8-2012

PROBING AND CONTROLLING FLUID RHEOLOGY AT MICROSCALE WITH MAGNETIC NANORODS

Alexander Tokarev
Clemson University, atokare@g.clemson.edu

PROBING AND CONTROLLING FLUID RHEOLOGY AT MICROSCALE WITH MAGNETIC NANORODS

A Thesis
Presented to
the Graduate School of
Clemson University

In Partial Fulfillment
of the Requirements for the Degree
Doctor of Philosophy
Materials Science and Engineering

---

by
Alexander Tokarev
August 2012

Accepted by:
Dr. Konstantin G. Kornev, Committee Chair
Dr. John Ballato
Dr. Igor Luzinov
Dr. Michael S. Ellison

ABSTRACT

This Dissertation is focused on the development of new methods for characterization and control of fluid rheology using magnetic nanorods. This Dissertation consists of five chapters. In the first chapter, we review current microrheologial methods and develop a Magnetic Rotational Spectroscopy (MRS) model describing nanorod response to a rotating magnetic field. Using numerical modeling, we analyze the effects of materials parameters of nanorods and fluids on the MRS characteristic features. The model is designed for a specific experimental protocol. We introduce and examine physical parameters which can be measured experimentally. The model allows identification of MRS features enabling the calculation of fluid viscosity. The MRS of Non-Newtonian fluids with exponentially increasing viscosity is discussed for the first time.

In the second chapter, we review the techniques for magnetic nanorods synthesis. We describe a setup and experimental protocol to synthesize nickel nanorods with the desired geometrical properties, in particular, with the controlled length to diameter ratio. We review magnetic systems used for manipulation of magnetic nanoparticles. A multifunctional magnetic rotator is introduced and described in detail in this chapter. We believe that this multifunctional magnetic system will be useful not only for micro and nanorheological studies, but will find much broader applications requiring remotely controlled manipulation of micro and nanoobjects.

In the third chapter, we describe the MRS experiments and use the model developed in the first chapter for characterization of magnetic properties of synthesized nickel nanorods. The same setup is used to measure viscosity of microdroplets. We show that the diffraction pattern from the suspension of nickel nanorods aligned in a magnetic field can be rotated by a spinning magnetic field. This effect opens up an opportunity for the MRS using much smaller nanorods. Another practical application of the controlled diffraction patterns is discussed: the use of this pattern in medical optofluidic devices producing stationary illuminating spots, for example, in endoscopes.

In the fourth chapter, we report on a new MRS method which can be used for *the in-situ* (or *in-vivo*) rheological measurements of fluids and polymer systems when the fluid viscosity increases exponentially with time. We use this method to measure the exponential change of the viscosity of HEMA (2-hydroxyethyl-methacrylate) undergoing photopolymerization. Remarkably, an exponential increase of viscosity can be traced beyond the point when the polymer system undergoes transition to a gel and the gel domains start to appear. We expect that this method will open up new horizons in the quantitative rheological analysis of fluids inside living cells, microorganisms, and aerosol droplets with thickeners.

In the fifth chapter, we describe a physical principle of self-assembly of magnetic nanorods into droplets of different sizes. These droplets can be formed on demand using magneto-static interactions between magnetic nanorods and a magnetic field gradient. We theoretically and experimentally confirmed that the cluster of nanorods

at the top of the droplet is acting as a cone-shape solid body deforming the top part of the droplet when moving towards the magnet. The developed model allows one to selectively concentrate a finite amount of magnetic nanorods at the free surface and print multiple microdroplets on demand.

ACKNOWLEDGEMENTS

Though this dissertation is a result of my work, I could never have performed all this work with such depth and detail without help, support, guidance and efforts of many wonderful people. First, I would like to express my deepest gratitude to my advisor, Dr. Konstantin G. Kornev, for his excellent guidance, caring, patience, and creating an inspiring atmosphere for conducting my research. He encouraged me to grow as a scientist and become an independent thinker.

I am sincerely grateful to my committee members: Dr. Igor Luzinov, Dr. Michael S. Ellison and Dr. John Ballato for their insightful comments and time.

The collaboration with Argonne National Lab was really fruitful. In particular I would like to thank Dr. Wah Keat Lee and Alex Deriy for their help with X-Ray imaging experiments. Also, I would like to thank Alexey Aprelev from Drexel University for his help with the design of magnetic rotator.

I would also like to thank Drs. Kornev's and Luzinov's group members, in particular, Serhiy Malynych, Maryana Kovalchuk, Taras Andrukh, Daria Monaenkova, Eugen Tatartschuk, Binyamin Rubin, Michael Seeber, Ruslan Burtovy, Bogdan Zdyrko, Chen-Chih Tsai, Fehime Vatansever, Yu Gu, Mahmut Kesimci, Marius Chyasnavichyus, and James Giammarco for their help and support at various stages of my research. I am very thankful to Kimberly Ivey, David White, Robbie Nicholson, Kathy Bolton and all other staff of MS&E department for their continuous support.

Special thanks to my close friends Maryana, Mike, Taras, Yury and Christy, who made this whole journey towards my doctorate and life at Clemson memorable.

My very special thanks to the one person whom I owe everything I am today, my mother, Elena Tokareva. Her unwavering faith and confidence in my abilities and in me is what has shaped me to be the person I am today. I would also like to thank my sister Anna Tokareva, her husband David and my stepdad Richard Steving. They were always supporting and encouraging me with their best wishes.

DEDICATION

I wish to dedicate this dissertation to my mother and my family.

LIST OF PUBLICATIONS

1) **Magnetic rotational spectroscopy with nanorods to probe time-dependent rheology of microdroplets.** *A. Tokarev*, I. Luzinov, J.R.Owens, K. G. Kornev, Langmuir, 2012, DOI: 10.1021/la3019474.

2) **Field-directed self-assembly with locking nanoparticles.** M. Motornov, S. Malynych, *A. Tokarev*, K. Kornev, I. Luzinov, S. Minko *at el*., Nanoletters, 2012, DOI: 10.1021/nl301780x.

3) **Multifunctional magnetic rotator for micro and nanorheological studies.** *A. Tokarev*, A. Aprelev, M. Zakharov, G. Korneva, Y. Gogotsi, K. G. Kornev, Review of Scientific Instruments, 2012, DOI: 10.1063/1.4729795.

4) **Butterfly proboscis: combining a drinking straw with a nanosponge facilitated diversification of feeding habits.** D. Monaenkova, M. S. Lehnert, T.Andrukh, C. E. Beard, B. Rubin, *A. Tokarev*, W. Lee, P. H. Adler, and K.G. Kornev, Journal of the Royal Society: Interface, 2012, 9(69), pp 720-726.

5) **Magnetic Nanorods for Optofluidic Applications**. *A. Tokarev*, B. Rubin, M. Bedford, K. G. Kornev, AIP Conference Proceedings, 2010, 1311, 204-209

6) **Magneto-Controlled Illumination with Opto-Fluidics**, S. Malynych, *A. Tokarev*, S. Hudson, G. Chumanov, J. Ballato and K. Kornev, Journal of Magnetism and Magnetic Materials, 2010, 322, 1894–1897

TABLE OF CONTENTS

Page

LIST OF FIGURES

Figure Page

Figure Page

Figure Page

Figure Page

LIST OF TABLES

1 MAGNETIC ROTATIONAL SPECTROSCOPY WITH NANORODS TO PROBE RHEOLOGY OF FLUIDS AT MICROSCALE

1.1 Literature review on magnetic nanorods in microrheological applications

Many polymers and biofluids rapidly react on the environmental conditions by changing their rheological properties[1]. Rheology of polymer solutions/gels (e.g. hazardous fluids containing thickeners) and biofluids depends on the concentration, level of cross-linking, oxygen content, temperature, pH, and many other environmental parameters. In biofluids such as cellular, mucosal and tissue fluids, the fluid viscosity changes over time making it challenging to quantify and analyze these changes. Drastic thickening of fluids in a short time interval often results in far-reaching consequences, for example, sickle cell disease results in the increase of the cytosolic viscosity inside the red blood cells [2, 3], polymerization of fibrinogen leads to fibrin clot formation and wound healing [4-6], etc. In polymer/biomedical engineering, fast polymerization processes are frequently used in different applications, for example, by HEMA (2-hydroxyethyl-methacrylate) photopolymerization, one can make contact disposable lenses [7-10]. Alginate and other polysaccharides, gelling in fractions of a second, are used for manufacturing fibers and films [11].These broad applications and abundance of rapidly gelling systems call for the methods of their analyses and characterization. The physics of

nucleation and the associated rheological fingerprints of the gelation process are hidden at the nanoscale and almost indistinguishable at the microscale.

A number of the microrheological methods were recently developed to study the rheology of fluids at microscale level [12-14]. These methods are summarized in Ref. [15]. Typically, a probe in a form of a solid particle is used and one measures its response to the thermal fluctuations (passive microrheology [14]) or to the external field, for example, magnetic field (active microrheology [13]). Active microrheology was used to study the rheological properties of different fluids [16-18]. Magnetic rotational spectroscopy (MRS) is a part of active microrheology where magnetic nanorods with unique rotational features deserve special attention [19-25]. First synthesis of rod-shaped magnetic nanoparticles was reported by Possin in 1970 [26]. While the interactions and applications of spherical particles were studied by many groups, the rod-like nanoparticles drew research interest only in recent years [21, 27-46]. Magnetic nanorods have several advantages over traditional spherical nanoparticles. High magnetization of magnetic nanorods allows one to control the nanorod orientation using moderate magnetic field. Additionally, nanorod solidity provides an easy way to manipulate the nanorod as a whole unit while chains formed by spherical particles are not stable in moving and rotating magnetic fields [47]. Properties of the template synthesized nanorods can be varied by changing the composition of the layers along its length during the electrochemical deposition of different metals into the pore of a template [48-56]. All these opportunities look attractive for applying nanorods in a lab-on-a-chip sensor, in particular, for rheological analysis of fluids given in a small amount. Ref. [30] reports that the

nickel nanorods do now show short term toxicity (<100 h) when embedded inside the living cells which makes them ideal candidates for *in vivo* microrheological measurements inside the living cells.

In the last decade, most attention has been paid to the development of MRS for simple Newtonian fluids. The available rheological techniques fall short to provide a viable information about the *in vivo* physico-chemical reactions and gelation mechanisms in the real time[1] especially when the amount of liquids is limited to microdroplets[3, 57] .

In this Chapter, we describe a theoretical model which can be used to study rheological properties of both Newtonian and non-Newtonian fluids at microscale level. This chapter is organized as follows. We first introduce analytical and numerical models describing the nanorod rotation in liquids with constant viscosity. We describe an experimental protocol which can be coupled with our theoretical model and used for the microrheological measurements. We then use these models to theoretically predict the behavior of magnetic nanorods in rotating magnetic fields of different frequencies in liquids with different viscosities in the range of $0<\eta<10000$ mPs*s. Moreover, we study the effects of materials parameters such as magnetic and shape factors of nanorods. Then we modify our numerical model to predict the nanorod behavior in non-Newtonians fluid with exponentially increasing viscosity. We present a full numerical analysis and summarize the results in a form of a phase portrait which can be used to study the system behavior at different conditions depending on the initial angle between the nanorod and the magnetic field, initial

viscosity of the liquid, aspect ratio and diameter of the nanorod, its magnetic properties, frequency and magnitude of magnetic field. We conclude with a summary of our findings.

1.2 Analytical and numerical analysis of nanorod rotation in liquids with constant viscosity

1.2.1 Derivation of the basic equation [58], [59]

Consider a magnetic nanorod suspended in a liquid. A rotating magnetic field is applied to this system. Rotation of a magnetic nanorod is shown in Figure 1.1 where we introduced different angles specifying the nanorod rotation.

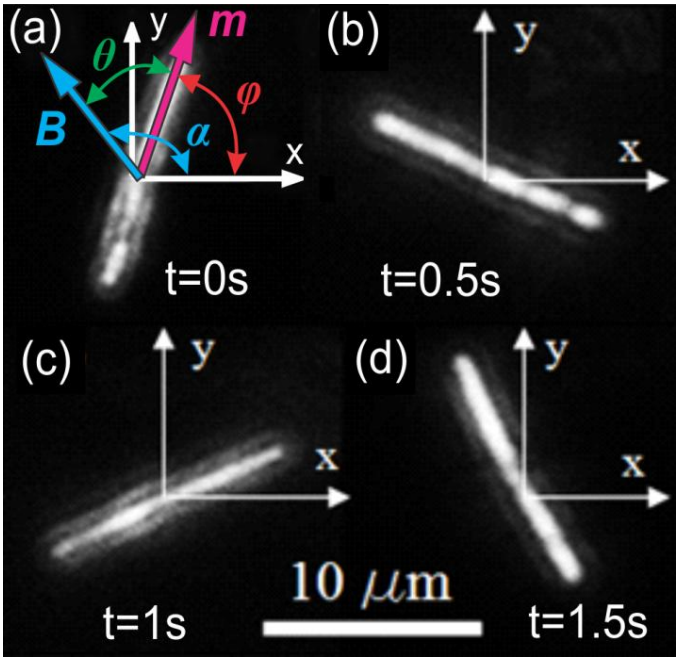

Figure 1.1 Counter 2D clockwise rotation of the nickel nanorod (d=200nm in diameter). Uniform magnetic field rotates with constant frequency f=0.5Hz forcing the nanorod to follow it.

The angle α specifies the direction of applied magnetic field **B** with respect to the reference axis X. Since the applied field rotates at the constant rate, this angle depends linearly on time, $\alpha = 2\pi ft$, where *f* is the frequency of the rotating magnetic field. We assume that the magnetization vector **M** is directed parallel to the nanorod axis. The drag force resists the nanorod rotation causing the nanorod to lag behind the field, making angle θ with vector **B** (Figure 1.1). In order to derive an equation governing the nanorod rotation, it is convenient to count its revolutions with respect to the fixed system of coordinates, i.e. with respect to the X-axis. Therefore, if the nanorod axis makes angle $\varphi(t)$ with the X-axis, this angle can be connected with $\alpha(t)$ and $\theta(t)$ as $\varphi(t) = 2\pi ft - \theta(t)$.

The torque balance equation reads $\left(\gamma d\varphi / dt\right)\mathbf{e} = \mathbf{M} \times \mathbf{B}$, where γ is the drag coefficient, and **e** is the unit vector directed perpendicularly to the plane of the nanorod rotation [60, 61]. Substituting the definition of angle $\varphi(t)$ through the angles $\alpha(t)$, and $\theta(t)$ the governing equation takes on the following form [21]:

$$\gamma\left(2\pi f - \frac{d\theta}{dt}\right) = mB\sin\theta, \tag{1.1}$$

where m is the magnetic moment of the nanorod. The drag coefficient γ depends on the nanorod length *l*, its diameter *d* and liquid viscosity η

$$\gamma = \frac{\eta l^3 \pi}{3\ln\left(l/d\right) - A}, \tag{1.2}$$

where $A \approx 2.4$ is a constant calculated in Ref. [62].

1.2.2 Analytical solution of the basic equation. Comparison with a numerical example

Integrating Eq. (1.1) , we find an implicit $\theta(t)$ dependence as

$$t = \frac{1}{C_2} \cdot \frac{2\arctan(k/\sqrt{1-k^2})}{(\sqrt{1-k^2})} - 2\arctan((k - \tan(\frac{\theta}{2})) \tag{1.3}$$

where $k = C_1 / C_2$, $C_2 = 2\pi f$, $C_1 = mB(3\ln\left(l/d\right) - A) / \eta l^3 \pi$

Equation (1.1) was also solved numerically by variable order method using MatLAB function ODE15i. Nanorod with length l=6.6 μm and diameter d=0.2 μm in ethylene glycol with viscosity η = 16·10^{-3}Pa·s was used as an example. The magnetization was set as m=2.25*10^{-14} A*m^2 and magnetic field was set as B=0.0015 T. The results of the analytical and numerical solutions $\theta(t)$ at the frequency of driving field f=1Hz are presented in the next figure:

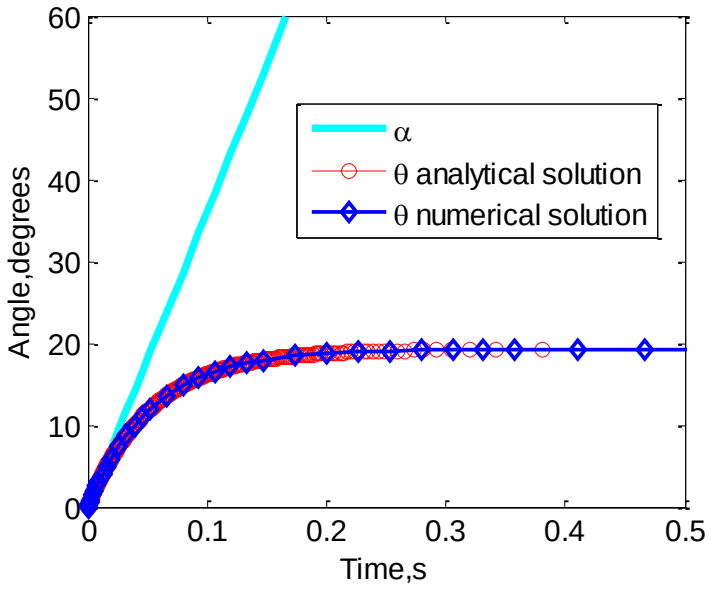

Figure 1.2 Numerical and analytical solutions of the Eq. (1.1) for the angle θ at frequency of driving field f=1Hz.

The magnetic field is rotating with the 1 Hz frequency and its rotation is shown as a solid line in Figure 1.2. The analytical solution of Eq. (1.1) is shown as a solid line with the circular markers and the numerical solution is shown as a solid line with the diamond markers. As seen from Figure 1.2 , both numerical and analytical solutions are in an excellent agreement. After about 0.2 seconds from the beginning of the rotation process, the angle θ stops changing, implying that the nanorod picks up the driving frequency of the magnetic field and keeps rotating synchronously with the field making angle $\theta_{steady} = 19^0$ with it.

When the frequency of driving field increases up to f=4Hz, the nanorod behavior changes drastically, Figure 1.3 (a): one observes a periodic solution.

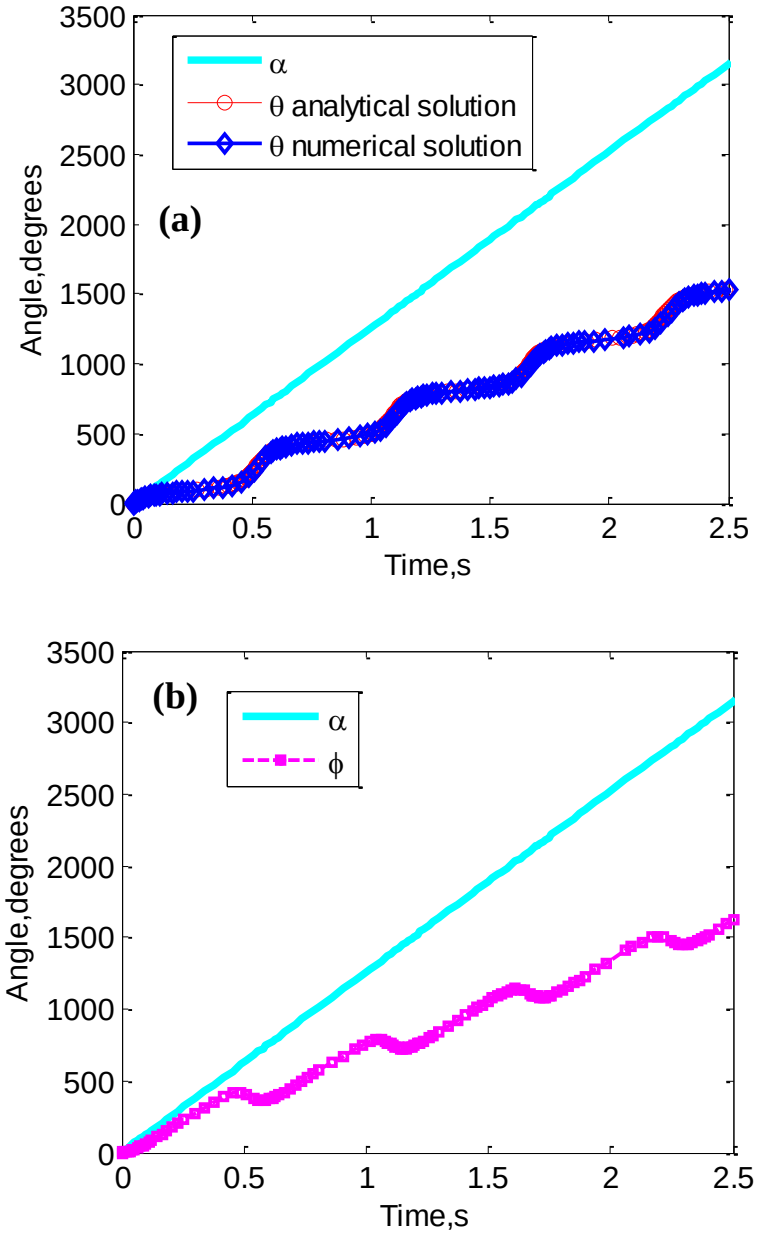

Figure 1.3 (a) Numerical and analytical θ-solutions of Eq. (1.1) when the frequency of the driving field increases to f=4Hz, (b) φ-solution, $\varphi(t) = 2\pi ft - \theta(t)$.

This periodic solution has an interesting consequence: the φ - solution show in Figure 1.3 (b) that corresponds to the behavior of angle φ that the nanorod makes with the X-axis, (Figure 1.1), acquires a periodic component as well. The φ - angle is still increasing with time, i.e. the nanorod keeps revolving about its center, but on the

background of continuous revolution, the nanorod starts to oscillate. The derivative $d\varphi / dt$ periodically changes the sign. The period of each nanorod revolution is different from the revolution time of the magnetic field. Thus, one can say that the nanorod rotates asynchronously with the field. This critical driving frequency f_{cr} specifying the frequency at which the nanorod cannot be picked up by the field anymore, is a very important parameter depending on the fluid viscosity, nanorod characteristics and the magnitude of the applied magnetic field.

1.2.3 Full analysis of the basic equation. Phase portrait.

It is convenient to introduce the dimensionless parameters by rewriting Eq. (1.1) as:

$$\frac{2\pi f\gamma}{mB}\left(1-\frac{d\theta}{2\pi fdt}\right)=\sin\theta, \tag{1.4}$$

A new dimensionless parameter V characterizes the strength of the drag torque with respect to the magnetic torque:

$$V=\frac{2\pi\gamma f}{mB} \tag{1.5}$$

The denominator of Eq. (1.5) provides an upper estimate of the magnetic torque. The numerator provides an upper estimate of the drag torque assuming that the nanorod revolves with the frequency of applied field.

$$V\left(1-\frac{d\theta}{2\pi fdt}\right)=\sin\theta, \tag{1.6}$$

Introducing dimensionless time $T=2\pi ft$, we obtain

$$\frac{d\theta}{dT} = \frac{1}{V}(V - \sin\theta), \tag{1.7}$$

Thus, only a single V-parameter carries all information about the materials properties of the nanorod and the fluid. Changing the V-parameter, we can plot a set of trajectories of Eq. (1.7).

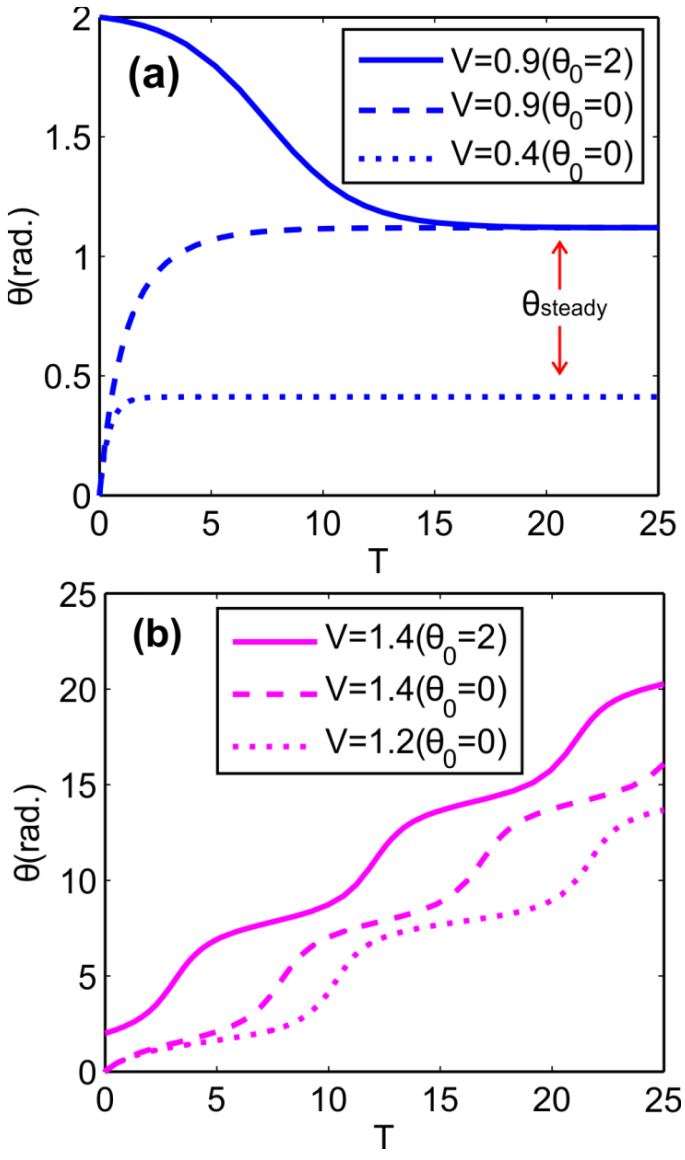

Figure 1.4 Integral curves of Eq. (1.7) showing the solution behavior for different parameters $V(l,d,\eta,B,m,f)$ at different initial conditions θ_0. (a) V<1. (b) V>1.

Effect of V – parameter. V<1. The dashed and dotted lines in Figure 1.4 (a) show the behavior of angle θ with time when the V-parameter is less than one, V =0.9, V=0.4 < 1, and the magnetic torque is stronger than the viscous drag. Initially, the nanorod and magnetic field are co-aligned, $\theta_0 = 0$. It can be seen that the angle θ increases and then stops changing. From this moment on, the nanorod starts rotating synchronously with the field making constant angle θ_{steady} with it. The greater the parameter V, the greater the constant θ_{steady}. According to Eq. (1.5), the V – parameter can be increased by increasing the fluid viscosity or decreasing the field strength. Therefore, the changes of viscosity or magnetic field can be traced through the change of θ_{steady} .

Effect of initial nanorod orientation. V<1. The solid line in Figure 1.4 (a) corresponds to initial condition $\theta_0 = 2$. In this case, the magnetic force is stronger than the viscous drag, but the initial angle between the nanorod and the field is greater than $\pi/2$. According to Eq. (1.7), this initial condition makes the right hand side negative, i.e. the angle θ decreases in first moments of time. Magnetic field moves in positive direction, i.e. in the counter clockwise direction toward the direction where the initial magnetic moment is pointing to. On the other hand, the magnetic torque always turns the nanorod toward the field direction. These two simultaneous movements result in a decrease of angle θ. When angle θ reaches the value V = sin θ, the derivative in Eq. (1.7) goes to zero and the angle reaches its steady state value θ_{steady}. Thus, for V<1, the initial orientation of the nanorods has no influence on the steady state angle θ_{steady}

.

An interpretation of the theta-solutions becomes easier when we look at angle φ that the nanorod makes with the X-axis, $\varphi(t) = 2\pi ft - \theta(t)$ (Figure 1.1). This angle can be measured experimentally by directly following the nanorod rotation with a camera and a microscope.

Figure 1.5 shows the behavior of φ-solutions corresponding to the nanorod trajectory. Ethylene glycol is used as a carrying fluid. The angle φ was calculated as $\varphi(t) = \alpha(t) - \theta(t)$:

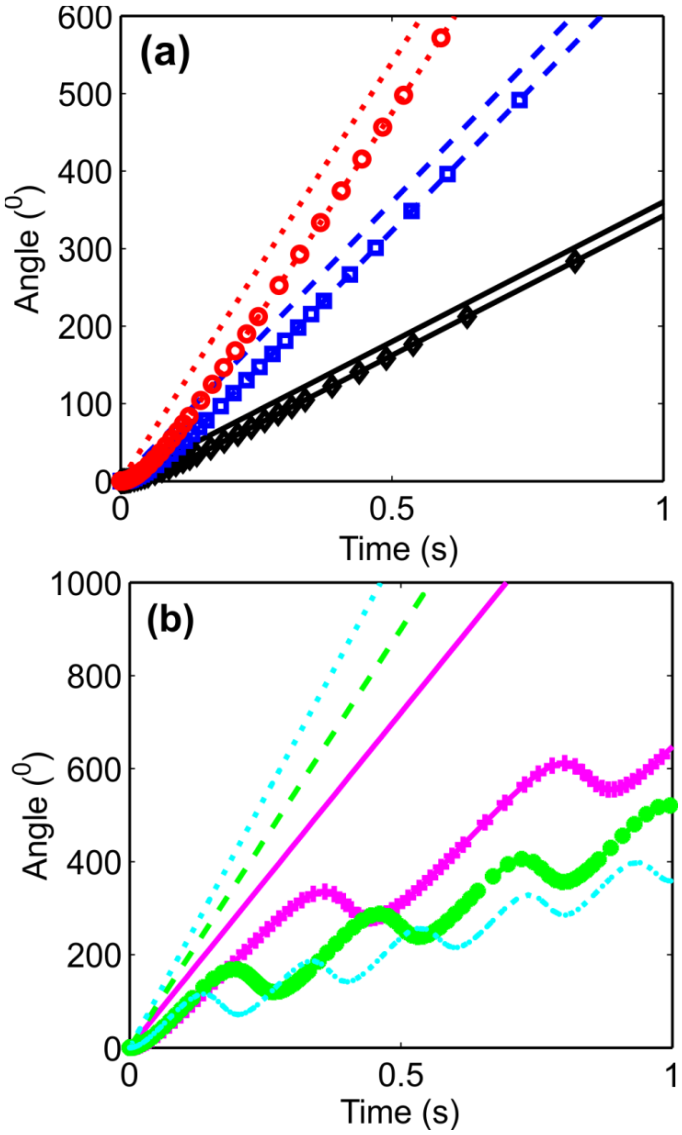

Figure 1.5 (a) The φ-solutions of Eq. (1.7) for different driving frequencies of magnetic field. The upper straight lines correspond to the change of α-angles with frequencies f = 1Hz (straight solid line), f = 2Hz (straight dashed line) and f = 3Hz (straight dotted line). The corresponding φ-solutions are marked with different symbols. The nanorod rotates synchronously with magnetic field at these frequencies, (b) the φ-solutions of Eq. (1.7) for different driving frequenciencies of magnetic field. The upper straight lines correspond to the change of alpha-angles with frequencies f=4Hz (straight solid line), f=5Hz (straight dashed line) and f=6Hz (straight dotted line). The corresponding φ-solutions are marked with different symbols.

Figure 1.5 (a) shows a series of numerical solutions of Eq. (1.7). These φ - solutions are asymptotically linear functions of time: the slopes of solid lines and the

corresponding lines with markers are the same and are equal to the frequency of the driving field and the frequency of rotating nanorod, respectively. These solutions describe a synchronous rotation of the nanorod with magnetic field when the nanorod makes a constant angle with the field direction during this rotation.

This numeric analysis suggests that when parameter V is smaller than one and magnetic torque dominates the drag torque, one can have a time independent solution of Eq. (1.7). The trajectories in Figure 1.5 (a) have constant asymptotes describing this type of solutions when the nanorod is picked up by magnetic field and rotates synchronously with the field. The phase lag between the field and nanorod becomes constant when derivative $d\theta / dT$ becomes zero. In this case, Eq. (1.7) is simplified to

$$\gamma 2\pi f = mB\sin\theta_{steady}. \tag{1.8}$$

Solving this equation for θ_{steady}, we notice that the solution exists if and only if the rotation frequency *f* is below the critical frequency [21, 61] :

$$f_c = \frac{1}{2\pi}\frac{mB}{\gamma}. \tag{1.9}$$

Expressing the magnetic moment through the material magnetization *M*, $m = Mv$, where

$$v = \frac{\pi d^2 l}{4} \tag{1.10}$$

is the nanorod volume, and combining equations (1.2) and (1.9), we notice that the dimensionless critical frequency f_d does not depend on the particular size of the nanorod, but only on the nanorod aspect ratio:

$$f_d = \frac{8\pi\eta f_c}{MB} = \frac{3\ln\left(\frac{l}{d}\right) - 2.4}{\left(\frac{l}{d}\right)^2} \tag{1.11}$$

Indeed, the viscous torque in Eq. (1.1) is proportional to l^3, while the magnetic torque is proportional to d^2l. Thus, these two torques compensate each other and the length scale is cancelled leading to a universal dependence(1.11). Figure 1.6 illustrates the dependence of dimensionless critical frequency f_d on the nanorod aspect ratio. Understanding this universal behavior of nanorods is important for practical applications: the rheological properties of very small droplets can be studied at a fixed frequency by adjusting the aspect ratio of the nanorods.

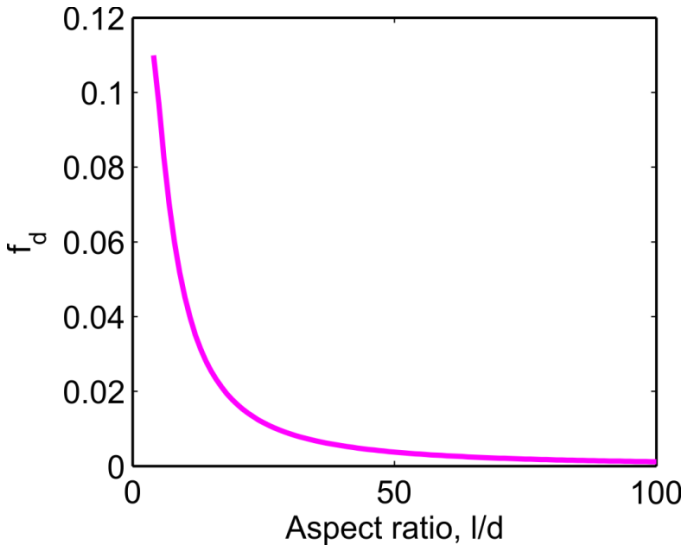

Figure 1.6 Dependence of dimensionless critical frequency f_d on nanorod aspect ratio. V > 1.

Three lines in Figure 1.4 (b) show the behavior of angle θ with time when the viscous drag is greater than the magnetic force and the nanorod cannot follow the applied magnetic field. When the V-parameter is greater than one, the solutions do not have any linear asymptote as time goes to infinity. All solutions change periodically: the right hand side of Eq. (1.7) is a periodic function of θ, hence the time derivative on the left hand side is also a periodic function. This behavior is illustrated by our numeric example when we increase the frequency up to f=4Hz. The linear solutions are turned into the oscillating solutions in Figure 1.5 (b).

This theoretical analysis suggests that the nanorod behavior in a rotating magnetic field significantly depends on the revolution rate of magnetic field. One can distinguish synchronous rotation from asynchronous one by changing the rotation rate of the magnetic field. The critical frequency is an important parameter which is easy to measure experimentally by detecting a moment when the nanorod starts oscillating

and slows down its rotation while the operator increases the frequency of the driving field. Obtaining this parameter from experiments, one can infer the viscosity of the surrounding fluid by solving Eq. (1.1) numerically or analytically and therefore, knowing the critical frequency and geometrical parameters of the nanorod, one can measure either fluid viscosity (provided that the magnetic moment *m* is known) or the nanorod magnetic moment (provided that the fluid viscosity is known) [21, 22]. This method was used to calculate magnetic properties of nanorods and to measure viscosity of liquids in microdroplets [22]. Experimental protocols and calculations are described in Chapters 3 and 4.

1.2.4 Effect of materials parameters

In order to use the magnetic rotational spectroscopy method for the rheological analysis of fluids at the microscale level, a dependence of V-parameter on materials properties should be analyzed. Estimating the volume covered by a 5 μm long and 0.2 μm thick nanorod as 1pL, one concludes that the MRS is able to evaluate the rheological properties of droplets as small as 1pL. Nanorods with the desired geometrical properties can be produced by template-assisted electrochemical deposition method [22, 63-65]. The nanorod synthesis is described in details in Chapter 2. Nanorods are formed in the pores of the template by electrodeposition of the metal from the counter electrode. Nickel, cobalt, iron and ferrite are the most used materials for nanorods synthesis [26, 39, 41, 66-75]. Typically, the nanorods are formed in membanes with 0.2, 0.4 or 1 μm pore diameters. The pore diameter defines the diameter of the nanorods. By varying the time of electrodeposition, it is possible to produce nanorods with aspect ratio l/d in the range of $4<l/d<200$.

First, we analyze a dependence of V-parameter on aspect ratio of magnetic nanorod in the range of $4<l/d<100$ because nanorods with aspect ratio greater than 100 are very brittle and can be broken in a rotating magnetic field. Nanorod was assumed to be a single-domain particle with a magnetic moment equal to $m = M_s v$, where M_s is the saturation magnetization of the material and v is the particle volume. Table 1.1 provides the values of saturation magnetization M_s for the most popular materials:

Table 1.1 Values of saturation magnetization Ms for the most popular magnetic materials used for nanorods synthesis.

Substance	Magnetization M_s ($*10^3$ A/m)
Fe(Iron)	1707
Cobalt(Co)	1400
Ni(Nickel)	485
Ferrite (Fe_3O_4)	480

By substituting Eqs. (1.2) and (1.10) in Eq. (1.5) we obtain the following equation showing the dependence of V-parameter on different parameters of the system:

$$V = \frac{2\pi\gamma f}{mB} = \frac{8\pi\eta f}{3MB(\ln(\frac{l}{d}) - A)}(\frac{l}{d})^2 \qquad (1.12)$$

Once again, the V-parameter appears independent on the nanorod size: only the nanorod aspect ratio affects its value. The V-parameter was calculated for nickel

nanorods with different aspect ratios ($4<l/d<100$) suspended in ethylene glycol (η=16.1 mPa*s) rotating in magnetic field B=0.0015. Such field can be generated by small, inexpensive, commercially available magnetic coils [12, 21, 24, 76-83]. The results for two frequencies of driving magnetic field (f=3,4) are presented in the next figure:

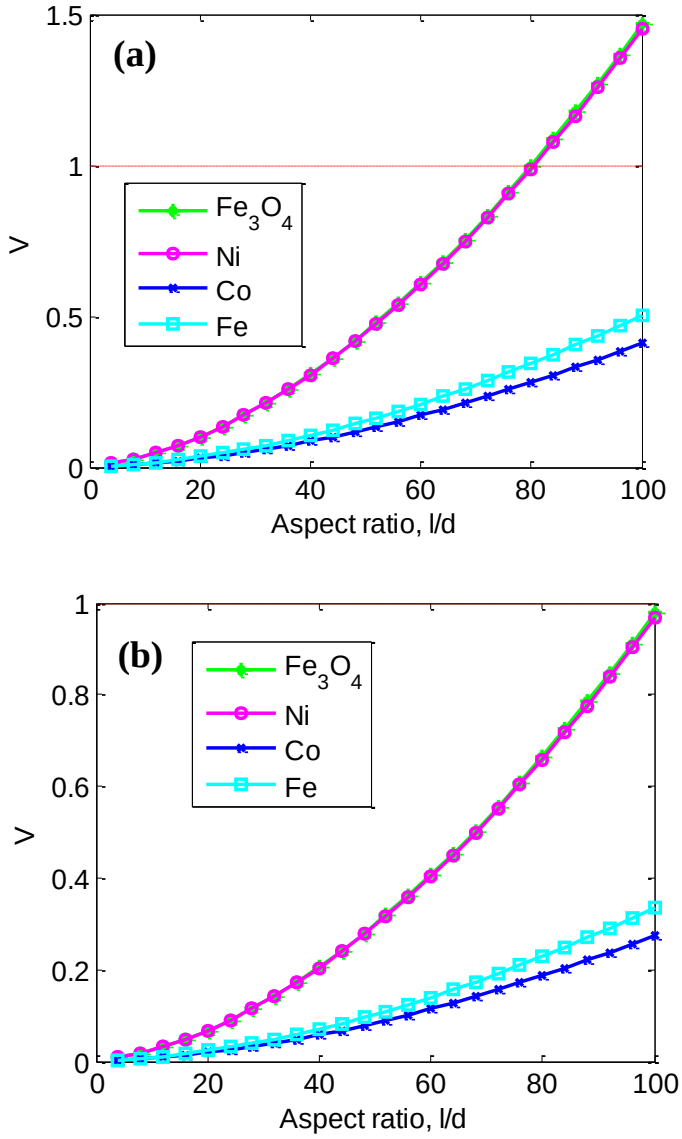

Figure 1.7 The dependence of V-parameter (Eq. (1.12)) on the nanorod aspect ratio. (a) Frequency of rotating magnetic field f=3, viscosity of the fluid η=16.1 mPa*s (ethylene glycol), magnetic field B=0.0015T, nanorod material – nickel, (b) frequency of rotating magnetic field f=2, all other parameters are the same.

The V-parameter increases with the aspect ratio because the numerator in Eq. (1.12) is getting larger as the drag torque increases, Figure 1.7 (a). The solid horizontal line in Figure 1.7 (a) defines two regions: the first one is where V<1 and the nanorod is rotating synchronously with magnetic field. This region can be used for viscosity measurements: applying the rotating magnetic field at f=3Hz and then increasing the frequency of the field up to f_{cr} one can measure the critical frequency.

The second region lies above the V=1 curve. In this region, the nanorod either rotates asynchronously with the field or does not revolve at all. In Figure 1.7 (a) the frequency is equal to f=3Hz and in Figure 1.7 (b) it is f = 2Hz. At the f=3Hz frequency of driving field there is a region for nickel and ferrite nanorods where they cannot be used for rheological measurements (Figure 1.7 (a), aspect ratio l/d>80, V>1). From this analysis we can conclude that the nanorods with low aspect ratios are better to use for rheological measurements in fluids with low viscosities.

In order to test the nanorods behavior at higher viscosities we took glycerol as an example of liquid with high viscosity (η=1200 mPa*s). The dependence of V-parameter on the aspect ratio of nanorods for glycerol is plotted in the next figure:

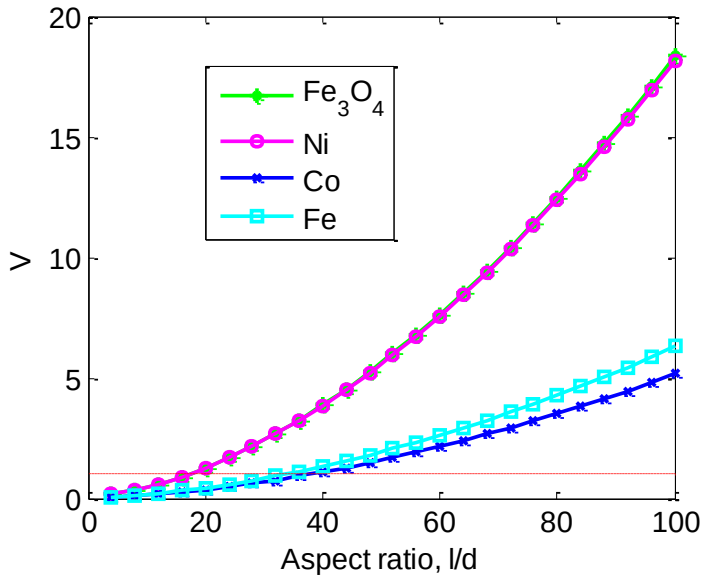

Figure 1.8 The dependence of V-parameter on the aspect ratio of nickel nanorod in glycerol (η=1200 mPa*s) in rotating magnetic field B=0.0015T.

The nickel and ferrite nanorods can be used for viscosity measurements only if the aspect ratio is lower than 16 corresponding to the region where V<1. Nanorods with aspect ratios up to 40 can be used if they are made from iron and cobalt.

In order to design a method for rheological measurements at the microscale we analyzed our model at different viscosities. Table 1.1 provides viscosities of some liquids of interest:

Table 1.2 Viscosities of some liquids of interest.

Liquid	Viscosity (cp=Mpa*s)
Ethanol	1.74
Corn syrup	1380
Glycerol	1200
Molten glass	>10000
Ethylene glycol	16
Castrol oil	1000

First, we analyzed the dependence of V-parameter on the viscosity of carrying fluid η. This parameter is linearly proportional to the viscosity and behavior of parameter V for nanorods rotating in fluids with $0<\eta<1500$ mPs*s is presented in Figure 1.9 (a):

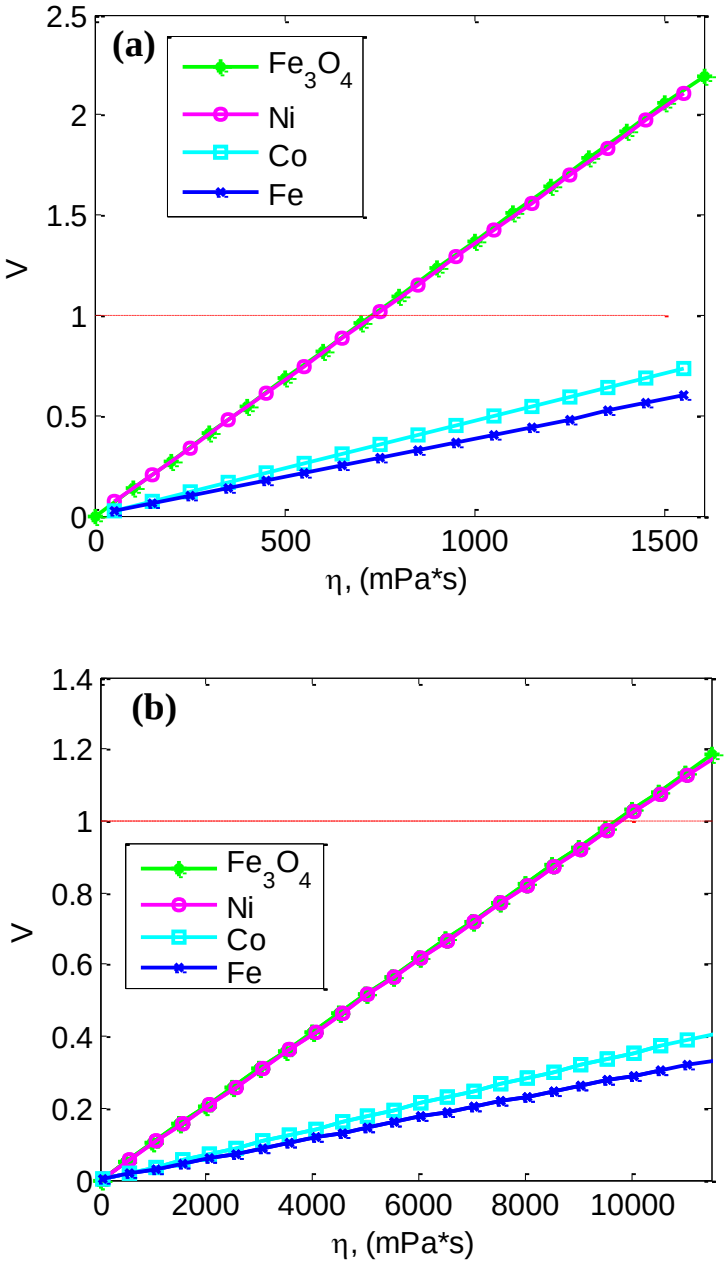

Figure 1.9 The dependence of V-parameter on the viscosity of carrying fluid for nanorods with aspect ratio *l/d*=15 (a) magnetic field B=0.0015T (b) magnetic field B=0.01T

The nickel and ferrite nanorods can be used to probe fluids with viscosities up to 600 mPa*s in the region where V<1; the iron and cobalt nanorods can be used to probe fluids with higher viscosities, up to 1500 mPs*s using the magnetic field B=0.0015T.

In order to probe fluids with viscosities up to 10000 mPa*s, the magnetic field should be increased thus decreasing the V-parameter, Eq. (1.12). When the magnetic field is raised up to 0.01T (Figure 1.9 (b)) it appears possible to probe fluids with viscosities up to a 10000 mPs*s with a nanorod made from any magnetic material from the Table 1.1 if it has the aspect ratio l/d=15

1.3 Numerical analysis of nanorod rotation in liquids with exponentially changing viscosity

When the liquid viscosity is not constant, we cannot use Eq. (1.1) anymore. In this case, the drag coefficient is changing in time because of the viscosity change. We used UV polymerization of HEMA as a system with a time dependent viscosity. The HEMA viscosity exponentially increases during free radical (three-dimensional UV) polymerization in the presence of the cross-linker DEGDMA (diethylene glycol dimethacylate) [7]. The gel point for the system can be reached in 60-200 seconds depending on the DEGDMA concentration [7]. The time dependent viscosity of many monomers undergoing polymerization is typically described by the following equation [7], [9]:

$$\eta(t) = \eta_0 e^{\frac{t}{\tau}} \tag{1.13}$$

where η_0 is the initial viscosity of monomer solution, t is the time and τ is the characteristic time of polymerization. This characteristic time is considered as a phenomenological parameter of the polymerization process [7], [9]. In Figure 1.10,

we plot relative viscosity $\eta(t)/\eta_0$ (bulk measurements from Ref. [7]) of HEMA undergoing photopolymerization for the different power of the UV irradiation**[7]**.

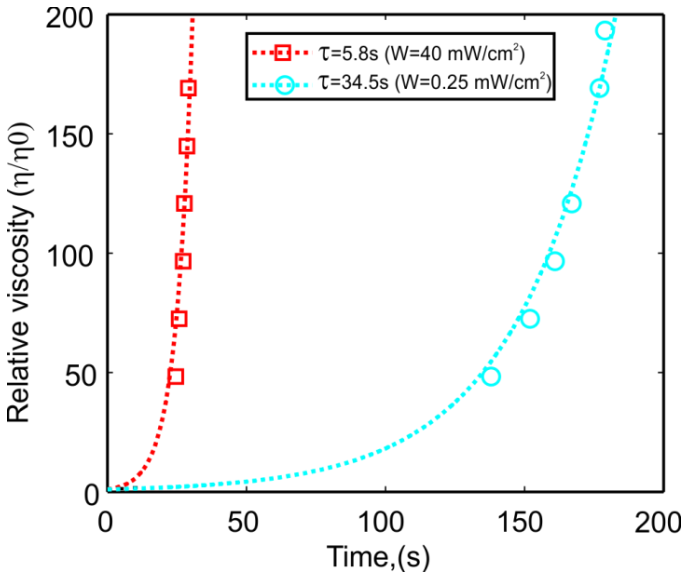

Figure 1.10 Viscosity change during UV photopolymerization of HEMA with 1.86wt% concentration of the crosslinker corresponding to $\tau = 5.8$ s and $\tau = 34.5$ s.

It can be seen that these measurements are well fitted by the exponential curves with different characteristic time τ (Eq. (1.13), $\tau = 5.8$s for the UV irradiation with W=40 mW/cm^2 power and $\tau = 34.5$s for the UV irradiation with W=0.025 mW/cm^2 power). The physics of exponential thickening of fluid via three-dimensional polymerization is not completely understood, yet some key mechanisms leading to this effect have been identified [10].

In order to assess the polymerization kinetics using rheological data, it is therefore imperative to correlate the kinetic parameters with the rheological parameters η_o and τ. The existing basic MRS model does not take into account the time dependence of

the fluid viscosity. When the viscosity of liquid is increasing exponentially in time drag coefficient changes as:

$$\gamma(t) = \frac{\eta_0 e^{\frac{t}{\tau}} l^3 \pi}{3\ln(l/d) - A}, \tag{1.14}$$

Hence the analysis of Eq. (1.1) deserves special care. We analyze this case by introducing the dimensionless times $T = 2\pi ft$ and $T_0 = 2\pi f\tau$. Then Eq. (1.1) can be rewritten as: $\beta e^{T/T_0}(1 - d\theta/dT) = \sin(\theta)$, where

$$\beta = \frac{\eta_0 l^3 2\pi f}{mB(3\ln(l/d) - A)}. \tag{1.15}$$

After making this nondimensionalization, all physical parameters of our problem collapse into two dimensionless complexes, β and T_0. The dimensionless parameter β describes all possible scenarios of the nanorod rotation: assume first that the drag force is much greater than the magnetic torque. This implies that the dimensionless parameter beta is much greater than one, $\beta >> 1$. Hence, as follows from the governing equation, $(1 - d\theta/dT) = (1/\beta)e^{-T/T_0}\sin(\theta) \approx 0$, or $\theta \approx T$, i.e one would not expect any rotation of the magnetic nanorod. In other limit, when the drag force is much smaller than the magnetic torque, the beta-parameter is much smaller than one, $\beta << 1$. As follows from the governing equation, $\beta e^{T/T_0}(1 - d\theta/dT) = \sin(\theta)$, one would expect to observe the nanorod rotation until the left hand side is smaller than one.

For complete analysis of the nanorod rotation, it is convenient to introduce new auxiliary function $U = \beta e^{T/T_0}$. Then Eq. (1.1) is rewritten as a system of two first order differential equations,

$$\begin{aligned} d\theta / dT &= 1 - \sin\theta / U, \\ dU / dT &= U / T_0. \end{aligned} \tag{1.16}$$

Dividing the first equation onto the second, we obtain,

$$\frac{d\theta}{dU} = \frac{T_0}{U^2}(U - \sin\theta). \tag{1.17}$$

Equation (1.17) allows one to perform a complete analysis of the nanorod dynamics depending on the viscosity, nanorod magnetization, magnetic field, and initial conditions. According to the definition of function *U*, the initial condition for this function reads $U(0) = \beta$. Therefore, in the plane (U, θ), each vertical line $U(0) = \beta$ corresponds to a continuous set of initial angles $\theta(0) = \theta_0$. Equation (1.17) has many solutions, but the nanorod dynamics is described by a single solution corresponding to a finite interval.

1.3.1 Dynamics of nanorods starting rotation at φ(0)=0.

For an interpretation of the images of rotating nanorods, we need to follow the $\varphi(t)$-dependence. Therefore, we rewrite the torque balance equation in the following form $\gamma(t) d\varphi / dt = mB\sin(2\pi ft - \varphi)$. As an initial condition, we can always choose

$\varphi(0)=0$ implying that the nanorod is initially aligned with the field. The right hand side of this equation is positive within the time interval $t<t_c$, where t_c is the first root of the equation $2\pi ft_c-\varphi(t_c)=0$. This root is well defined for each τ: it corresponds to the first maximum of function $\varphi(t)$. In Figure 1.11 (a) we show the behavior of the nanorod with length *l*=5 μm, diameter *d*=0.2 μm, initial viscosity of the HEMA solution η_0= 2.7 mPa·s, magnetic field B= 0.0015 T, and frequency of the rotating field *f*=0.5Hz.

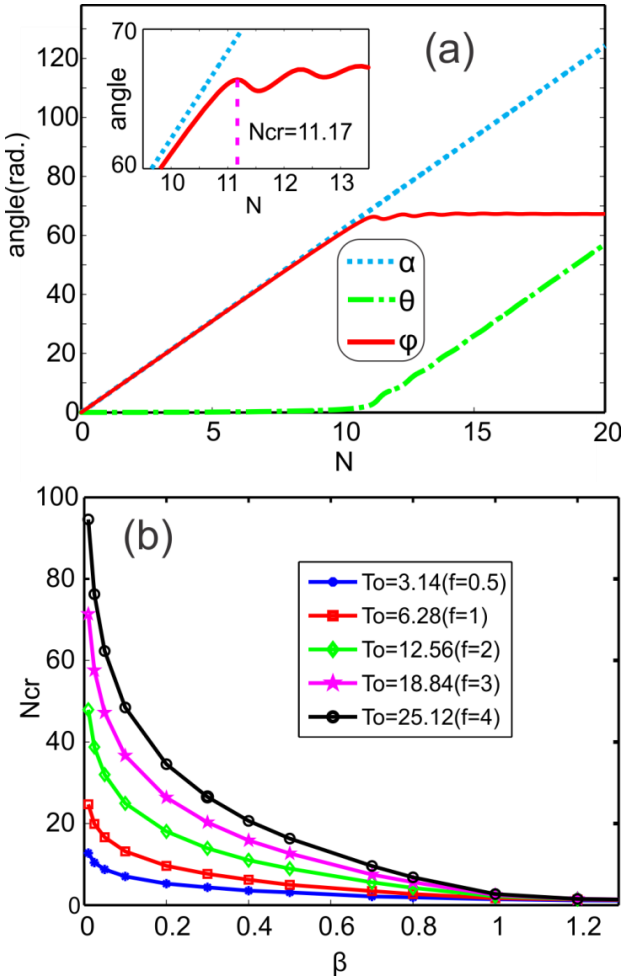

Figure 1.11 (a) Numerical solutions for φ, α and θ as functions of the number of turns, *N=t·f* , of a nanorod. The inset shows oscillating behavior of a nanorod which is about to stop its rotation after N_{cr} ~ 11 revolutions, (b) the dependence of the critical number of turns of a nanorod on parameter *β*

In Figure 1.11 (a), the nanorod revolves seven times at the frequency of rotating field and the dashed and solid lines corresponding to the field and nanorod rotation angles, respectively, coincide. On the other hand, the dash-dot line corresponding to the θ-angle stays zero. Thus, during this rotation period the field and magnetization are oriented parallel to each other. After seven turns, the slope of the solid line changes implying a gradual decrease of the rotation rate from 0.5 Hz to 0.45 Hz. It can be seen from the graphs that the nanorod (φ) follows the rotation of the field (α) for about N_{cr}=11.17~11 revolutions. After N_{cr} turns, the derivative of $\varphi(N)$ changes the sign from positive to negative and the nanorod sways back about 45°. After that, the nanorod rotates back and forth with decreasing amplitude and then completely stops at N~15. In experiments, $N_{cr.}$ can be found by measuring the time (or number of turns) that the nanorod takes on before it sways back for the first time. In Figure 1.11 (b), we plot the dependence of this critical parameter N_{cr} as a function of T_0 and β.

One can infer from these dependencies that the number of turns significantly decreases as the initial viscosity increases and as the external field increases. This analysis suggests an experimental strategy for the investigation of rheological properties of polymeric fluids during polymerization. That is, one needs to measure N_{cr} and use τ as an adjustable parameter to fit the experimental N_{cr} with the theoretical one.

1.3.2 Dynamics of nanorods starting rotation at arbitrary angle θ_0.

There are three possible scenarios of nanorod rotation starting at an arbitrary angle θ_0. The results of numerical analysis of Eq. (1.17) are summarized in a form of the phase

diagram shown in Figure 1.12. The initial conditions satisfying the inequality $U_0 = \beta < 1$ correspond to the case when the magnetic torque is stronger than that caused by the viscous drag. The shaded region under the curve $U = \sin\theta$ corresponds to the conditions that cause the rod to sway toward the field direction at the initial instants of time. When the viscous drag takes over, the rod slows down its rotation and eventually stops. Since magnetic field keeps revolving, the angle $\theta(U)$ increases with each revolution even if the nanorod is not moving. Therefore, the integral curves coming out from the shaded region first decrease, form minimums at curve $U = \sin\theta$, and then turn up to increase.

This behavior can be easily observed experimentally by first aligning the nanorods with a bias field and then applying the rotating field which is directed perpendicularly to the nanorods at *t*=0. Therefore, the initial condition for this experiment is stated as $\theta_0 = \pi/2$. The time when the nanorods form the minimum angle $\theta_{\min}$ with the rotating field can be thus obtained as $\beta e^{T_{\min}/T_0} = \sin\theta_{\min}$ or $T_{\min} = 2\pi f \tau \ln(\sin\theta_{\min}/\beta)$. Since $\theta_{\min}$ and $T_{\min}$ are well defined experimentally, one can infer the τ parameter from this relation.

Numerical analysis shows that all curves coming out of the shaded region, first pass a minimum, then find their way to move at a close proximity of curve (A). When *U* is large, $U >> 1$, Eq. (1.17) can be integrated to give $\theta = T_0 \ln U$, which means that angle θ increases linearly with time. These asymptotics explains why all integral curves run parallel to each other as *U* increases.

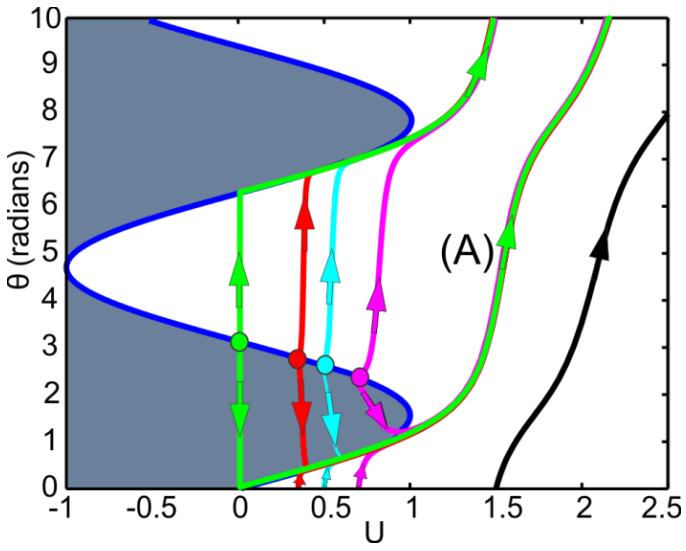

Figure 1.12 Phase portrait for Eqs (1.16) showing the solution behavior for different initial conditions U_0, θ_0 at fixed dimensionless $T_0 = \pi$. Only $U > 0$ is of practical interest hence the integral curves for $U < 0$ are not shown.

The integral curves coming out from the regions outside the shaded area in Figure 1.12, always increase as U increases. Therefore, as follows from the definition of angle θ, we have the following inequality $d\theta/dt = 2\pi f - d\varphi/dt > 0$, or, rewriting it for the observable angle, we obtain $2\pi f > d\varphi/dt$. This behavior suggests that the external field rotates faster than the rod for these initial conditions. The phase portrait sketched in Figure 1.12 is applicable for all T_0, yet the slopes of the integral curves are influenced by this parameter T_0.

The characteristic features of the nanorod behavior can be further elucidated by following the trajectories belonging to different regions on the phase portrait. For example, the initial conditions θ_0 = 0, 2, and 2.9 correspond to three different types of the nanorod trajectories. From equation $\varphi(t) = \alpha(t) - \theta(t)$ one can infer the following

initial condition for φ-solutions: $\varphi(0) = -\theta(0)$. The results of these calculations are presented in Figure 1.13 for the physical parameter τ =4.

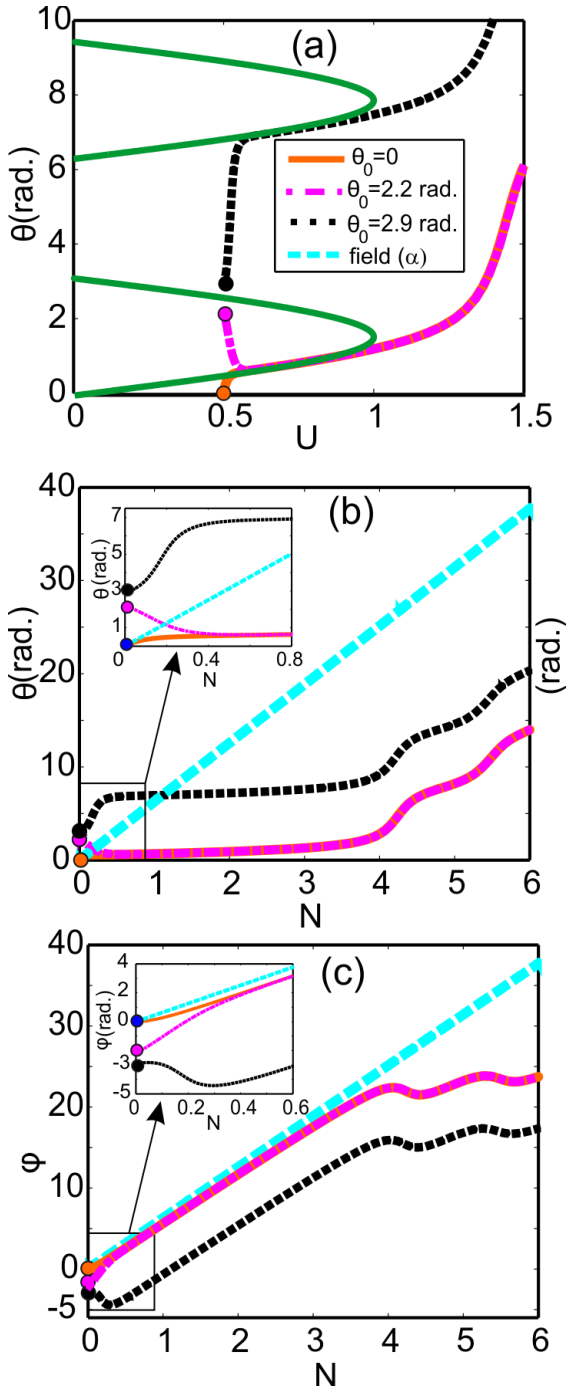

Figure 1.13 Nanorod behavior at three initial conditions, θ_0 = 0, 2, and 2.9 radians. (a) phase portrait of Eq. (1.17) showing the solution behavior for these initial conditions, (b) numerical θ-solutions as a function of the number of turns, *N*= *t*·*f*, (c) numerical φ -solutions as a function of the number of turns.

Figure 1.13 (a) shows three different dependencies of angle θ on parameter U at different initial conditions θ_0, and the same $U(0) = 0.5$. In this region, the derivative $d\theta/dU$ is positive because $U>\sin(\theta)$, Eq. (1.17). The magnetic field and nanorod magnetization are initially co-aligned, $\theta_0 =0$, solid line in Figure 1.13 (a),(b) and (c), and after approximately 0.2 revolutions, the angle θ stops changing. This implies that the nanorods are caught by the field and from this moment they rotate with the field at the same frequency (solid line in Figure 1.13 (c)). Then after rotation in unison with the field for approximately 2 revolutions, the frequency of nanorod rotation starts to slow down. The nanorod sways back for the first time at $N_{cr}=4$.

The dash-dot trajectory corresponding to the initial condition $\theta_0 =2$ in Figure 1.13 (a),(b) and (c) shows the distinct features of the trajectories with initial conditions taken in the region $U<\sin(\theta)$. In this region, the derivative $d\theta/dU$ is negative because $U<\sin(\theta)$, Eq. (1.17). Therefore, the angle θ decreases with time implying that the magnetic field rotates toward the direction of the nanorod magnetization and the angle between them decreases. After approximately 0.2 revolutions, the angle θ stops changing. This means that the nanorods are caught by the field and from this moment they rotate with the field at the same frequency repeating the behavior of nanorods which started at $\theta_0 = 0$. (the dash-dot line in Figure 1.13 (c)). Then after rotation in unison with the field for approximately 2 revolutions, the frequency of nanorod rotation starts to slow down. The nanorod sways back for the first time at $N_{cr}=4$.

The dotted trajectory corresponding to the initial condition θ_0 =2.9 in Figure 1.13 (a),(b) and (c)) elucidates the distinct features of the trajectories with the initial conditions taken in the region $U>\sin(\theta)$. In this region, the derivative $d\theta/dU$ is positive because $U>\sin(\theta)$, eq (7). Accordingly, the angle θ is first increasing and after about 0.2 revolutions it stops changing. This means that the nanorods are caught by the field and from this moment they rotate with the field at the same frequency repeating the behavior of nanorods which started at θ_0 = 0 and 2 radians. After two revolutions nanorods starts to slow down and then sways back for the first time at N_{cr}=4.

For all of these three cases, the parameter N_{cr} is the same and it is equal to $N_{cr} \cong 4$. From the numerical analysis, we conclude that the behavior of nanorods at the first moments of time does depend on angle θ_0 , but the critical number of turns N_{cr} does not depend on the initial orientation of the nanorods.

1.3.3 Effect of β - parameter on nanorod dynamics.

Effect of the β-parameter, i.e. the initial condition U(0), can be explained by following the trajectories corresponding to β = U_0 = 0.3, 0.5, and 0.7 and assuming that the initial angle θ_0 = 0. The dependencies of functions θ and φ on time are presented in Figure 1.14 where we have chosen the τ =4.

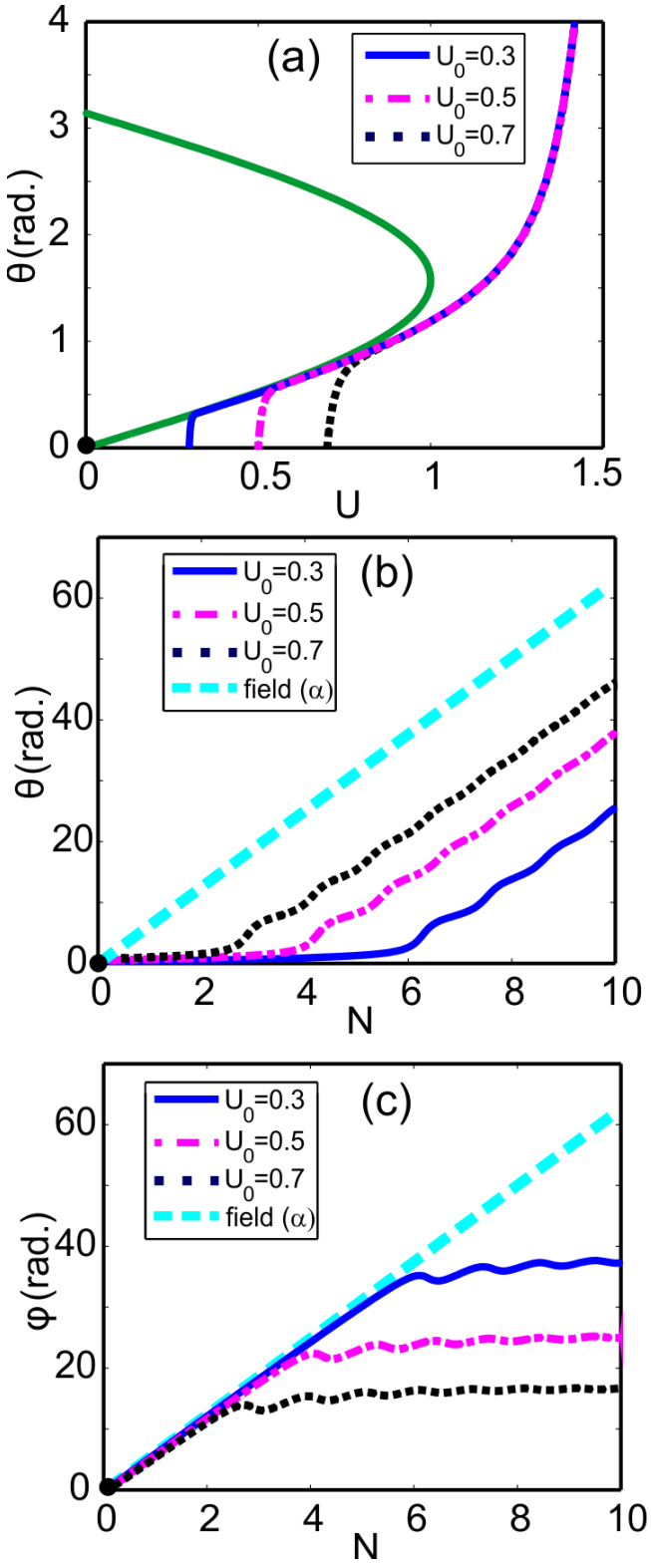

Figure 1.14 Nanorod behavior at different initial conditions β = U(0) = 0.3, 0.5, 0.7 (a) Phase portrait of Eq. (7) showing the solution behavior for different initial conditions U (0) at $\theta_0 = 0$, (b) the numerical θ - solutions as a function of the number of turns, $N = t \cdot f$,(c) the numerical φ -solutions as a function of the number of turns.

Figure 1.14 reveals that the nanorod behavior for different β does not change significantly: the behavior of the θ and φ-solutions are very similar to each other. At initial moments of time, the nanorod trajectory and the field angle trajectory coincide, i.e. the nanorods are co-aligned with the field and revolve with the same frequency as that of the driving magnetic field, Figure 1.14 (c). The nanorod keeps rotating until it reaches a critical number of turns, N_{cr} . This critical number depends on the initial conditions, for example, $N_{cr}(0.3) = 2.8$, $N_{cr}(0.5)=4$, $Ncr(0.7) = 6.1$. The lower the beta-parameter, the greater the critical number of turns. As follows from Eq. (1.15), the beta-parameter can be decreased by decreasing initial viscosity, by making the nanorod shorter, by applying a stronger magnetic field, or by decreasing the frequency of rotation of the applied magnetic field.

This numerical analysis of Eq. (1.17) allows one to design the MRS experiments with different materials and estimate the critical parameters such as the critical number of turns or τ -parameter specific for different liquid-nanorod pairs.

1.4 Conclusions

We theoretically developed a method which can be used for the rheological measurements of polymer systems, aerosol droplets with thickeners and biofluids at the microscale. First, we developed the analytical and numerical models describing the nanorod behavior in rotating magnetic fields. We introduced an important parameter, the critical frequency f_{cr} at which magnetic nanorods starts rotating asynchronously with the driving magnetic field. This parameter can be found

experimentally and then substituted into our model to calculate the viscosity of the carrying fluid. We used analytical and numerical models to predict the behavior of magnetic nanorods with different magnetic and geometrical properties in liquids with different viscosities. It was shown that the nanorods with aspect ratio lower than 16 can be used to probe viscosities up to 1500 mPa*s at magnetic fields B=0.0015T. This field can be generated by small, inexpensive commercially available electromagnets. In order to probe viscosities up to 10000 mPa*s one needs to design a magnetic system which can generate rotating magnetic fields with magnitude B=0.01T. The described method was used to measure rheological properties of liquids in microdroplets with constant viscosity. Experimental protocols and calculations are described in Chapter 3. Proposed method can also be used to characterize magnetic properties of nanorods when the viscosity of surrounding liquid is known. We used this method to characterize magnetic properties of nickel nanorods synthesized in our laboratory. Experimental protocols and calculations of magnetic properties of nanorods are described in Chapter 3.

We then modified our numerical model to study the nanorod behavior in a non-Newtonian fluid with exponentially increasing viscosity. Photopolymerization of HEMA was chosen as an example of a fluid with exponentially changing viscosity. We conducted full numerical analysis and summarized results in a form of a phase diagram which can be used to study the system behavior at different initial conditions (initial angle between nanorod and magnetic field, initial viscosity of the liquid, geometrical and magnetic properties of nanorod, frequency and magnitude of magnetic field). We theoretically described an important parameter $N_{cr.}$- the number

of turns that the nanorod takes on before it sways back for the first time. Based on these calculations we described an experimental protocol where one needs to measure N_{cr} and use τ as an adjustable parameter to fit the experimental N_{cr} with the theoretical one. This protocol was used to measure the viscosity of HEMA undergoing photopolymerization process. Experimental procedure and results from these measurements are described in Chapter 4.

We believe that the described methods will provide materials scientists and chemists with a unique tool to probe and map the physico-chemical properties of sophisticated microsystems in short time intervals.

1.5 References

1. Larson, R.G., *The structure and rheology of complex fluids*. Topics in Chemical Engineering, ed. K.E. Gubbins, 1999, New York: Oxford University Press. 663.

2. Barabino, G.A., M.O. Platt, and D.K. Kaul, *Sickle Cell Biomechanics*, in *Annual Review of Biomedical Engineering, Vol 12*, M.L. Yarmush, J.S. Duncan, and M.L. Gray, Editors., 2010, Annual Reviews: Palo Alto. p. 345-367.

3. Aprelev, A., Z.H. Liu, and F.A. Ferrone, *The Growth of Sickle Hemoglobin Polymers*. Biophysical Journal, 2011. **101**(4): p. 885-891.

4. Zavyalova, E.G., et al., *Investigation of Early Stages of Fibrin Association.* Langmuir, 2011. **27**(8): p. 4922-4927.

5. Hall, C.E. and H.S. Slayter, *The fibrinogen molecule: its size, shape, and mode of polymerization.* The Journal of biophysical and biochemical cytology, 1959. **5**(1): p. 11-16.

6. Ferri, F., et al., *Growth kinetics and structure of fibrin gels.* Physical Review E, 2001. **63**(3).

7. Li, L. and L.J. Lee, *Photopolymerization of HEMA/DEGDMA hydrogels in solution.* Polymer, 2005. **46**(25): p. 11540-11547.

8. He, H., L. Li, and L.J. Lee, *Photopolymerization and structure formation of methacrylic acid based hydrogels: The effect of light intensity.* Reactive and Functional Polymers, 2008. **68**(1): p. 103-113.

9. Malkin, A.I.A. and A.I. Isayev, *Rheology concepts, methods, and applications*, 2006, ChemTec Pub.: Toronto, Ont.

10. Korolev, G.V. and M.M. Mogilevich, *Three-dimensional free-radical polymerization : cross-linked and hyper-branched polymers*, 2009, Berlin: Springer.

11. Sa, V. and K.G. Kornev, *A method for wet spinning of alginate fibers with a high concentration of single-walled carbon nanotubes.* Carbon, 2011. **49**(6): p. 1859-1868.

12. Wilhelm, C., F. Gazeau, and J.C. Bacri, *Rotational magnetic endosome microrheology: Viscoelastic architecture inside living cells.* Physical Review E, 2003. **67**(6).

13. Bausch, A.R., W. Möller, and E. Sackmann, *Measurement of Local Viscoelasticity and Forces in Living Cells by Magnetic Tweezers.* Biophysical Journal, 1999. **76**(1): p. 573-579.

14. Guigas, G., C. Kalla, and M. Weiss, *Probing the Nanoscale Viscoelasticity of Intracellular Fluids in Living Cells.* Biophysical Journal, 2007. **93**(1): p. 316-323.

15. Weihs, D., T.G. Mason, and M.A. Teitell, *Bio-Microrheology: A Frontier in Microrheology.* Biophysical Journal, 2006. **91**(11): p. 4296-4305.

16. Barrera, C., et al., *Monitoring gelation using magnetic nanoparticles.* Soft Matter, 2010. **6**(15): p. 3662-3668.

17. Erglis, K., et al., *Viscoelasticity of the bacteriophage Pf1 network measured by magnetic microrheology.* Magnetohydrodynamics, 2010. **46**(1): p. 23-29.

18. Huisman, E.M., et al., *Gelation of semiflexible polyelectrolytes by multivalent counterions.* Soft Matter, 2011. **7**(16): p. 7257-7261.

19. McNaughton, B.H., et al., *Physiochemical microparticle sensors based on nonlinear magnetic oscillations.* Sensors and Actuators B-Chemical, 2007. **121**(1): p. 330-340.

20. Samouhos, S. and G. McKinley, *Carbon nanotube-magnetite composites, with applications to developing unique magnetorheological fluids.* Journal of Fluids Engineering-Transactions of the Asme, 2007. **129**(4): p. 429-437.

21. Korneva, G., et al., *Carbon nanotubes loaded with magnetic particles.* Nano Letters, 2005. **5**(5): p. 879-884.

22. Tokarev, A., et al., *Magnetic Nanorods for Optofluidic Applications.* AIP Conference Proceedings, 2010. **1311**: p. 204-209.

23. Allione, M., et al., *Rod-shaped nanostructures based on superparamagnetic nanocrystals as viscosity sensors in liquid.* Journal of Applied Physics, 2011. **110**(6).

24. Frka-Petesic, B., et al., *Dynamics of paramagnetic nanostructured rods under rotating field.* Journal of Magnetism and Magnetic Materials, 2011. **323**(10): p. 1309-1313.

25. Anguelouch, A., R.L. Leheny, and D.H. Reich, *Application of ferromagnetic nanowires to interfacial microrheology.* Applied Physics Letters, 2006. **89**(11): p. 111914.

26. Possin, G.E., *A method for forming very small diameter wires.* Review of Scientific Instruments, 1970. **41**(5): p. 772.

27. Bentley, A.K., et al., *Suspensions of nickel nanowires as magneto-optical switches.* Nanotechnology, 2005(10): p. 2193-2196.

28. Kornev, K.G., et al., *Magnetostatic interactions between carbon nanotubes filled with magnetic nanoparticles.* Applied Physics Letters, 2008. **92**(23): p. Article Number: 233117

29. Klein, T., et al., *Magnetic-field-dependent optical transmission of nickel nanorod colloidal dispersions.* Journal of Applied Physics, 2009. **106**(11): p. Article Number: 114301.

30. Safi, M., et al., *Interactions between Magnetic Nanowires and Living Cells: Uptake, Toxicity, and Degradation.* ACS Nano, 2011. **5**(7): p. 5354-5364.

31. Shen, T.H., et al., *Magnetic nanowires fabricated by anodic aluminum oxide template-a brief review.* Science China-Physics Mechanics & Astronomy, 2011. **54**(7): p. 1181-1189.

32. Kou, X., et al., *Memory Effect in Magnetic Nanowire Arrays.* Advanced Materials, 2011. **23**(11): p. 1393-1397.

33. Celedon, A., Christopher M. Hale, and D. Wirtz, *Magnetic Manipulation of Nanorods in the Nucleus of Living Cells.* Biophysical Journal, 2011. **101**(8): p. 1880-1886.

34. Carignan, L.P., et al., *Ferromagnetic Nanowire Metamaterials: Theory and Applications.* Ieee Transactions on Microwave Theory and Techniques, 2011. **59**(10): p. 2568-2586.

35. Bellan, L.M., D. Wu, and R.S. Langer, *Current trends in nanobiosensor technology.* Wiley Interdisciplinary Reviews-Nanomedicine and Nanobiotechnology, 2011. **3**(3): p. 229-246.

36. Song, M.M., et al., *Cytotoxicity and cellular uptake of iron nanowires.* Biomaterials, 2010. **31**(7): p. 1509-1517.

37. Schlorb, H., et al., *Magnetic nanowires by electrodeposition within templates.* Physica Status Solidi B-Basic Solid State Physics, 2010. **247**(10): p. 2364-2379.

38. Ali, G., et al., *Characterization of Cobalt Nanowires Fabricated in Anodic Alumina Template Through AC Electrodeposition.* Nanotechnology, IEEE Transactions, 2010. **9**(2): p. 223-228.

39. Zhang, L.Y. and Y.F. Zhang, *Fabrication and magnetic properties of Fe(3)O(4) nanowire arrays in different diameters.* Journal of Magnetism and Magnetic Materials, 2009. **321**(5): p. L15-L20.

40. Tuboltsev, V. and J. Raisanen, *Ion beam processing of Au nanowires.* Nanotechnology, 2009. **20**(33).

41. Talapatra, S., et al., *Synthesis and characterization of cobalt-nickel alloy nanowires.* Journal of Materials Science, 2009. **44**(9): p. 2271-2275.

42. Gao, J. and B. Xu, *Applications of nanomaterials inside cells.* Nano Today, 2009. **4**(1): p. 37-51.

43. Celedon, A., et al., *Magnetic Tweezers Measurement of Single Molecule Torque.* Nano Letters, 2009. **9**(4): p. 1720-1725.

44. Pardavi-Horvath, M., et al., *Interaction effects in Permalloy nanowire systems.* Journal of Applied Physics, 2008. **103**(7): p. 07D517.

45. Sarkar, J., G. Khan, and A. Basumallick, *Nanowires: properties, applications and synthesis via porous anodic aluminium oxide template.* Bulletin of Materials Science, 2007. **30**(3): p. 271-290.

46. Choi, D., et al., *Transport of living cells with magnetically assembled nanowires.* Biomedical Microdevices, 2007. **9**(2): p. 143-148.

47. Vuppu, A.K., A.A. Garcia, and M.A. Hayes, *Video Microscopy of Dynamically Aggregated Paramagnetic Particle Chains in an Applied Rotating Magnetic Field.* Langmuir, 2003. **19**(21): p. 8646-8653.

48. Sun, L., et al., *Tuning the properties of magnetic nanowires.* Ibm Journal of Research and Development, 2005. **49**(1): p. 79-102.

49. Chen, M., et al., *Tuning the response of magnetic suspensions.* Applied Physics Letters, 2003. **82**(19): p. 3310-3312.

50. Chen, M., P.C. Searson, and C.L. Chien, *Micromagnetic behavior of electrodeposited Ni/Cu multilayer nanowires.* Journal of Applied Physics, 2003. **93**(10): p. 8253-8255.

51. Evans, P.R., G. Yi, and W. Schwarzacher, *Current perpendicular to plane giant magnetoresistance of multilayered nanowires electrodeposited in anodic aluminum oxide membranes.* Applied Physics Letters, 2000. **76**(4): p. 481-483.

52. Dubois, S., et al., *Evidence for a short spin diffusion length in permalloy from the giant magnetoresistance of multilayered nanowires.* Physical Review B, 1999. **60**(1): p. 477-484.

53. Piraux, L., et al., *The temperature dependence of the perpendicular giant magnetoresistance in Co/Cu multilayered nanowires.* European Physical Journal B, 1998. **4**(4): p. 413-420.

54. Maurice, J.L., et al., *Microstructure of magnetic metallic superlattices grown by electrodeposition in membrane nanopores.* Journal of Magnetism and Magnetic Materials, 1998. **184**(1): p. 1-18.

55. Dubois, S., et al., *Perpendicular giant magnetoresistance of NiFe/Cu multilayered nanowires.* Applied Physics Letters, 1997. **70**(3): p. 396-398.

56. Piraux, L., et al., *Giant magnetoresistance in magnetic multilayered nanowires.* Applied Physics Letters, 1994. **65**(19): p. 2484-2486.

57. Tsai, C.-C., et al., *Nanoporous Artificial Proboscis for Probing Minute Amount of Liquids.* Nanoscale, 2011.

58. Blums, E., A.O. Sebers, and M.M. Maiorov, *Magnetic fluids*,1997, Berlin ; New York: Walter de Gruyter. xii, 416 p.

59. Frenkel, I.A.I.i., *Kinetic theory of liquids*1955, New York,: Dover Publications. xi, 488 p.

60. Landau, L.D. and E.M. Lifshitz, *Electrodynamics of continuous media*1960, Oxford: Pergamon. 417.

61. Blums, E., A. Cebers, and M.M. Maiorov, *Magnetic fluids*, 1997, New York: Walter de Gruyter 416.

62. Doi, M. and S.F. Edwards, *The theory of polymer dynamics*. International series of monographs on physics, 1988, Oxford: Clarendon Press. xiii, 391 p.

63. Thongmee, S., et al., *Fabrication and magnetic properties of metallic nanowires via AAO templates.* Journal of Magnetism and Magnetic Materials, 2009. **321**(18): p. 2712-2716.

64. Fert, A. and L. Piraux, *Magnetic nanowires.* Journal of Magnetism and Magnetic Materials, 1999. **200**(1-3): p. 338-358.

65. Bentley, A.K., et al., *Template Synthesis and Magnetic Manipulation of Nickel Nanowires.* Journal of Chemical Education, 2005. **82**(5): p. 765.

66. Imran, M.M.A., *Structural and magnetic properties of electrodeposited Ni nanowires.* Journal of Alloys and Compounds, 2008. **455**(1-2): p. 17-20.

67. Cao, G. and D. Liu, *Template-based synthesis of nanorod, nanowire, and nanotube arrays.* Advances in Colloid and Interface Science, 2008. **136**(1-2): p. 45-64.

68. Aravamudhan, S., et al., *Porous silicon templates for electrodeposition of nanostructures.* Applied Physics a-Materials Science & Processing, 2007. **87**(4): p. 773-780.

69. Xue, S.H. and Z.D. Wang, *Metal nanorod arrays and their magnetic properties.* Materials Science and Engineering B-Solid State Materials for Advanced Technology, 2006. **135**(1): p. 74-77.

70. Tang, X.T., G.C. Wang, and M. Shima, *Superparamagnetic behavior in ultrathin CoNi layers of electrodeposited CoNi/Cu multilayer nanowires.* Journal of Applied Physics, 2006. **99**(12).

71. Piraux, L., et al., *Magnetic and superconducting nanowires.* Journal of Nanoscience and Nanotechnology, 2005. **5**(3): p. 372-389.

72. Li, D., T. Herricks, and Y.N. Xia, *Magnetic nanofibers of nickel ferrite prepared by electrospinning.* Applied Physics Letters, 2003. **83**(22): p. 4586-4588.

73. Vazquez, M., *Soft magnetic wires.* Physica B, 2001. **299**(3-4): p. 302-313.

74. Ge, S.H., et al., *Fabrication of electro deposited Co nanowire arrays with perpendicular anisotropy.* Journal of Magnetism and Magnetic Materials, 2001. **226**: p. 1867-1869.

75. Coey, J.M.D. and G. Hinds, *Magnetic electrodeposition.* Journal of Alloys and Compounds, 2001. **326**(1-2): p. 238-245.

76. Yellen, B.B., O. Hovorka, and G. Friedman, *Arranging matter by magnetic nanoparticle assemblers.* Proceedings of the National Academy of Sciences of the United States of America, 2005. **102**(25): p. 8860-8864.

77. Gosse, C. and V. Croquette, *Magnetic tweezers: Micromanipulation and force measurement at the molecular level.* Biophysical Journal, 2002. **82**(6): p. 3314-3329.

78. Barbic, M., *Magnetic wires in MEMS and bio-medical applications.* Journal of Magnetism and Magnetic Materials, 2002. **249**(1-2): p. 357-367.

79. Wilson, L.G. and W.C.K. Poon, *Small-world rheology: an introduction to probe-based active microrheology.* Physical Chemistry Chemical Physics, 2011. **13**(22): p. 10617-10630.

80. Llandro, J., et al., *Magnetic biosensor technologies for medical applications: a review.* Medical & Biological Engineering & Computing, 2010. **48**(10): p. 977-998.

81. Tierno, P., et al., *Overdamped dynamics of paramagnetic ellipsoids in a precessing magnetic field.* Physical Review E, 2009. **79**(2): p. 021501.

82. Keshoju, K., H. Xing, and L. Sun, *Magnetic field driven nanowire rotation in suspension.* Applied Physics Letters, 2007. **91**(12): p. 123114.

83. Paivo, K., et al., *High frequency asynchronous magnetic bead rotation for improved biosensors.* Applied Physics Letters, 2010. **97**(22): p. 223701.

2 SYNTHESIS OF NICKEL NANORODS AND DESIGN OF MAGNETIC MICROROTATOR FOR MICRORHEOLOGICAL STUDIES

2.1 Literature review on synthesis techniques of magnetic nanorods

Template-assisted electrochemical deposition method is widely used for preparation of magnetic nanorods [1-4]. The schematic of the three electrode system for the synthesis of nanorods is shown in Figure 2.1. The nanoporous template is covered with a conductive layer on one side and serves as a working electrode. Nanorods are formed in the pores of the template by electrodeposition of the metal from the counter electrode.

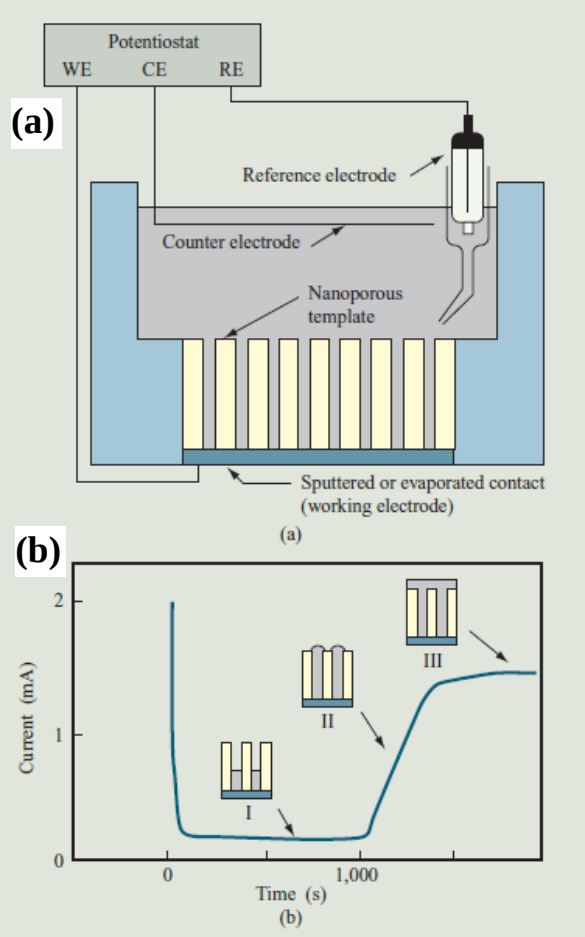

Figure 2.1 (a) Three-electrode cell for the electrodeposition of nanorods, (b) current behavior in the system during the electrodeposition process and corresponding stages of the membrane filling [5].

Anodized alimunum oxide (AAO) nanoporous membranes are usually used as templates [1, 6]. The main advantage of AAO membranes is that they have a narrow distribution of pore size and all pores have the same shape. Therefore, it is possible to synthesize nanorods with identical properties in AAO membranes. The pore diameters in this membranes is usually in the range from 5nm to 1μm and depth is up to 100 μm. Polymer membranes are less expensive compared to the alumina ones, but they have a broad non uniform distribution of pore sizes which leads to the synthesis of the nanorods with different properties [3]. Different metals (Ni, Fe, Co, Zn, etc.) and their

alloys can be electrodeposited inside of the membrane pores to form the rod-shaped structures. Properties of nanorods can be precisely controlled during the synthesis by varying conditions of elechtrochemical reaction. A typical hysteresis loop which shows the magnetic response of the ferromagnetic nanorods to an applied magnetic field is shown in the Figure 2.2. The features of the loop can be used to characterize magnetic properties of the material.

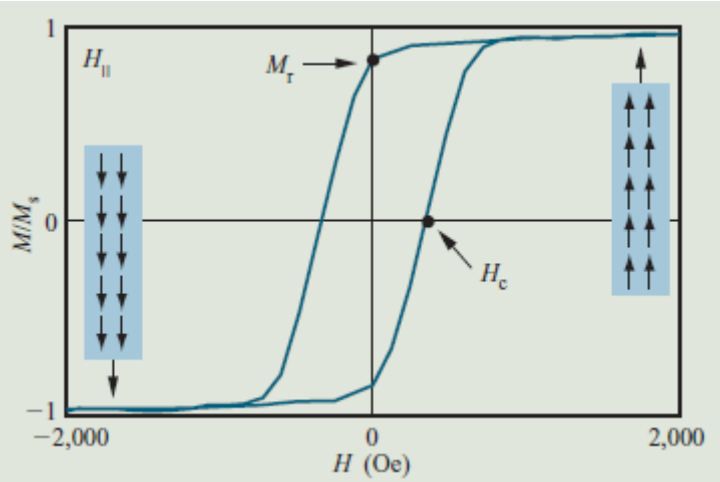

Figure 2.2 Hysteresys loop of an array of nickel nanorods with 100 nm in diameter [5].

The coercitivity H_c shows at what magnitude of the applied magnetic field the magnetization M of the sample becomes zero. The remanent magnetization M_r is introduced as the retained magnetization of the sample after turning off the applied field H. Ferromagnetic nanorods have non-zero magnetization in the absence of magnetic field. In order to reduce magnetization of ferromagnetic nanorods to zero, the magnetic field with magnitude H_c should be applied in the opposite direction.

Paramagnetic nanorods do not keep magnetization when the external magnetic field turns off. The way to produce magnetic nanorods with a paramagnetic behavior is to fill carbon nanotubes with superparamagnetic nanoparticles [7, 8].

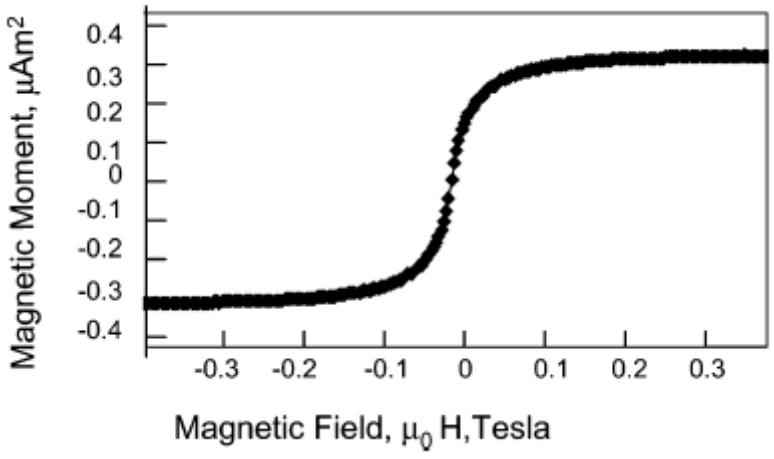

Figure 2.3 Typical magnetization curve of a nanotube membrane loaded with magnetic nanoparticles [7].

It can be seen from the Figure 2.3 that the nanotubes do not have a hysteresis loop on the magnetization curve thus demonstrating a paramagnetic behavior.

To conclude, magnetic nanorods with desired geometrical and magnetic properties can be produced by electrodeposition method. We used this method to synthesize nanorods which can be used for microrheological measurements. As shown in Chapter 1, the Ni nanorods with aspect ratios up to l/d=100 can be used to characterize rheological properties of liquids at the microscale. The details of electrochemical synthesis are provided below. First, we discuss the synthesis of nanorods for microrheological measurements and then we describe a device which can be used for nanorods manipulation and microrheological measurements.

2.2 Setup and experimental protocol for synthesis of nickel nanorods

From the theoretical analysis in Chapter 1 it can be seen that it is possible to probe picoliter volumes of liquids with viscosities up to 10000 mPa*s by using nickel nanorods with aspect ratio in the range of 4<l/d<100 (Figure 1.7, Figure 1.9) . To meet this requirements we have built a setup to synthesize nickel nanorods inside the pores of anodic aluminium oxide membranes by electrodeposition technique [3].

An alumina membrane (Whatman) with 0.2 µm pore sizes and 60 µm depth was used for the synthesis. The SEM image of this membrane is shown in the Figure 2.4

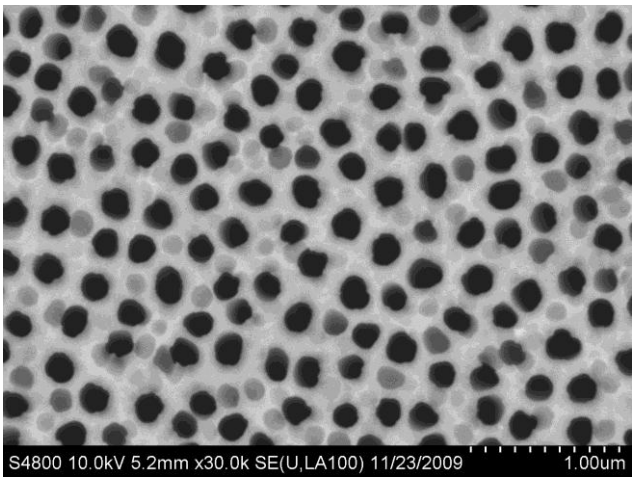

Figure 2.4 SEM image of alumina membrane used for synthesis of nickel nanorods (bottom)

In order to design a cathode for the electrodeposition system one side of the alumina membrane was covered with a conductive Gallium-Indium eutectic liquid. The membrane was placed on a glass slide with the bottom of the membrane facing up. A

small amount of Gallium-Indium (~20µL) was placed on the surface of the membrane and gently spread over the surface using a cotton swab until the entire back had a thin uniform coating on it.

A copper plate (76 x 38 x 4.2 mm^3) was cleaned using a high quality grade sand paper and then washed with a dishwashing liquid (Dawn Inc.). Once the plate has been cleaned, it was rinsed under tap water and dried completely before it was used. Cleaning process was needed to provide a good electrical contact between copper plate and conductive surface of the membrane. Next the membrane was lifted off of the glass slide and placed on the surface of copper plate (Figure 2.5). Then the membrane was sealed with water-proof tape and wax to prevent any contact of the copper plate with solution during the electrodeposition process. Electrical contact with a cathode is available only through the pores in the membrane.

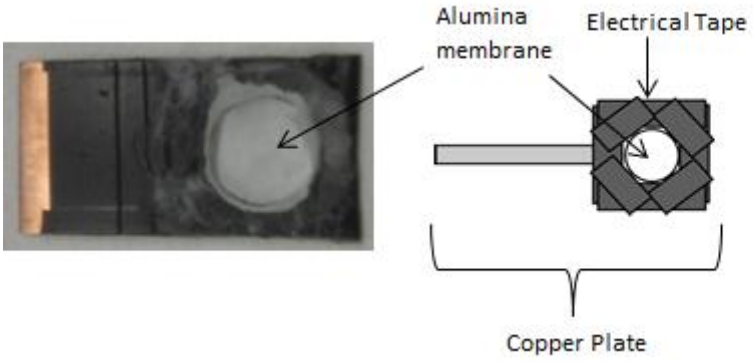

Figure 2.5 Copper plate cathode setup – alumina membrane is placed on the copper plate and is sealed to it with water-proof tape and wax leaving the surface of the membrane exposed to the Watts solution during the electrodeposition process.

The beaker was filled with the Watts solution (300 g/L $NiSO_4 \cdot 6H_2O$, 45 g/L H_3BO_3, and 45 g/L $NiCl_2 \cdot 6H_2O$) (Figure 2.6). The 1 mm nickel wire was used as anode and was placed on the opposite side from the cathode in a beaker .The DC regulated power supply (Gwinstek PSS-2005, Instek) was used to apply 1.5 V potential between anode and cathode. The power supply was controlled with a LabView program (National Instruments Corporation).

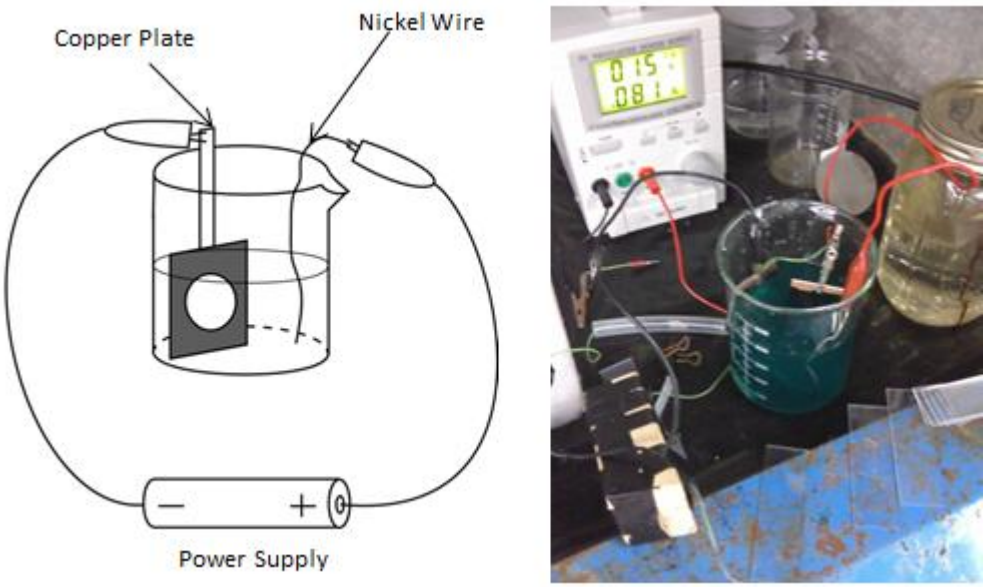

Figure 2.6 A diagram of the electrodeposition setup for synthesis of nickel nanorods.

In order to control the electrodeposition process, the reference electrode was used to measure the current during electrochemical reaction. Current behavior in the system is shown in Figure 2.7.

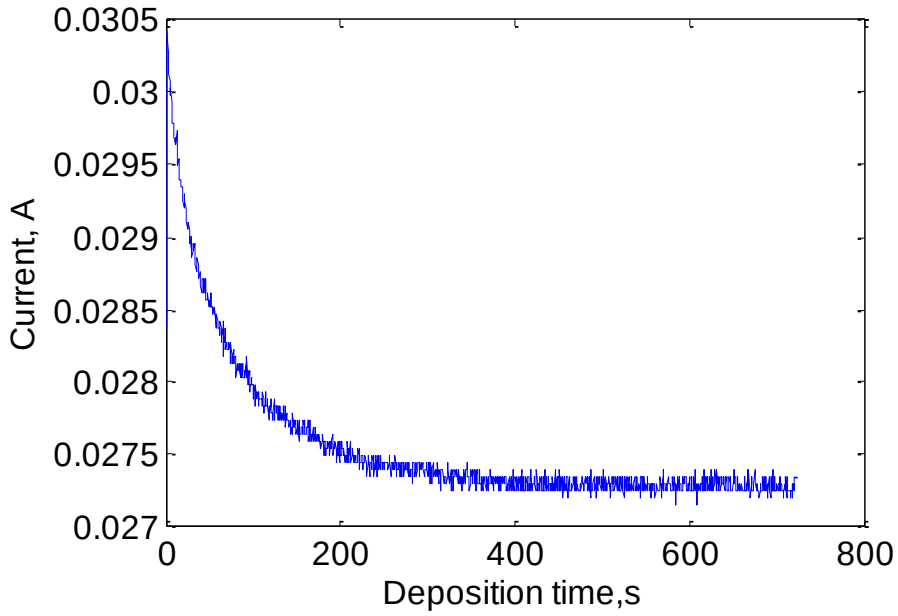

Figure 2.7 Time dependence of the current during the electrodeposition process of nanorods.

After the nickel electrodeposition was completed, the cathode was immersed in acetone for 10 minutes to remove the water-proof tape. Once the membrane was removed from the copper plate it was lightly taped to a microscope slide. A cotton applicator was first soaked in a nitric acid and then was used to remove the Gallium-Indium layer. The alumina membrane was dissolved in 10 mL of 6 M NaOH solution. Permanent neodymium magnet (K&J Magnetics®, DY81) was placed at the bottom of the beaker while nickel nanorods were rinsed several times with water. Ethylene glycol was added and a suspension of nickel nanorods was prepared by ultrasound sonication.

This setup was built for the synthesis of nanorods with desired geometrical and magnetic properties for the use in microrheological measurements (Chapter 1).

Diameter of the rods is controlled by pore size of the membrane and can be varied by using membranes with different size of the pores. The length of nanorods can be varied by the time of electrodeposition. The longer the electrodeposition time, the longer the nanorods will be produced. In order to produce nanorods of a given length we studied how the length of nanorods varies with changing the time of electrodepositiom. Three samples were prepared by electrodeposition technique with varied time of deposition (720, 1450 and 3300 seconds accordingly).

The diameter of all nanorods was controlled by the diameter of pores in alumina membrane and it was equal to 200.57±2.59nm (Figure 2.8).

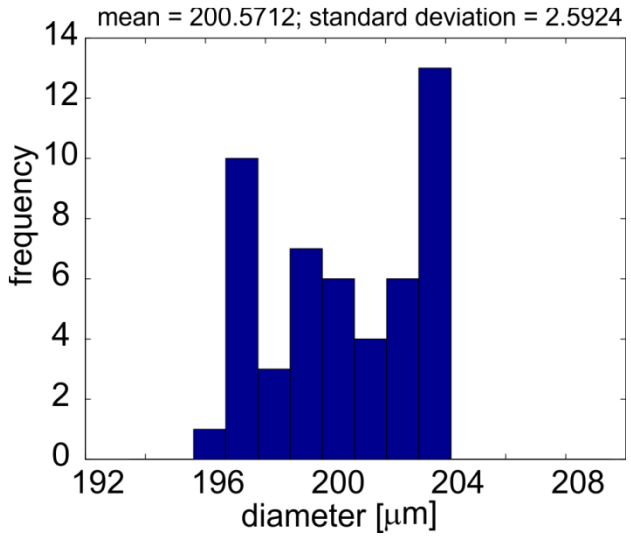

Figure 2.8 The pore size distribution for the alumina membrane which was used in the nanorods synthesis.

After the membrane was dissolved, ultrasound sonication was applied for 30 seconds for each sample in order to produce dispersion of nanorods in ethylene glycol. A

droplet with magnetic nanorods(~10µL) was placed on a Si wafer, dried in the oven at 200^0C and the length of nanorods was measured by scanning electron microscope (SEM) Hitachi S4800. The SEM images were processed with ImageJ (NIH) and MatLab to get the nanorod length distributions. The SEM images and corresponding length distributions are shown in the Figure 2.9.

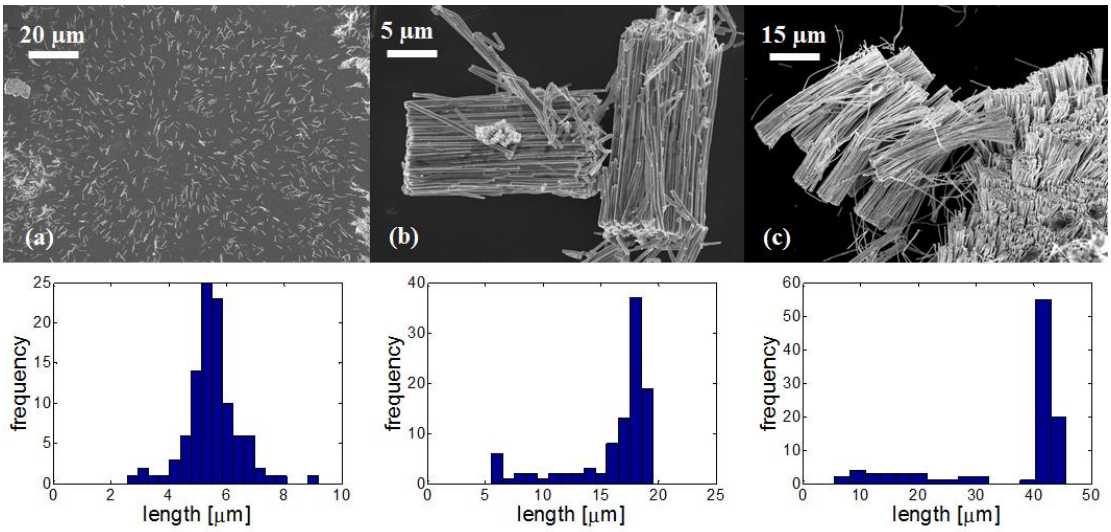

Figure 2.9 SEM pictures and size distributions for 3 samples with different electrodeposition times (a) sample 1, *l*=5.5±0.93 µm(t=720sec.), (b) sample (2), *l*=16.03±3.71 µm(t=1450 seconds), (c) sample 3, *l*=36.43±11.67µm (t=3330 seconds).

A longer electrodeposition time results in an increased length of nanorods in the sample, Figure 2.9. It can also be noticed that the size distribution of nanorods becomes wider with an increased length of the nanorods. This can be explained by the nanorod mechanical instability: the longer nanorods break more easily than the shorter ones during the ultrasound sonication process. The time of ultrasound sonication for all samples was 30 seconds. This time is enough to break some of the

rods which are longer than 10 μm. The best size distribution of nanorods was achieved at the time of electrodeposition t=720s.

Faraday's law was used to calculate the length of nanorods depending on the time of electrodeposition:

$$m_f = \frac{Q \cdot M}{F \cdot z} \tag{2.1}$$

where m_f is the mass of the substance liberated at an electrode in grams, Q is the total electric charge passed through the substance, F = 96485 C mol^{-1} is the Faraday constant, M is the molar mass of the substance (58.6 g/mol for Ni), z is the valency number of ions of the substance (2 for nickel). The total charge Q is the electric current $I(t)$ integrated over time t:

$$Q = \int_{t_1}^{t_2} I dt \tag{2.2}$$

The total charge was calculated by integrating the graph from Figure 2.7 and it is equal to 20.5 A·s. The integration was done in MatLab by calculating the area under the curve with limits t_1=0 and t_2=720 seconds for Sample 1:

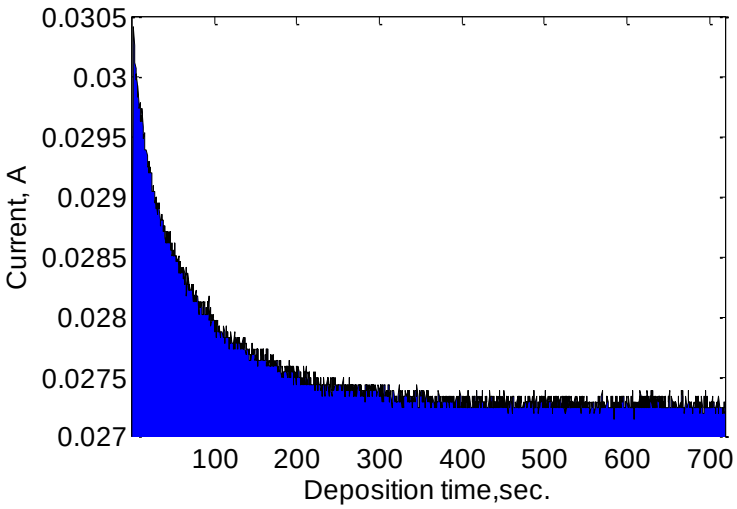

Figure 2.10 Area under the current-time curve calculated from the Eq. (2.2) in MathLab (limits t_1=0 and t_2=720).

Equation (2.1) estimate the mass m_f = 0.0062g of nickel deposited into pores of the membrane during electrodeposition. Assuming that the deposited nickel fills completely all the pores, one estimates the mass as

$$m_{theor} = p \cdot \rho \cdot S \cdot h \tag{2.3}$$

where p – porosity of the membrane (0.5), ρ – nickel density (8900 kg/m^2), S – area of the membrane exposed to solution (0.000119 m^2 for sample 1, 11x11 mm), h – height of the membrane (60 μm). The calculated m_{theor} for Sample 1 is 0.064g. The length of nanorods in Sample 1 can be estimated as:

$$h_r = h \cdot \frac{m_f}{m_{theor}} \tag{2.4}$$

The nanorod length h_r in Sample 1 calculated from Faraday's law is equal to 5.85 μm. The same procedure was used to calculate the length of nanorods in Samples 2 and 3. Theoretical and experimental results for all samples are summarized in Table 2.1 :

Table 2.1 Dependence of Ni nanorods length on electrodeposition time

Sample #	Time of electrode position, s	Area under the I(t) curve, A·s	Area of membrane exposed to electrodeposition, mmxmm	Length of the wires calculated from Faraday's law, μm	Length of the wires measured from SEM pictures, μm
1	720	20.5	11x11	5.85	5.5±0.93
2	1450	50.96	9x9	17.71	16.03±3.71
3	3330	91.24	9x9	39.11	36.43±11.67

As seen from the table, the length of nanorods calculated from the SEM pictures is in good agreement with the theoretical predictions based on Faraday's law. Therefore, the nanorods with any length up to 60 μm can be produced by controlling the time of electrodeposition.

To conclude, we successfully built an electrochemical setup which can be used tosynthesize nanorods with desired geometrical and magnetic properties. Diameter of nanorods can be varied by choosing membranes with desired pore size and length of the rods can be varied by the time of electrodeposition process. Magnetic properties of nanorods can be varied by using different metals and alloys (Ni, Fe, Co, Zn, etc.) as anodes in the setup shown in the Figure 2.6.

2.3 Litarature review on magnetic systems for manipulation of magnetic nanoparticles and microrheological measurements

Actuation and rotation of magnetic materials by applying alternating current (AC) magnetic field is an attractive method to probe the materials mechanical properties. Many materials can be made magnetic by embedding magnetic micro and nanoparicles which are available on the market or can be produced in the laboratory [9-11]. Magnetic nanoparticles with different shapes and surface functionalization are attractive candidates for the sensoric and diagnostic applications. Such applications call for the development of new devices providing controlled manipulation of the objects in question [2, 12-15]. Depending on the method of field generation, these devices can be split into two groups [16-18]. One group employs permanent magnets fixed on a movable stage/holder which can be shaken or spun to produce an AC field [17, 18]. Another group utilizes coils generating magnetic fields with a broad frequency band [7, 19-21].

The permanent magnets are attractive candidates because they provide high gradients of the magnetic field. When the stage with a magnet rotates or moves back and forth, the nanoparticles readily follow the generated field [17, 18, 22-26]. On the other hand, the frequency band generated by the moving stage is very narrow. This limits the application of permanent magnets.

Many practical applications require an AC field covering a broad frequency band. In this respect, electromagnets offer significant flexibility: the magnitude, direction, and frequency of the magnetic field can be remote controlled by simply changing the current on the magnetic coils. [20, 27] In optofluidic applications, when one needs to precise control the rotation and simultaneous observation of the magnetic particles, the system has to meet the following criteria: 1) the size of the micro-rotator has to be small enough to place it under the microscope objectives; 2) the setup must be flexible to ensure an easy change of the setup configuration by rearranging the coils or changing the distance between them; 3) the magnitude and frequency of the magnetic field have to be remotely controlled. Several groups have been working in the past years to apply electro-magnetic control in optofluidic devices [7, 20, 27-35].

In this respect, rotating magnetic field deserves special attention. Generation of the rotating magnetic field can be done with small Helmholtz coils having the cores measured in millimetres and even hundreds of microns. [30, 36-38]. Magnetic rotators with small Helmholtz coils can provide the rotation frequency in the range between 1 Hz to 1 kHz and the ten millitesla field strength [2, 7, 27, 31, 32, 34, 35, 39]. The strength and frequency of the magnetic field are limited by the coil ability to support high currents. It was shown that small water-cooled magnetic coils can maintain sufficiently high rotating magnetic fields [20].

In this chapter, we describe the development of a multifunctional magnetic rotator that has been designed for microrheological studies. Below, we explain the features of the proposed magnetic rotator.

2.4 Design of magnetic microrotator for microrheological measurements of fluids

Compact and versatile magnetic rotator was designed and used with Olympus BX51/MVX10 microscopes. The device circuit is shown in Figure 2.11 (a). In the schematic, we show the working head of the rotator that includes four solenoids with soft iron cores (Figure 2.11 (c)). In order to work with small optical cells that can be placed under a microscope, one needs sufficiently small solenoid coils with high inductance. We used 20.7mm diameter and 1.5mm thick coils (Solarbotics). The 6 mm diameter cylindrical cores made of soft iron were chosen long enough to deliver milliTesla range fields, the length depends on the application. The solenoids were assembled on a stage under the 50x microscope objective; see an example in Figure 2.11 (c).

The rotating magnetic field was generated using a waveform analog output PCI board (NI-PCI 6722) and custom 4-channel voltage-to-current converter. This NI-PCI 6722 board has 8 independent analog outputs and can produce signals with the frequencies up to 10 kHz. A LabVIEW 7 (NI) code allows one to generate four sinusoidal signals shifted by 90 degrees and smoothly converted to the voltage signal by an analog output board with a digitization frequency of about 200 kS/s per channel.

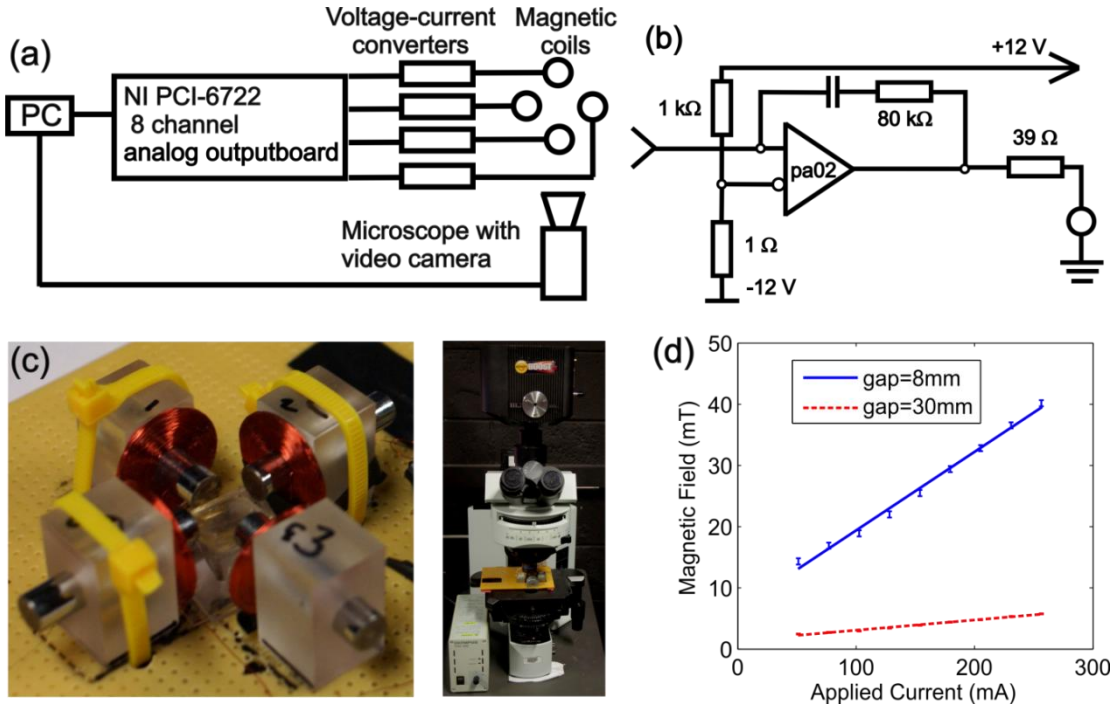

Figure 2.11 (a) Circuit of magnetic rotator, (b) circuit of the voltage-current converter, (c) magnetic rotator, (d) experimental measurements of the magnetic field in the middle of the two face-to-face placed coils as a function of applied current.

A circuit of the voltage-to-current converter is shown in Figure 2.11 (b). It is based on a 350kHz, 5A power amplifier, PA02 Cirrus Logic, Inc.. It is designed to drive the inductive loads and has a low crossover distortion. Using this highly integrated and relatively costly amplifier, one allows to keep the circuitry simple and any repair inexpensive. The generated current controls the strength and direction of the magnetic field in the field of view of the microscope.

For the applications requiring stronger magnetic fields, we used E-66-100 coils (15mm diameter and 8.5mm thick, Magnetic Sensor Systems). In order to analyze the strength of the magnetic field produced by these coils, two coils were placed face to face and magnetic field was measured using the digital teslameter (133-DG GMW

Inc.). The current-magnetic field curves are shown in Figure 2.11 (d) (the error bar represents a standard deviation from 3 measurements at each current)**.** One confirms that placing the coils 8mm apart, one can reach the 40 mT magnetic field. When the coil-to-coil distance was increased to 30mm, the field strength dropped down to 5 mT. A few milli-Tesla fields are sufficient enough to rotate magnetic nanoparticles [2, 27].

NI LabVIEW Signal Express (http://www.ni.com/labview/signalexpress/) was chosen to design a software to control the operation of magnetic micro-rotator. This software allows one to precise control the magnetic field and to simultaneously acquire images of the rotating objects during the experiments.

In our experiments, we examined the performance of four, three, and two magnetic coils. The software developed in LabVIEW is able to generate three types of magnetic fields: rotating, pulsating, and DC fields. Snapshot of the LabVIEW program window used for the signal generation is shown in the next figure:

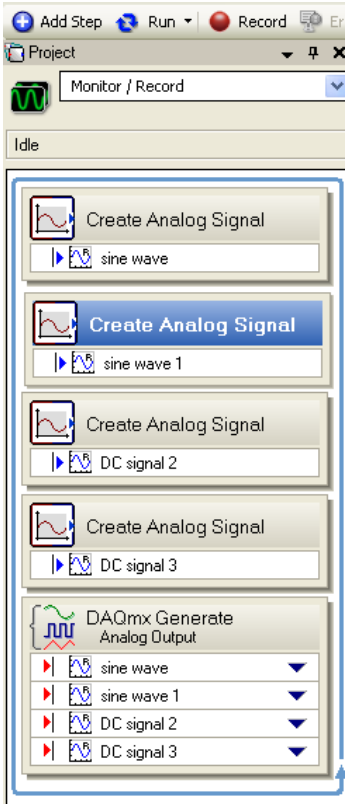

Figure 2.12 Snapshot of the LabVIEW program window used for the signal generation

First, an analog signal should be created in the program by specifying parameters of the signal in the "Create Analog Signal Box". As it can be seen from the figure, this signal can be either the AC (sin wave) or DC. After signals are created, an output route should be specified for each signal. Analog output board (Figure 2.11 (a)) has 8 output channels and analog signal generated in a LabVIEW program can be sent to either one of them. Output channel number should be specified in "DAQmx generate analog output" section (Figure 2.12 (a)). Output signal goes through the voltage-current converter remaining same properties (shape and frequency) and then it is sent to electromagnetic coils which produce magnetic field.

This system is able to produce three types of magnetic fields: the rotating, pulsating, and DC fields. These fields are controlled from the computer by a LabView program. An example of the LabView panel is shown in Figure 2.13**.** Different signal shapes can be generated, for example, DC – signal (b), square (c), sinusoidal (d), or triangle (e).

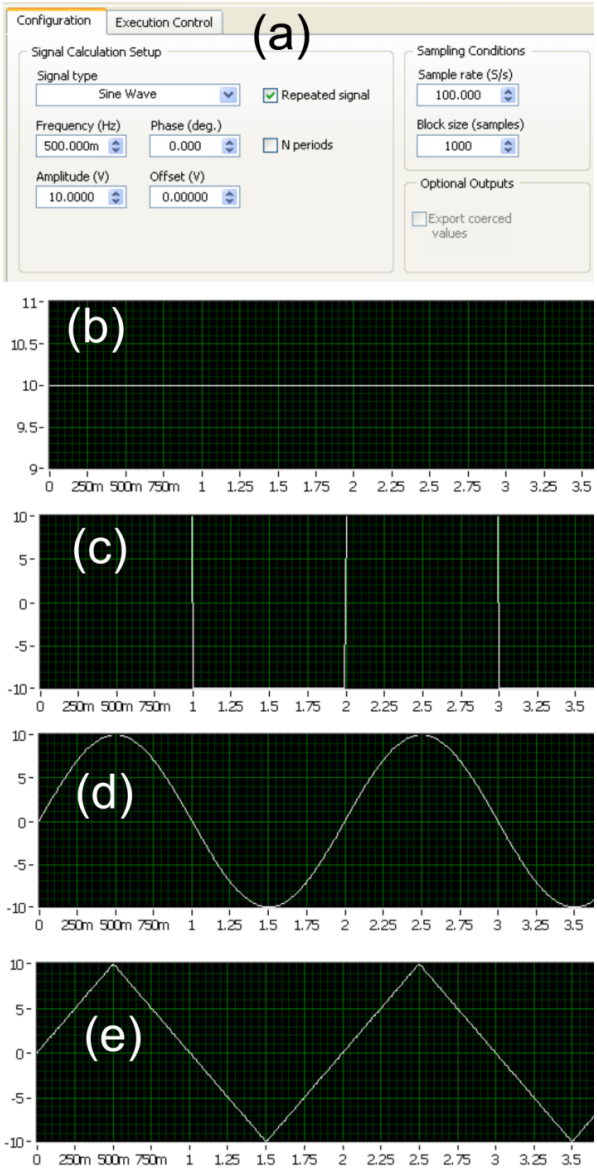

Figure 2.13 (a) LabView panel and different signal shapes generated by the LabVIEW program, (b) DC – signal, (c) square, (d) sinusoidal, or (e) triangle

The shape of the signal can be changed by setting up a formula for the signal (Figure 2.13 (a)) or by uploading the data file with a defined signal into the program. It can be seen from Figure 2.13 (a) that the Labview program allows one to control all properties of the signal – frequency, offset, and phase. The system was calibrated by sending the output signal from the LabView program and measuring the magnetic field at the center of the magnetic cell.

Rotating magnetic field is needed for microrheological analysis described in Chapter 1. It can be created as follows. Two coils of the magnetic rotator were fixed under the objective of BX-51 Olympus microscope (Figure 2.11). In order to produce a rotating magnetic field, two sinusoidal signals were sent to the coils with 90 degrees phase difference between them and rotation of magnetic nanorod was observed in the microscope equipped with a camera (Figure 2.14).

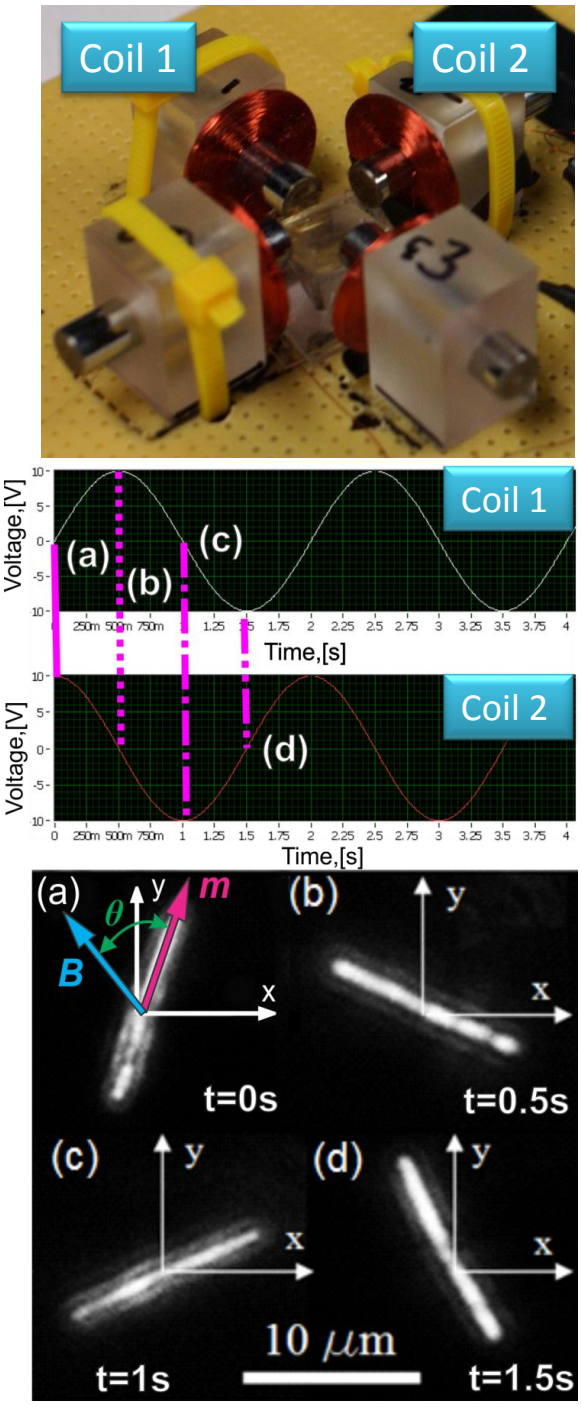

Figure 2.14 Two sinusoidal signals sent to two coils at the time moments (a),(b),(c) and (d). Following the generated rotating field, the nickel nanorod rotates clockwise at 0.5 Hz frequency.

This phase shift allows one to generate a rotating magnetic field. As it can be seen from the Figure 2.14 at the moment (a) the signal on the Coil 1 is zero and it is maximum on Coil 2. At the moment (b) signal on Coil 1 is maximum and it is zero on Coil 1. This arrangement allows one to generate a rotating magnetic field. Nanorod rotates with the same frequency as magnetic field (Figure 2.14). The frequency of the magnetic field set in the LabView program by changing the frequency of the sinusoidal signal sent to the coils. The magnitude of the magnetic field is determined by the amplitude of the sinusoidal signal which is set in the LabView program and can be changed during the experiment.

We developed a multifunctional magnetic rotator that allows one to generate rotating magnetic fields in a broad frequency band, from hertz to tens kilohertz. This system is able to produce magnetic field sufficient for the manipulation of magnetic nanoparticles and meets all requirements to be used for MRS.

2.5 Conclusions

To conclude, we successfully built an electrochemical setup which can be used tosynthesize nanorods for microrheological measurements described in Chapter 1. Diameter of nanorods can be varied by choosing membranes with desired pore size and length of the rods can be varied by the time of electrodeposition process. Magnetic properties of nanorods can be varied by using anode made from different materials. We successfully synthesized nickel nanorods 200nm in diameter with length in the range from 3 to 36 μm. As it can be seen from the theoretical analysis (Figure 1.9 (a)) nickel nanorods having aspect ratio l/d=15 can be used to probe fluids

with viscosities up to 600 mPa*s by rotating in the magnetic field with magnitude B=0.0015T. Morover, same nanorods might be used to probe fluids with viscosities up to 10000 mPa*s when the magnetic field is raised up to 0.01T.

Furthermore, we developed a multifunctional magnetic rotator that allows one to generate rotating magnetic fields in a broad frequency band, from hertz to tens kilohertz. We employed this system to study rheology of different fluids at the microscale level (Chapters 3 and 4). This system meets all requirements to be used for MRS: 1) the size of the system allows it to be placed under 50x microscope objective; 2) setup is flexible i.e. it is easy to rearrange coils and change distance between them; 3) magnitude and frequency of magnetic field is remotely controlled from the LabVIEW program. 4) the setup allows one to produce the AC as well as DC magnetic fields with up to 0.04T of magnitude. This system can also be used for microrheological studies in liquids with viscosities up to 10000mPa*s by replacing the coils with bigger ones which can produce rotating fields with magnitude up to 0.01T. We believe that this multifunctional magnetic system will be useful not only for micro and nanorheological studies, but it will find much broader applications requiring remote controlled manipulation of micro and nanoobjects.

2.6 References

1. Thongmee, S., et al., *Fabrication and magnetic properties of metallic nanowires via AAO templates.* Journal of Magnetism and Magnetic Materials, 2009. **321**(18): p. 2712-2716.

2. Tokarev, A., et al., *Magnetic Nanorods for Optofluidic Applications.* AIP Conference Proceedings, 2010. **1311**: p. 204-209.

3. Fert, A. and L. Piraux, *Magnetic nanowires.* Journal of Magnetism and Magnetic Materials, 1999. **200**(1-3): p. 338-358.

4. Bentley, A.K., et al., *Template Synthesis and Magnetic Manipulation of Nickel Nanowires.* Journal of Chemical Education, 2005. **82**(5): p. 765.

5. Sun, L., et al., *Tuning the properties of magnetic nanowires.* Ibm Journal of Research and Development, 2005. **49**(1): p. 79-102.

6. Shen, T.H., et al., *Magnetic nanowires fabricated by anodic aluminum oxide template-a brief review.* Science China-Physics Mechanics & Astronomy, 2011. **54**(7): p. 1181-1189.

7. Korneva, G., et al., *Carbon nanotubes loaded with magnetic particles.* Nano Letters, 2005. **5**(5): p. 879-884.

8. Kornev, K.G., et al., *Magnetostatic interactions between carbon nanotubes filled with magnetic nanoparticles.* Applied Physics Letters, 2008. **92**(23): p. Article Number: 233117

9. *Special Issue = Magnetic Nanoparticles* International Journal of Molecular Sciences, 2011. **12**(1).

10. Graham, D.L., H.A. Ferreira, and P.P. Freitas, *Magnetoresistive-based biosensors and biochips.* Trends in Biotechnology, 2004. **22**(9): p. 455-462.

11. Krishnan, K.M., *Biomedical Nanomagnetics: A Spin Through Possibilities in Imaging, Diagnostics, and Therapy.* Ieee Transactions on Magnetics, 2010. **46**(7): p. 2523-2558.

12. Wilhelm, C., *Out-of-equilibrium microrheology inside living cells.* Physical Review Letters, 2008. **101**(2): p. 028101.

13. Chi, X.Q., et al., *Nanoprobes for in vitro diagnostics of cancer and infectious diseases.* Biomaterials, 2012. **33**(1): p. 189-206.

14. Gao, J. and B. Xu, *Applications of nanomaterials inside cells.* Nano Today, 2009. **4**(1): p. 37-51.

15. Malynych, S.Z., et al., *Magneto-controlled illumination with opto-fluidics.* Journal of Magnetism and Magnetic Materials, 2010. **322**(14): p. 1894-1897.

16. Choi, D., et al., *Transport of living cells with magnetically assembled nanowires.* Biomedical Microdevices, 2007. **9**(2): p. 143-148.

17. Celedon, A., Christopher M. Hale, and D. Wirtz, *Magnetic Manipulation of Nanorods in the Nucleus of Living Cells.* Biophysical Journal, 2011. **101**(8): p. 1880-1886.

18. Evans, B.A., et al., *Magnetically Actuated Nanorod Arrays as Biomimetic Cilia.* Nano Letters, 2007. **7**(5): p. 1428-1434.

19. Hosu, B.G., et al., *Magnetic tweezers for intracellular applications.* Review of Scientific Instruments, 2003. **74**(9): p. 4158-4163.

20. Frka-Petesic, B., et al., *Dynamics of paramagnetic nanostructured rods under rotating field.* Journal of Magnetism and Magnetic Materials, 2011. **323**(10): p. 1309-1313.

21. Paivo, K., et al., *High frequency asynchronous magnetic bead rotation for improved biosensors.* Applied Physics Letters, 2010. **97**(22): p. 223701.

22. Vuppu, A.K., A.A. Garcia, and M.A. Hayes, *Video Microscopy of Dynamically Aggregated Paramagnetic Particle Chains in an Applied Rotating Magnetic Field.* Langmuir, 2003. **19**(21): p. 8646-8653.

23. Bausch, A.R., W. Möller, and E. Sackmann, *Measurement of Local Viscoelasticity and Forces in Living Cells by Magnetic Tweezers.* Biophysical Journal, 1999. **76**(1): p. 573-579.

24. Mosconi, F., J.F. Allemand, and V. Croquette, *Soft magnetic tweezers: A proof of principle.* Review of Scientific Instruments, 2011. **82**(3): p. 034302.

25. Celedon, A., et al., *Magnetic Tweezers Measurement of Single Molecule Torque.* Nano Letters, 2009. **9**(4): p. 1720-1725.

26. Hultgren, A., et al., *Cell manipulation using magnetic nanowires.* Journal of Applied Physics, 2003. **93**(10): p. 7554-7556.

27. Paivo, K., et al., *High frequency asynchronous magnetic bead rotation for improved biosensors.* Applied Physics Letters. **97**(22): p. 223701.

28. Yellen, B.B., O. Hovorka, and G. Friedman, *Arranging matter by magnetic nanoparticle assemblers.* Proceedings of the National Academy of Sciences of the United States of America, 2005. **102**(25): p. 8860-8864.

29. Gosse, C. and V. Croquette, *Magnetic tweezers: Micromanipulation and force measurement at the molecular level.* Biophysical Journal, 2002. **82**(6): p. 3314-3329.

30. Barbic, M., *Magnetic wires in MEMS and bio-medical applications.* Journal of Magnetism and Magnetic Materials, 2002. **249**(1-2): p. 357-367.

31. Wilson, L.G. and W.C.K. Poon, *Small-world rheology: an introduction to probe-based active microrheology.* Physical Chemistry Chemical Physics, 2011. **13**(22): p. 10617-10630.

32. Llandro, J., et al., *Magnetic biosensor technologies for medical applications: a review.* Medical & Biological Engineering & Computing, 2010. **48**(10): p. 977-998.

33. Tierno, P., et al., *Overdamped dynamics of paramagnetic ellipsoids in a precessing magnetic field.* Physical Review E, 2009. **79**(2): p. 021501.

34. Keshoju, K., H. Xing, and L. Sun, *Magnetic field driven nanowire rotation in suspension.* Applied Physics Letters, 2007. **91**(12): p. 123114.

35. Wilhelm, C., F. Gazeau, and J.C. Bacri, *Rotational magnetic endosome microrheology: Viscoelastic architecture inside living cells.* Physical Review E, 2003. **67**(6).

36. Barbic, M., et al., *Scanning probe electromagnetic tweezers.* Applied Physics Letters, 2001. **79**(12): p. 1897-1899.

37. Yapici, M.K. and J. Zou, *Permalloy-coated tungsten probe for magnetic manipulation of micro droplets.* Microsystem Technologies-Micro-and Nanosystems-Information Storage and Processing Systems, 2008. **14**(6): p. 881-891.

38. Yapici, M.K., et al., *Development and experimental characterization of micromachined electromagnetic probes for biological manipulation and stimulation applications.* Sensors and Actuators a-Physical, 2008. **144**(1): p. 213-221.

39. McNaughton, B.H., et al., *Sudden breakdown in linear response of a rotationally driven magnetic microparticle and application to physical and chemical microsensing.* Journal of Physical Chemistry B, 2006. **110**(38): p. 18958-18964.

3 MICRORHEOLOGICAL MEASUREMENTS WITH NICKEL NANORODS

3.1 Introduction

As shown theoretically in Section 1.2.3, magnetic nanorods can be used to study rheological properties of different liquids at the microscale level. In Section 2.2 we described a setup for nanorods synthesis. This setup allows one to synthesize nanorods with desired geometrical properties by varying the time of electrodeposition. Synthesized nanorods meet all requirements of the proposed MRS method. Furthermore, a multifunctional magnetic rotator (Section 2.4) allows one to generate rotating magnetic fields in a broad frequency band. Before starting microrheological experiments we need to characterize magnetic properties of synthesized nanorods. This chapter is organized as follows. First, we use the developed MRS method to characterize magnetic properties ofsynthesized Ni nanorods. We then use the obtained magnetic constants in rheological measurements of liquids and compare them to the bulk constants available in the literature and obtained with the cone-and-plate rheometer. We study the diffraction pattern from the system of aligned nanorods and study the reaction time of this reconfigurable lattice. We discuss a possible application of nanorods for optofluidic illumination in medical devices. We conclude with a summary of our findings.

3.2 Measuring magnetic properties of nickel nanorods

When magnetic nanorod is rotating in a simple Newtonian fluid and the frequency of the rotating magnetic field is increasing, we showed that there exists an important limiting frequency f_{cr} when the magnetic nanorod starts oscillating and revolving slower than the driving field. Obtaining f_{cr} from experiments in liquid with known viscosity, one can infer the magnetic moment of nanorods by solving Eq. (1.9) for m as

$$m = \frac{2\pi\gamma f_c}{B} \tag{3.1}$$

This formula has been used to measure the magnetic properties of nickel nanorods with different aspect ratios. Experimentally, the critical frequency was determined by rising up the frequency of the driving magnetic field and measuring the frequency of the nanorod rotation. An image tracking procedures was used to obtain the rate of rotation of magnetic nanorods (Video Spot Tracker; http://cismm.cs.unc.edu/downloads/). Two coils of the magnetic rotator were fixed under the objective of BX-51 Olympus microscope (Figure 2.11 (c)). In order to produce a rotating magnetic field, two sinusoidal signals were sent to the coils with 90 degrees phase difference between them (Figure 2.14). This phase shift allows one to generate a rotating magnetic field. The strength of the magnetic field was determined by the current as discussed in Section 2.4, and the amplitude of the sinusoidal signal which was set in the LabView program.

A 10µl droplet of ethylene glycol (η = 16 mPa·s) with the suspended nickel nanorods having the aspect ratios in the range $4<l/d<16$, was placed on a glass slide and investigated under the 50x objective of the BX-51 Olympus microscope. The measured magnetic field at the location of a droplet with the nanorod suspension was B = 0.0015T. We applied the dark field microscopy technique to detect the 200nm nanorods which were not visible in the bright field [1]. A SPOT videocamera (SPOT Imaging Solutions, Inc.) was used for filming the rotating nanorods. A high speed digital camera (Motion Pro X3, Red Lake, FL) was used to capture the images of the rotating magnetic nanorods at the frequencies higher than 25Hz. The captured videos were analyzed manually using VirtualDub software (http://www.virtualdub.org).

In order to exclude the interactions between the nanorods, we always double checked that the chosen nanorod was far away from their neighbours. The distance to the closest nanorod was at least 7 times greater than the nanorod length (Figure 3.1). This guarantees a weak dependence of nanorod behavior on dipole-dipole interactions as discussed in Ref. [2].

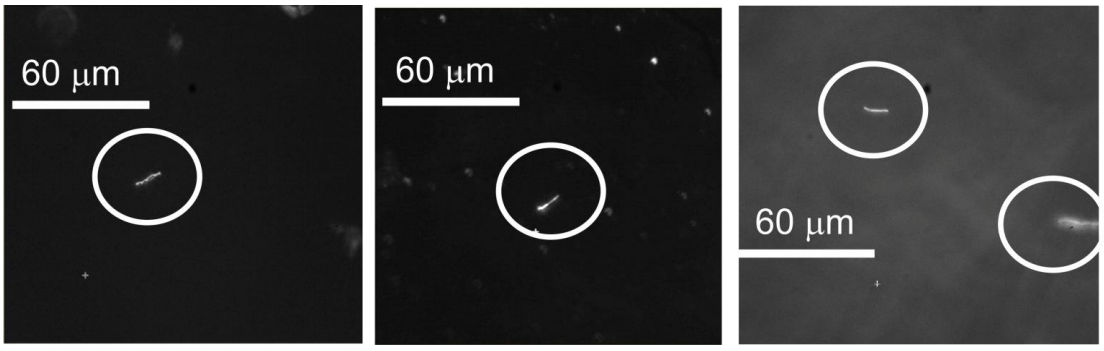

Figure 3.1 The circled nanorod was used in the MRS analysis. These pictures were taken from 3 different experiments to show that the closest neighbor is situated far away from the chosen nanorod. The width of the screen is 160 µm.

The recorded videos were used for the determination of a critical frequency of a particular nanorod. The critical frequency was measured for 6 nanorods having different aspect ratios. The dependence of the critical frequency on the rod aspect ratio is plotted in Figure 3.2, where experimental values are marked as red diamonds.

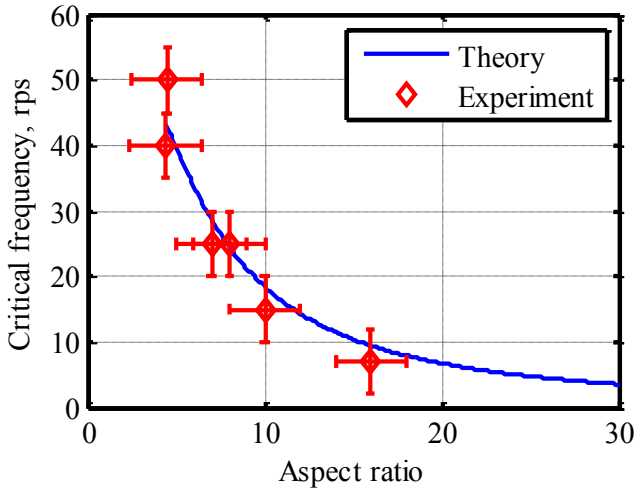

Figure 3.2 Critical frequency f_c up to which rotation of nickel nanorod is synchronized with rotation of the magnetic field as a function of nanorod aspect ratio *l*/*d*.

The literature data on magnetic properties of nickel nanorods demonstrate a significant scatter depending on the parameters used for the nanorod synthesis [3, 4]. This uncertainty suggests considering the magnetic moment of nanorod using a scaling relation:

$$m = vB\chi / \mu_0 \tag{3.2}$$

where *v* is the nanorod volume, μ_0 is the magnetic permeability of vacuum and χ is a magnetic constant of nanorod material. We used Eq. (3.3) for the least square fitting (χ as an adjustable parameter) the experimental data on critical rotation frequency f_c. The obtained best fit value provided χ = 92. (Figure 3.2, solid line).

After magnetic parameters of nanorods were obtained, we tested this method to measure viscosity of glycerol (Fisher Scientific Inc.) and its mixtures with water. First, we measured bulk viscosity with DV-III Ultra Rheometer (Brookfield Eng.), then conducted the MRS experiments and solved the following equations for η.

$$f_c = \frac{1}{2\pi}\frac{mB}{\gamma} \tag{3.3}$$

$$\gamma = \frac{\eta l^3 \pi}{3\ln(l/d) - A}, \tag{3.4}$$

Magnetic moments of nanorods were calculated by using Eq. (3.2) with parameter χ = 92. The results of MRS measurements are in a good agreement with the data obtained from the bulk measurements and available literature data (see Table 3.1).

Table 3.1 The results of MRS measurements, data obtained from the bulk measurements and available literature data.

Sample (22.5°C)	Bulk measurements with a rheometer (mPa*s)	MRS measurements (mPa*s)	Literature (22.5°C)
98% Glycerin +2% water	778	790±45	784[5]
89 %Glycerin+11%water	175	191±14	169[5]

These experiments confirmed that we can use the developed method and our setup to measure viscosities up to 790 mPa*s.

This theoretical and experimental analysis confirms the dependence of the critical frequency f_{cr} on aspect ratio of nanorods and allows one to use the MRS method to study magnetic properties of nanorods if the viscosity of the surrounding liquid is known. By measuring the viscosities of different fluids we confirmed that obtained value of magnetic constant χ=92 is valid and Eq. (3.2) can be used to calculate magnetic properties of nanorods. Magnetic properties of nanorods can vary significantly depending on the parameters used for nanorods synthesis. Therefore, one needs to calibrate each sample of synthesized nanorods to obtain magnetic constant χ before using these nanorods for microrheological measurements.

3.3 Measuring a temperature-dependent viscosity of a microdroplet

In the materials science applications, when a synthesized polymer is produced in a miniscule amount and the droplet size is measured in micrometers, the standard rheological instruments fall short to characterize the material. The MRS appears attractive because it provides a way to extract the rheological parameters of microdroplets by studying the rotational features of magnetic nanorods.

As can be seen from Figure 1.9 (a) using nickel nanorods with aspect ratio *l/d*=15 in the rotating magnetic field of magnitude B=0.0015T, it is possible to probe viscosities

up to 600 mPa*s. By reducing the aspect ratio of nanorods to *l/d*=10 it is possible to probe viscosities up to 1200mPa*s (Figure 1.8). In order to illustrate the robustness of the designed microrotator and to confirm the developed MRS theory (Section 1.2.3), we studied a temperature-dependent viscosity of microdroplets. Nickel nanorods were synthesized by using electrochemical template synthesis described in Section 2.2. A viscosity standard liquid S600 (Cannon Instrument Company) was used in these experiments. Viscosity of this liquid depends on the temperature. The temperature-viscosity curve is shown as a solid line in Figure 3.3 (a). This curve was generated using the table provided by the vendor with the data points marked by squares.

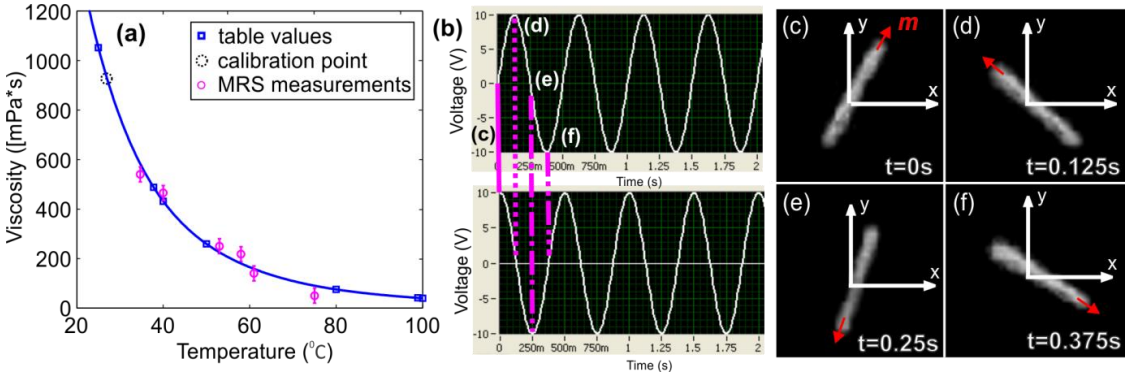

Figure 3.3 (a) Viscosity of the viscosity standard liquid S600 measured by rotation of the nanorods with different aspect ratios; squares and blue line show the table values of the viscosity; open circles show measured viscosity from 5 independent experiments with nanorods of different aspect ratios. A data point corresponding to the 927.5 mPa·s viscosity was used to obtain constant χ = 290, (b) Two sinusoidal signals sent to two coils at the time moments (c),(d),(e) and (f). Following the generated rotating field, the nickel nanorod rotates counter-clockwise at 2 Hz frequency.

Experimentally, the critical frequency was determined by increasing the frequency of the driving magnetic field and measuring the frequency of the nanorod rotation. Experimental details are described in Section 3.2. A 2µl droplet with the suspended Ni nanorods was placed on the insulated flexible heater made of a polymide film

(KA-808, Omegalux). A DC Regulated Power Supply (CSI12001X, Circuit Specialists) was connected to the film and was used to control the temperature of the film. The surface temperature was measured with a thermocouple connected to the temperature controller (TC-3300, CAL Controls LTD). We heated the 2 µL drop of viscosity standard liquid with nanorods dispersed in it up to 26.9^0C and used the calibrated viscosity η = 927.5 mPa·s (a dotted circle in Figure 3.3 (a)) given by the vendor. First, we experimentally determined f_c, the frequency at which the nanorod stopped rotating synchronously with the magnetic field. This viscosity value was used to obtain constant χ = 290. Then the temperature of the substrate was raised up and a critical frequency was measured at six different temperatures for different nanorods. When the critical frequencies were determined, the viscosity was calculated using Eqs. (3.3) and (3.4). The results of the viscosity measurements during the temperature rise (circles in Figure 3.3 (a)) are in a very good agreement with the values provided by the vendor. Therefore, this analysis confirms that the developed MRS model with the designed magnetic rotator provides correct viscosity data, hence the instrument can work as a nanorheological viscometer.

3.4 Manipulation of the diffraction pattern from nanorods with a rotating magnetic field and its applications for the illumination purposes

3.4.1 Introduction

Possible applications of magnetic liquids in optofluidics include optical modulators and switches. The properties and behavior of magnetic fluids from spherical nanoparticles have been studied for more than half a century. When a magnetic field

is applied to this fluid, the material becomes optically anisotropic, and different magneto-optical effects can be observed. Specifically, optical birefringence, Faraday rotation, dichroism and different types of light scattering were studied [6-9]. One of the most important effects is the diffraction pattern discovered by Haas [10]. In the applied magnetic field, the fluid becomes "frozen", forming chains of magnetic carriers directed along the field lines. When the light is applied perpendicular to the chains, an elongated characteristic diffraction pattern is formed on the screen (Figure 3.4 (a)).

While the optical effects from the dispersion of spherical particles were studied by many groups, the fluids with rod-like nanoparticles drew research interest only in recent years [2, 11-13]. Magnetic nanorods have great potential for applications in optofluidics because of their unique properties of high magnetization and structural stability, in contrast with chains of spherical particles.

Unlike traditional magnetic fluids, colloids of magnetic nanorods have several advantages in optofluidic applications. High magnetization of magnetic nanorods allows one to control the nanorods orientation using a moderate magnetic field. This offers the possibility to use miniaturized magnets with a lab-on-a-chip. Also, the nanorod solidity provides an easy way to manipulate the nanorod as a whole unit. For example, if the magnetic field (Figure 3.4 (a)) would rotate in the plane perpendicular to the direction of light propagation, the diffraction pattern would follow this rotation, enabling illumination of a large area. Moreover, by rotating nanorods in the plane perpendicular to the light beam, one can vary the transmission coefficient, enabling

intensity modulation [14]. In contrast to nanorods, the nanoparticle chains typically break in the rotating field [15]. We show that a suspension of nickel nanorods can be used for optofluidic applications where the precise control of light is needed but mechanical contact is not possible. In particular, we demonstrate that the light beam from a laser can be significantly diffracted by nickel nanorods and by rotating magnetic field one can illuminate a larger area.

3.4.2 Experimental set up

In the optical experiments, nickel nanorods of 200 nm in diameter and 10μm in length were suspended in ethylene glycol at different concentrations (0.0015-0.034 wt. %). The rectangular glass cell (1 mm thick) filled with the suspension was placed between two poles of GMW 3470 dipole electromagnet (Figure 3.4 (a)).

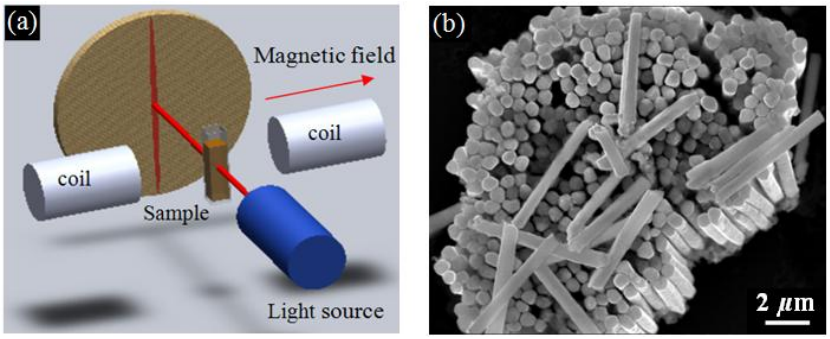

Figure 3.4 (a) Experimental setup for magneto-optical experiments, (b) Scanning electron micrograph of nickel nanorods

When magnetic field was applied perpendicular to the direction of beam propagation, we observed that the nanorods aligned along the field lines. He-Ne the laser beam

(632.8 nm) illuminated the cell with aligned rods, and the diffraction pattern was observed on the screen located at the distance of 16 cm from the optical cell. This pattern was similar to that of spherical nanoparticles [4, 16]. CCD camera (Dalsa Falcon 1.4M100) was used to capture the diffraction patterns and the distributions of light intensity were quantitatively analyzed using Matlab®. The rotating magnetic field was generated by a designed system of four electromagnets (Figure 3.5 (a)).

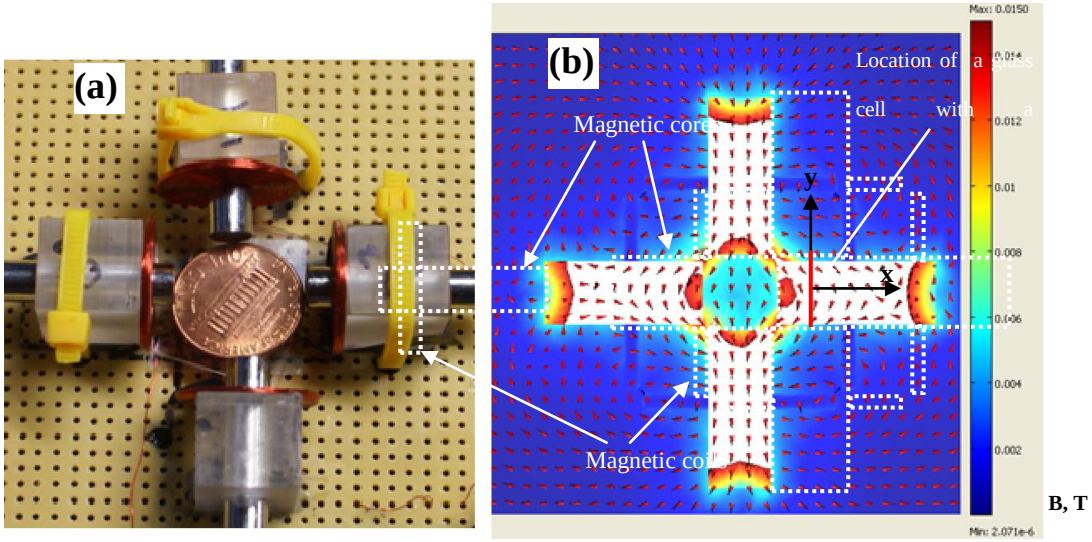

Figure 3.5 (a) system of 4 electromagnets for producing a rotating magnetic field, (b) numerical simulation of the magnetic field produced by this system in Comsol

Design of the system is described in details in Section 2.4. Each electromagnet included 6 mm diameter magnetic core and solenoid with 300 turns of copper wire. The magnitude and frequency of the magnetic field were controlled by the LabVIEW® program. To observe rotation of the nanorods, the system of electromagnets (Figure 3.5 (a)) with a microfluidic chip or a capillary containing the nanorod dispersion was placed under a microscope (Olympus MVX10). High speed digital camera (Motion Pro X3) was used to capture images of rotating magnetic

nanorods. In order to obtain the magnetic field distribution in the nanorod suspension within the cell, FEM solver COMSOL® was used to simulate the magnetic field (Figure 3.5 (b)). The validity of these calculations was confirmed by measuring the magnetic field at the center of the optical cell using the digital teslameter (133-DG GMW Inc.). The deviations between the numerical data and the measured value were not greater than 10%.

3.4.3 Results and discussion

The diffraction pattern and the distributions of light intensity along the diffraction wings obtained using the setup shown in Figure 3.4 (a) are shown in Figure 3.6. We observed that in the range of nanorod concentrations varied between 0.0015 wt. % to 0.034 wt. %, both the illumination intensity and illuminated area have increased monotonously with the nanorod concentration. This effect is explained by the multiple diffraction of light on the layers of nanorods aligned in the applied magnetic field; as the nanorod concentration increases, the light beam finds more obstacles thus enlarging the cone over which the light spreads.

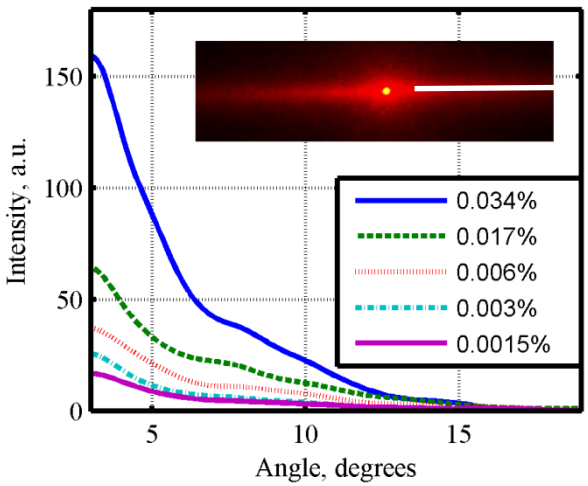

Figure 3.6. The distribution of light along the right diffraction wing (along the white line in the insert) for different mass concentrations of nanorods.

We observed this effect earlier for the chains of spherical magnetite nanospheres [14]. As proposed in Ref.[14],(Figure 3.7), one can take advantage of this reconfigurable diffraction pattern and make an optofluidic illuminator by filling a hollow fiber with a suspension of magnetic nanoparticles.

Figure 3.7 Optical fiber with a capillary tip filled with suspension of spherical nanoparticles (a) light pattern on a screen before (b) and after (c) the magnetic field was switched on. Central spot corresponds to direct laser beam (zero-order diffraction); diffracted line is slightly bended due to the imperfections in optical alignment.

The light beam from a laser can be coupled to the optical fiber with a glass tip filled with a magnetic fluid (Figure 3.7 (a)). Without magnetic field, the light goes through the tip forming a round spot on the screen (Figure 3.7 (b)).When the field is applied perpendicularly to the fiber, it deforms the spot thus illuminating a larger area (Figure 3.7 (c)).When the direction of beam propagation is perpendicular to the magnetic field, the nanoparticles form chains and diffract the light transforming a circular beam into a ribbon and yielding a larger visible area. In order to produce larger spot size, it would be advantageous to rotate this diffraction pattern by spinning the external magnetic field. In contrast with the chains of the magnetite nanospheres, the nanorods

are stable in a rotating magnetic field and strongly follow the field. Therefore, they are excellent candidates for this application. Another advantage is that the onset of rotation of the nickel nanorods is observed at lower magnetic fields, much lower than those required to form chains of spherical iron oxide nanoparticles [14]. It is known that the rate of 25 frames per second is close to the limit of naked eye resolution for moving objects. Hence, the diffraction pattern rotating at 25 revolutions per second will be seen as an almost frozen round spot, illuminating an area significantly larger than the original beam spot. In applications to optofluidic illuminators, it is necessary to estimate the relation between the required physical parameters of the nanorods and the frequency of rotating magnetic field.

It was shown in Section 3.2(Figure 3.2) that nanorods with aspect ratio $l/d<9$ can rotate synchronously with magnetic field at frequencies higher than 25 Hz. Nickel nanorods of 200 nm in diameter and 1.6μm in length ($l/d=8$) were synthesized by electrodeposition method and suspended in ethylene glycol. The tip of the optical fiber (Figure 3.7 (a)) was filled with the suspension of nanorods and placed inside of the magnetic microrotator (Figure 3.5 (a)). When magnetic field was rotating at frequency f=25 Hz the diffraction pattern from the suspension of nanorods (Figure 3.6) followed the field with the same frequency illuminating an area which much larger than the initial beam spot. Therefore, designed illuminator containing suspension of nanorods with low aspect ratios ($l/d<9$) can be used in medical optofluidic devices for illumination purposes.

3.5 Conclusions

We showed that using nickel nanorods in a rotating field, one can probe mechanical properties of materials that are difficult to analyze by any other available techniques. First, we used MRS method described in Section 1.2.3 to characterize magnetic properties of synthesized nickel nanorods. We then used obtained magnetic constants to measure rheological properties of liquids with known viscosities. Results of these measurements are in a good agreement with published values and values obtained by two plates rheometer.

Furthermore, we used MRS method to measure the viscosity in microdroplets of standard liquid S600 at different temperatures. The results of the viscosity measurements during the temperature rise obtained by MRS are in a very good agreement with the values provided by the vendor. Experimental and theoretical analysis confirms that the developed model provides correct viscosity data. Therefore, the designed instrument can be used to measure rheological properties of fluids at microscale level.

Finally, a suspension of nanorods, aligned in a magnetic field and illuminated by a visible laser beam, was used for the analysis of the diffraction pattern. It was found that increasing the concentration of nanorods in the suspension one can increase the area of diffraction wings. The control of this diffraction pattern is needed in the optofluidic applications where one needs to illuminate a larger area yet no direct mechanical contact with the light source is possible. We showed that the diffraction pattern can be rotated by spinning the magnetic field. The nanorods are stable in

rotating magnetic field, i.e. the rotation of the field does not break them as it would with a chain of spherical magnetic nanoparticles. The produced nickel nanorods are able to rotate at the rate as high as 25 revolutions per seconds that is beyond the limit of naked eye resolution for moving objects. This effect opens an opportunity for use of these colloidal suspensions in medical optofluidic devices producing stationary illuminating spots, for example in endoscopes.

3.6 References

1. Innoue, S., *Video Microscopy : The Fundamentals (Language of Science)*. 2 ed, 1997, New York: Springer. 770 pages

2. Kornev, K.G., et al., *Magnetostatic interactions between carbon nanotubes filled with magnetic nanoparticles.* Applied Physics Letters, 2008. **92**(23): p. Article Number: 233117

3. Prina-Mello, A., Z. Diao, and J. Coey, *Internalization of ferromagnetic nanowires by different living cells.* Journal of Nanobiotechnology, 2006. **4**(1): p. 1-11.

4. Hultgren, A., et al., *Optimization of yield in magnetic cell separations using nickel nanowires of different lengths.* Biotechnology Progress, 2005. **21**(2): p. 509-515.

5. Sheely, M.L., *Glycerol Viscosity Tables.* Industrial & Engineering Chemistry, 1932. **24**(9): p. 1060-1064.

6. Fosa, G., R. Badescu, and G.C. Calugaru, *On the time evolution of transmittivity in magnetic fluids.* Czechoslovak Journal of Physics, 2004. **54**(9): p. 989-996.

7. Mehta, R.V., et al., *Experimental evidence of zero forward scattering by magnetic spheres.* Physical Review Letters, 2006. **96**(12): p. Article Number: 127402.

8. Yerin, K. and S. Kunikin, *Change in the intensity of light scattering in a magnetite colloid under the simultaneous action of electric and magnetic fields.* Optics and Spectroscopy, 2007. **102**(5): p. 765-770.

9. Li, J., et al., *Coordinated chain motion resulting in intensity variation of light transmitted through ferrofluid film.* Physics Letters A, 2008. **372**(46): p. 6952-6955.

10. Haas, W.E.L. and J.E. Adams, *Diffraction Effects in Ferrofluids.* Applied Physics Letters, 1975. **27**(10): p. 571-572.

11. Bentley, A.K., et al., *Suspensions of nickel nanowires as magneto-optical switches.* Nanotechnology, 2005(10): p. 2193-2196.

12. Korneva, G., et al., *Carbon nanotubes loaded with magnetic particles.* Nano Letters, 2005. **5**(5): p. 879-884.

13. Klein, T., et al., *Magnetic-field-dependent optical transmission of nickel nanorod colloidal dispersions.* Journal of Applied Physics, 2009. **106**(11): p. Article Number: 114301.

14. Malynych, S.Z., et al., *Magneto-controlled illumination with opto-fluidics.* Journal of Magnetism and Magnetic Materials, 2010. **322**(14): p. 1894-1897.

15. Blums, E., A. Cebers, and M.M. Maiorov, *Magnetic fluids*, 1997, New York: Walter de Gruyter 416.

16. Thongmee, S., et al., *Fabrication and magnetic properties of metallic nanowires via AAO templates.* Journal of Magnetism and Magnetic Materials, 2009. **321**(18): p. 2712-2716.

4 MEASURING THE CHANGE IN THE VISCOSITY DURING THE PHOTOPOLYMERIZATION OF HEMA AT THE MICROSCALE

4.1 Introduction

In Section 1.3 we developed a numerical model describing the nanorod behavior in non-Newtonian fluid with exponentially increasing viscosity. We chose a photopolymerization of HEMA as an example of such liquid. We theoretically described an important parameter $N_{cr.}$- number of turns that the nanorod takes on before it sways back for the first time (Figure 1.11). When this parameter is measured experimentally one can use the developed numerical model to find the characteristic time of polymerization τ which defines the viscosity change during the photopolymerization process (Figure 1.10). In this chapter we describe an experimental protocol and present our results on the viscosity measurements during the photopolymerization.

First, we describe an experimental protocol to measure N_{cr} in five different solutions of HEMA with varied concentration of the crosslinker. We then use obtained data with a model described in Section 1.3 to calculate the viscosity change during the photopolymerization.

Moreover, we discuss the mechanism of HEMA polymerization, perform and discuss the FT-IR measurements during photopolymerization. All these experiments show the robustness of the proposed MRS method allowing us to find a relation between the phenomenological parameters η_0 and τ, concentration of the crosslinker, and the fraction of the crosslinked material at different stages of photopolymerization.

4.2 Materials and methods

HEMA monomer (Sigma-Aldrich Co. LLC) was mixed with the crosslinking agent DEGDMA (Sigma-Aldrich Co. LLC). Five solutions with different concentrations of the crosslinking agent, 1.86, 3, 4.5, 7, 9.3 wt%, were prepared for the testing. The photoinitiator 2,2-Dimethoxy-2-Phenylacetophenone (Sigma-Aldrich Co. LLC) of 1wt% relative to the monomers was added to the solutions. Nickel nanorods were synthesized inside pores of alumina membranes (Watman Ltd.) by the electrodeposition technique described in Section 2.2. HEMA solution was added to the beaker with nickel nanorods and an ultrasound agitation was used to prepare a uniform suspension of nanorods. Concentration of nanorods in the suspension was 0.05 wt %.

1.8µl droplet of the nanorod dispersion was placed between two glass slides. A 64 µm thick Kapton tape was inserted between the ends of two glass slides to keep them separated. The drop was sandwiched between glass slides and was investigated under the 50x objective of the BX-51 Olympus microscope. We applied the dark field microscopy technique to detect the 200nm diameter nanorods which are not visible in

the bright field [1]. First, the microscope was focused on the upper glass slide and then by moving the objective down, it was focused on the bottom glass slide. This way it was possible to focus the objective on magnetic nanorod which was situated in the middle of the optical cell. Each experiment was started by confirming that the tested nanorod was situated at least 20 μm away from each optical slide and the wall effects can be safely neglected. This nanorod position did not change during the HEMA photo polymerization experiment, i.e. the nanorods have never settled down. The following estimates explain these observations. Assuming that the nanorod is settling down at velocity υ and it keeps the long axis parallel to the plates, the drag force on a nanorod is written as $F = 4\pi\eta l\upsilon / \ln(l/d)$ [2]. This drag force is balanced by the buoyancy force, $F = \pi d^2 l \Delta\rho g / 4$, where $\Delta\rho$ =8000kg/m^3 is the density difference and g is acceleration due to gravity. Therefore, the settling velocity is estimated as $\upsilon = d^2 l \Delta\rho g \ln(l/d)/(16\eta l) = d^2 \Delta\rho g \ln(l/d)/(16\eta)$. Assuming l/d= 30, d = 0.2 μm, η =2 mPa·s (viscosity prior to photo polymerization), we have υ = 0.33 μm/s. If at the first moment a nanorod was positioned in the middle of the optical cell, which is 30 μm away from the bottom plate, it would take about t ≅ 30/0.33 ≅ 91 seconds to settle down. As shown in the experiments, the HEMA photopolymerization was initiated in less than 10 seconds after placing the droplet on the glass slide. And it took about 40 s to change the HEMA viscosity in hundred times. This explains why the buoyancy effect was insignificant and why we were able to follow the same nanorod during photo polymerization.

Two magnetic coils orthogonal to each other were used to produce rotating magnetic field. We used E-66-100 coils (15mm diameter and 8.5mm thick, Magnetic Sensor

Systems). The current was controlled with a Labview program. The design of the setup is described in Section 2.4. The magnetic field at the center of the optical cell was estimated to be $B=1.5\cdot10^{-3}$ T. A SPOT videocamera (SPOT Imaging Solutions, Inc.) was used for filming the rotating nanorod during HEMA polymerizaion. In order to initiate the polymerization, the B-100SP UV lamp (UVP, LLC) was placed 100 mm apart from the glass slides containing the HEMA solution. The light intensity at this distance was approximately 10 mW/cm^2. The captured videos were analyzed using VirtualDub software (http://www.virtualdub.org). Magnetic properties of nickel nanorods vary significantly depending on the parameters of electrodeposition process [3, 4]. In order to calculate the magnetic moments of the nickel nanorods we conducted the MRS experiments in ethylene glycol, a simple Newtonian fluid with η = 16 mPa·s, and used Eq. (3.2) to calculate *m*. The obtained magnetic moment appeared to be well approximated by the formula $m = VB\chi / \mu_0$ where *V* is the nanorod volume, μ_0 is the magnetic permeability of vacuum and χ is a constant, $\chi = 92$.

After calibration of our MRS system, we obtained the characteristic viscosity η_0 by rotating the nanorod in HEMA solution prior to exposing it to the UV radiation. Once the critical frequency was reached, we solved Eqs. (3.3) and (3.4) for the viscosity to obtain $\eta_0 = 2.7$ mPa·s. This characteristic viscosity did not change when we added the crosslinker.

In all MRS experiments, we were trying to measure the phase lag between the applied signal and nanorod displacement. Our system was unable to detect any phase lag until the nanorod reached N_{cr} revolutions. Therefore, within this time interval the material reacted as a purely viscous liquid, and no fingerprints of materials elasticity were observed. With this confirmation in hands, we applied our model to interpret the experimental data.

4.3 Results

With the obtained parameters, we used the following strategy to evaluate the dependence of characteristic time τ on the crosslinker concentration during UV-polymerization. For each of five solutions, corresponding to 1.86, 3, 4.5, 7, and 9.3 wt% crosslinker concentrations, we obtained the critical number of nanorod revolutions $N_{cr.exp}$. Ten different nanorods with the lengths ranging from 3.9 μm to 11.85 μm were used in these experiments for each droplet**.** Then we have run the numerical analysis of our model, Eqs (1.16), to fit the experimental data using τ as an adjustable parameter of the model. The obtained τ-values were used to plot ten exponential curves for each crosslinker concentration.

In Figure 4.1 (a), we plot relative viscosity $\eta(t)/\eta_0$ of HEMA with 1.86wt% concentration of the crosslinker measured with the MRS and compare these measurements with available data reported in Ref.[5] for the different power of the UV irradiation. It can be seen that the MRS results are well fitted by the exponential curve and the relative viscosity curve for our UV source (W= 10 mW/cm^2) is situated between those obtained in Ref.[5] at stronger UV irradiation with W=40 mW/cm^2

power and weaker UV irradiation with W = 0.25 mW/cm^2 power. Therefore, the obtained results appear reasonable and coherent with the available data.

In Figure 4.1 (b), we plot five dependencies of the relative viscosity, each being related to the given crosslinker content. Any point on these curves represents the average value taken over ten measurements for each concentration of the crosslinker. Error bars provide the standard deviation from the mean value. In the inset, we show the τ -dependence on the crosslinker concentration.

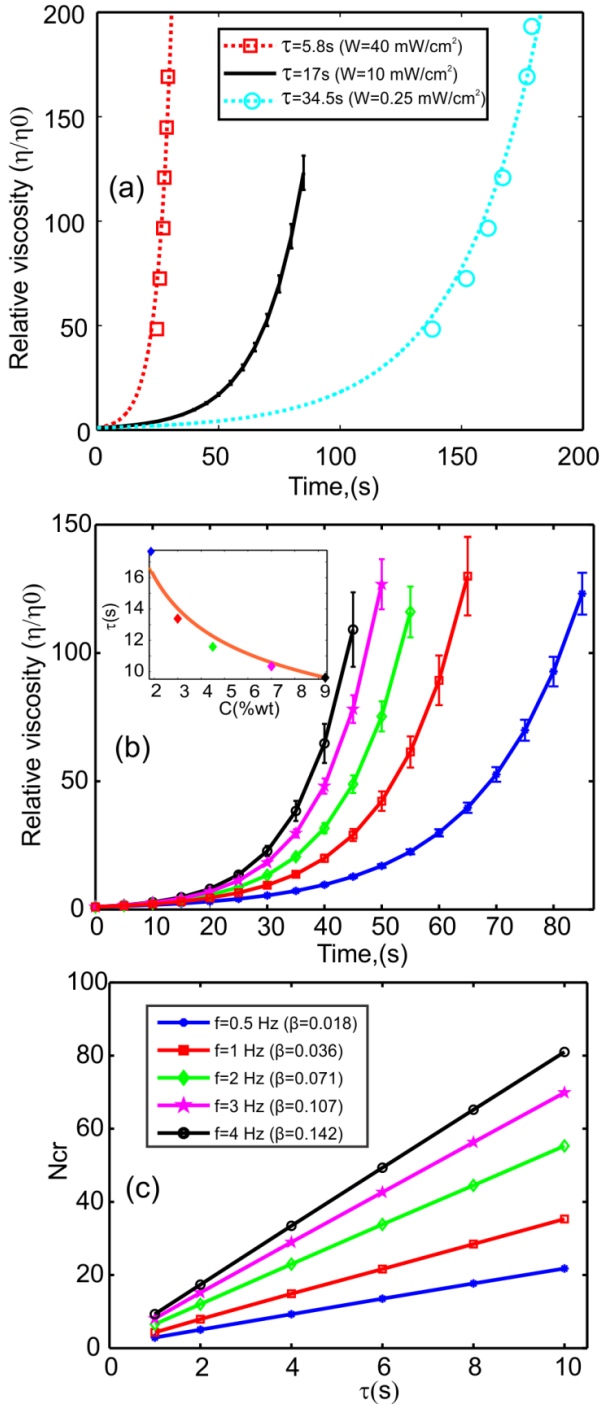

Figure 4.1 (a) The viscosity change during UV polymerization of HEMA with 1.86wt% concentration of the crosslinker measured with MRS (f=0.5Hz, $\tau = 17$ s) compared with bulk measurements of Ref.[5] corresponding to $\tau = 5.8$ s and $\tau = 34.5$ s, (b) viscosity change during UV polymerization for different concentrations of the crosslinker (from the right to the left 1.86, 3, 4.5, 7, 9.3wt%). Inset: the dependence of characteristic time τ on the weight fraction of the crosslinker, C, in the monomer-crosslinker mixture, diamonds are the experimental points; line is a cubic polynomial fit, (c) theoretical dependence of the critical number of turns N_{cr} of a nanorod as a function of characteristic time τ .

It can be seen from the graphs that the fastest change of viscosity is observed in the system with the highest concentration of the crosslinker. The dependence of the characteristic time τ on concentration of the crosslinker can be fit with a cubic polynomial $\tau = a \cdot C^{-1/3}$, where $C = m_{cr.} / m_{mix.}$ is the weight fraction of the cross-linker of weight m_{cr} in the monomer-crosslinker mixture of weight $m_{mix.}$ and a = 4.36 s is a coefficient determined from the fit. A theoretical dependence of N_{cr} on τ is shown in the Figure 4.1 (c).

This analysis demonstrates that the magnetic rotational spectroscopy allows one to measure the viscosity of polymerized solution when its viscosity drastically changes in a short time interval. However, from the MRS data, one cannot resolve whether the polymer has already undergone the transition to a gel form or it is still a liquid and not completely cross-linked yet. We therefore conducted a series of additional experiments enabling one to distinguish the conformational changes of HEMA solutions at different time moments.

4.4 Discussion

HEMA polymerizes linearly through the carbon-carbon double bond in 2-hydroxyethyl-methacrylate shown as the blue bold line in the Figure 4.2, and crosslinks through the two carbon-carbon double bonds in diethylene glycol dimethacylate shown as the red dashed lines in Figure 4.2.

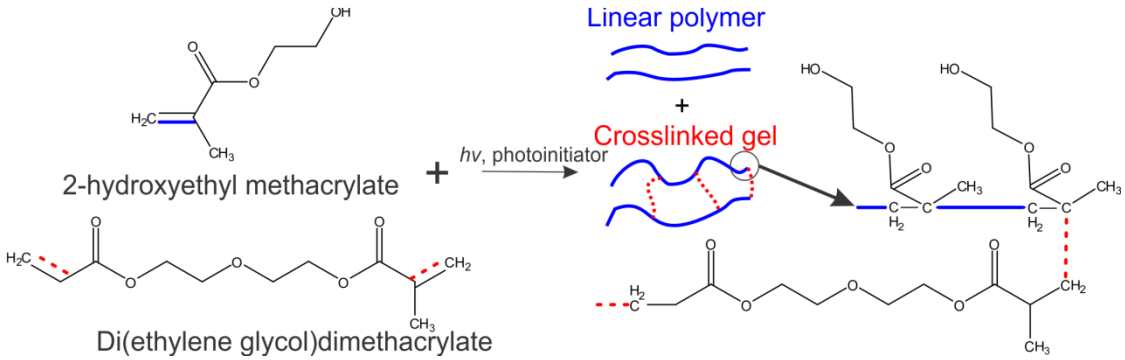

Figure 4.2 Polymerization of HEMA with DEGDMA.

Therefore, in order to evaluate the cross-linking kinetics, we used the FT-IR spectroscopy (Nicolet Magna 550). We followed the rate of decrease of carbon-carbon double bonds in the system by measuring the rate of disappearance of the 1635 cm^{-1} peak corresponding to the carbon-carbon double bonds. [6]

Figure 4.3 shows the 1638 cm^{-1} absorption peaks at time 0s (a) and after 60 second of polymerization (b) and 1720cm^{-1} peak at time 0(c) and time 60s (d):

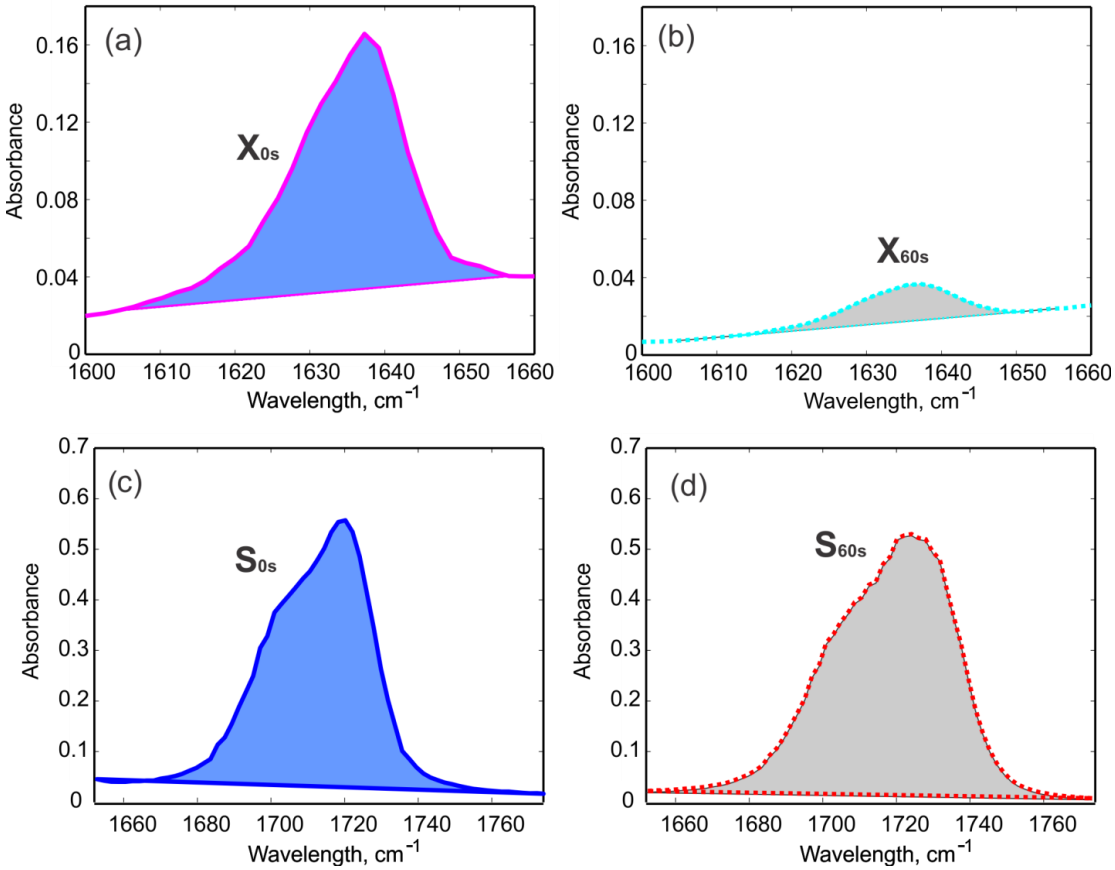

Figure 4.3 1638 cm-1 peak at time 0s (a) and after 60 second of polymerization, (b) 1720cm-1 peak at time 0(c) and time 60s(d)

In order to find the peak areas, we used the Omnic software (Nicolet Corp.). Integration intervals were set manually, then the corrected baseline was set by the Omnic software and the peak areas were calculated. The 1720 cm^{-1} peak (Figure 4.3 (c), (d)) corresponding to carbonyl group in HEMA and DEGDMA was used as a reference to calculate the conversion of carbon-carbon bonds in the system, because it does not change during the photopolymerization. We followed the double bond conversion, ϕ, corresponding to the ratio of the reacted double bonds to the total number of double bonds in the system. The conversion was found from the following equation $\phi = 100 \times (1 - X_t S_0 / X_0 S_t)$ [6] where X_0 and X_t are the areas under the 1638

cm^{-1} peak at time 0 (Figure 4.3 (a)) and time t (Figure 4.3 (b)) respectively(integration interval is 1604 - 1656 cm^{-1}), S_0 and S_t are the areas under the reference 1720cm^{-1} peak at time 0 (Figure 4.3 (c)) and time t (Figure 4.3 (d)) respectively (integration interval is 1652 - 1774 cm^{-1}).

The conversion of the double bonds ϕ with time is plotted in Figure 4.4 as the dashed line. The intensities of the absorbance peaks were measured before polymerization (solid line in the inset of Figure 4.4) and after 30, 50 and 60 seconds of the UV exposure. The dashed line in the inset of Figure 4.4 shows the intensity of the 1635 cm^{-1} peak after 60 seconds of photopolymerization.

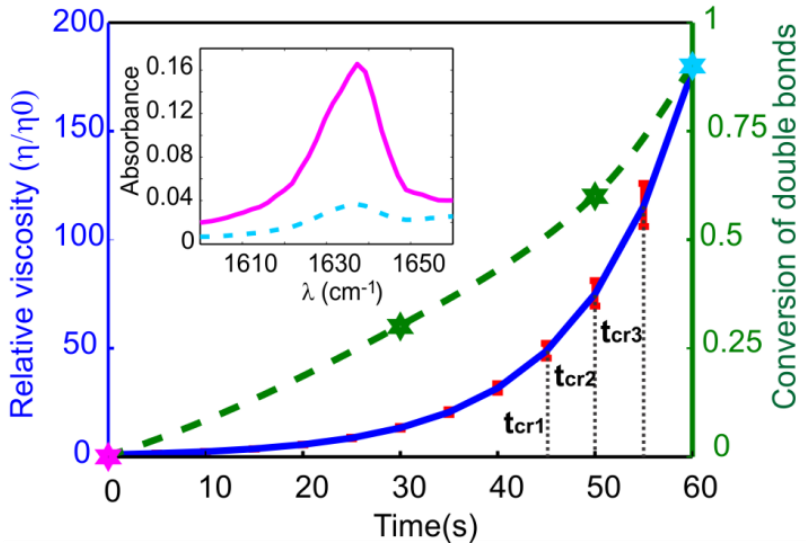

Figure 4.4 The solid line illustrates the change of relative viscosity with time of photopolymerization of the 4.5 wt% crosslinker solution (left y-axis) and the stars show the conversion of double bonds during the photopolymerization (right y-axis) and the dashed line is a trend-line. The inset shows a FTIR spectrum of the solution near 1635 cm^{-1} before (solid line) and after 60 seconds of polymerization (dashed line)

We found that the number of the double bonds in the solution has decreased by 91.4% after 60 seconds of the photopolymerization. This reduction of total number of the

double bonds in the system is caused by both the linear polymerization of HEMA and crosslinking of HEMA through the double bonds of DEGDMA. However, the FTIR analysis (showing only the total extent of the polymerization) does not provide information on the amount of the polymeric material involved in the crosslinked gel. Therefore, we determined the amount of gel fraction in the polymerizing system as a function of time (Table 4.1). This fractionation was achieved by washing out the cross-linker, photoinitiator, and a linear polymer from the sample immediately after the photopolymerization. We followed the same polymerization as described above. After 45, 50 and 55 seconds of the UV-exposure of the 4.5wt% solution, the resulted gel was collected with a blade from the glass slide. The sample was cured for time t as specified in Table 4.1, weighted and washed in water to remove unreacted water soluble monomer (HEMA) then centrifuged and washed again with a hexane (VWR International, LLC) to remove hexane soluble unreacted cross-linker (DEGDMA) and photoinitiator. Then the sample was dried in the oven under the vacuum at 75^0C for 2 hours. The sample was weighted again and the gel fraction was calculated by dividing the weight of the washed and dried sample by the weight of the initial sample. Experiment was repeated 3 times for each stage of polymerization.

Table 4.1 The amount of gel fraction at different stages of the photopolymerization.

Time of the UV-exposure, s	Fraction of crosslinked polymer at time t, wt %
45 (t_{cr1} in Figure 4.4)	23.1±2.11
50(t_{cr2} in Figure 4.4)	30.9±2.8
55(t_{cr3} in Figure 4.4)	35.7±1.4

Three points in Figure 4.4, taken at t_{cr1}, t_{cr2} and t_{cr3} correspond to the time moments when nanorods of different lengths sway back for the first time. As follows from the analysis of Figure 4.1 (c), the longer nanorods having greater parameter β stop rotating earlier than the shorter ones. Accordingly, the 6.5 μm long nanorods stopped at time t_{cr1}, the 5.8 μm long nanorods stopped at time t_{cr2}, and then the 3.9 μm long nanorods stopped at time t_{cr3}. The data presented in Table 1.1 suggests that the longer nanorods most likely probe HEMA having weakly crosslinked gel nuclei, while the shorter nanorods are able to probe HEMA having stronger crosslinked gel domains with the total amount of gel in the suspension reaching ~ 36wt%. Thus, the MRS provides instructive information about the viscosity of polymers undergoing gel formation.

4.5 Conclusions

We theoretically developed and implemented new MRS method which can be used for the *in-situ* (or *in-vivo*) rheological measurements of fluids and polymer systems when the fluid viscosity increases with time exponentially fast. Only small quantity of the sample is needed: for example, taking that the rotating 5 μm long nanorod can cover the 1pL volume, one can measure the rheological property of a drop of comparable size. The material rheology can be probed on micro as well as on nano levels, depending on the size of the used nanorods.

In this Chapter we described an experimental protocol to measure $N_{cr.}$- number of turns that the nanorod takes on before it sways back for the first time. We then used these results with the developed numerical model to find the characteristic time τ for

solutions of HEMA with 5 different concentrations of crosslinker undergoing photopolymerization.

Remarkably, an exponential increase of viscosity can be traced beyond the point when the polymer system undergoes transition to a gel and the domains start to appear. We used FT-IR spectroscopy to show that the MRS with nanorods probes the viscosity of HEMA when the conversion of double bonds reaches ~90%. We expect that this method will open new horizons in the quantitative rheological analysis of fluids inside the living cells, microorganisms, and aerosol droplets with thickeners.

4.6 References

1. Innoue, S., *Video Microscopy : The Fundamentals (Language of Science)*. 2 ed, 1997, New York: Springer. 770 pages

2. Doi, M. and S.F. Edwards, *The theory of polymer dynamics*. International series of monographs on physics1988, Oxford: Clarendon Press. xiii, 391 p.

3. Prina-Mello, A., Z. Diao, and J. Coey, *Internalization of ferromagnetic nanowires by different living cells.* Journal of Nanobiotechnology, 2006. **4**(1): p. 1-11.

4. Hultgren, A., et al., *Optimization of yield in magnetic cell separations using nickel nanowires of different lengths.* Biotechnology Progress, 2005. **21**(2): p. 509-515.

5. Li, L. and L.J. Lee, *Photopolymerization of HEMA/DEGDMA hydrogels in solution.* Polymer, 2005. **46**(25): p. 11540-11547.

6. Ghaemy, M., M. Heidaripour, and M. Barghamadi, *Synthesis, characterization, and cure reaction of methacrylate-based multifunctional monomers for dental composites.* Journal of Applied Polymer Science, 2007. **106**(3): p. 1917-1923.

5 SELF ASSEMBLY OF MAGNETIC NANORODS FOR DROP-ON-DEMAND MAGNETIC PRINTING

5.1 Introduction

With progress in nanotechnology, the complex fluids loaded with magnetic nanoparticles find new applications in electronics, analytical chemistry, and nano and biotechnology [1-9]. Many important applications require the assembly of magnetic nanoparticles into micro and nanodroplets. For example, magnetic droplets are of practical interest for printing of magnetic nanostructures on demand [10-13], for synthesis of magnetic particles with a complex structure and functionality [14-17], for the on-chip polymerase chain reaction (PCR) analyses [18], for injection of magnetic markers into single cells and gene expression analysis [19], and for bioanalitical applications [20]. Controlled formation of magnetic droplets with a broad range of size distribution is a challenge; engineering applications typically assume printing of magnetic droplets using commercial printing devices with a certain nozzle size controlling the droplet diameter [21].

In this Chapter, we report on the development of a physical principle of self-assembly of magnetic nanorods into droplets of different sizes without using any nozzle. These droplets can be formed on demand taking advantage of the magneto-static interactions between the nanorods and the magnetic field gradient. Since the nanorod length is measured in tens of microns, only hundreds of nanorods are needed to form a chain

spanning a millimeter big drop from the bottom to the top. Even in a millitesla strong uniform field, hundreds of nanorods can be gathered together within fractions of a second and are able to form a drop-diameter-long chain, Figure 5.1 (c) [22, 23]. In a gradient field, the time of formation of a micron size magnetic cluster can be made comparable or even shorter than that of a commercial printing device. All these important features of the nanorod colloid should allow one to selectively concentrate a finite amount of magnetic nanorods at the free surface and print multiple microdroplets on demand.

5.2 Magnetic poppy heads formed by the nanorods

Schematic of the experimental setup is shown in Figure 5.1 (a). We prepared nickel nanorods as described in Section 2.2. Ethylene glycol was added to the beaker with nickel nanorods and after sonication for 30 seconds (Branson Sonifier 450), a uniform suspension of Ni nanorods was produced. This dispersion was used for drop formation. A double tape (MMM237, 3M) was attached to a glass slide to prevent the droplet spreading. A permanent cylindrical magnet (K&J Magnetics, grade ND42) with a tapered tip was attached to the XYZ linear stage (VT-21, Mikos) to allow the alternation of the field gradient by moving the stage with a 100 nm minimum step in the vertical direction. Magnetic field was calculated numerically by using the FEMM software (http://www.femm.info), Figure 5.1 (b) and then the numerical results were confirmed by the measurements of magnetic field at the central axis with a digital teslameter (133-DG GMW Inc.) positioned with the manipulator (VT-21, Mikos) at different distances l from the magnet (diamonds in Figure 5.1 (b)). For further analysis, we approximated the axial component of magnetic field by formula

B=*b*/*l*=0.735/*l* which was proved correct in the range 1.7 mm < *l* < 7.1mm (the dashed line in Figure 5.1 (b)).

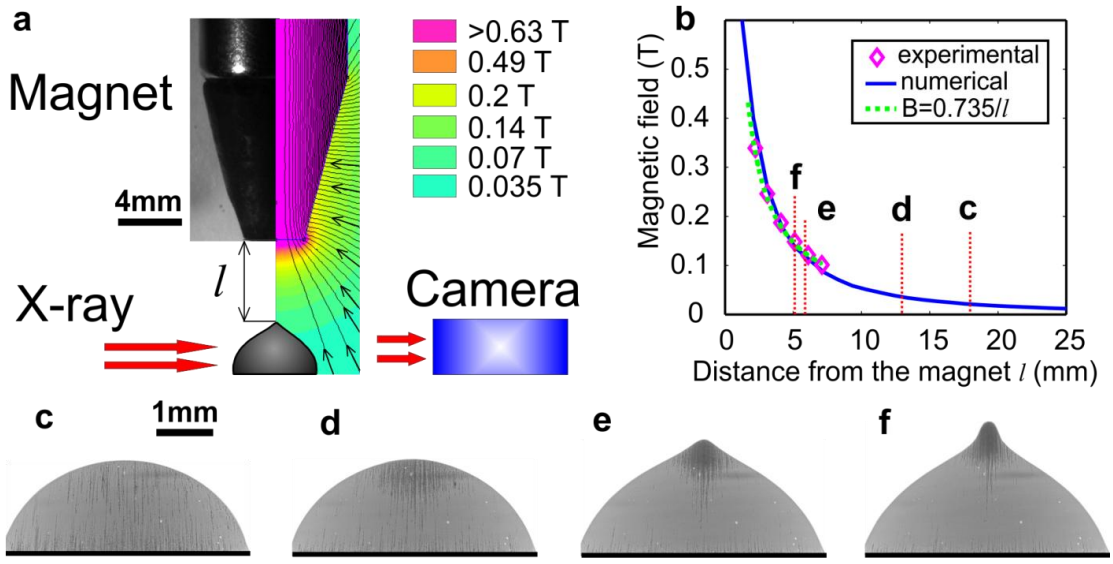

Figure 5.1 (a) A schematic of the experimental setup used in the X-Ray phase contrast imaging experiment, (b) axial magnetic field measured experimentally and calculated numerically vs. distance *l* from the magnet, where *l* = 0 corresponds to a central point at the magnet surface; (c),(d),(e),(f) : x-ray phase-contrast images of the droplet at various distances *l* from the magnet to the droplet

An analysis of the nanorod assembly was performed using the x-ray phase contrast imaging at Argonne National Laboratory. A schematic of the experimental setup is shown in Figure 5.1 (a) and a sequence of pictures illustrating the behavior of nanorods in magnetic field is presented in Figure 5.1 (c)-(f). We moved magnet toward the droplet with a constant speed (V=0.2mm/s). The Figure 5.1 (c),(d),(e) and (f) show the configurations of the droplet and the structure of nanorods chains and clusters at different distances *l* from the magnet. When the magnet is far away from the drop, the field is almost uniform and all nanorods are distributed evenly over the droplet volume. Magnetic field orients the nanorods in the vertical direction, but the

nanorods are free to move so that they form long chains from the droplet bottom to the free surface. Remarkably, the drop shape does not change during this nanorod movement. This behavior of nanorods is very unusual and cannot be reproduced with a ferrofluid, a colloid of magnetic nanobeads [24]. Ferrofluid droplet responds on the field gradient by deforming the whole fluid body, Figure 5.3 (d)-(e). Contrary to the ferrofluid, the nanorod droplet, like a poppy head of the orthodox church, forms a sharp peak at the top of the droplet.

As the magnet is moving toward the droplet, the chains start moving to the top of the droplet and cluster there (Figure 5.1 (d)). The magnetostatic energy of two magnetic dipoles oriented in the head-to-tail configuration is half of that observed in the configuration when the dipoles are placed side by side [25],[24]. Therefore, the distant nanorods have a tendency to form chains. Contrary to magnetic beads, two parallel nanorods are prone not only to the head-to-tail ordering, but they have a tendency of sidewise attraction as well [23]. In a gradient field, the magnetic force acting on a nanorod oriented along the z-axis in its negative direction is written as $\mathbf{F}_m = (\mathbf{m}\cdot\nabla)\mathbf{B} = -(m_z \partial / \partial z)\mathbf{B}$ where $m_\mathbf{z}$ is a magnetic moment of the nanorod and **B** is a magnetic field vector. Therefore, the radial component of the magnetic force causing the nanorods to cluster at or spread away from the central axis is dictated by the z - derivatives of the B_r - field component. Radial component was calculated in FEMM along the central axis of the magnet and along solid and dashed lines shown in Figure 5.2:

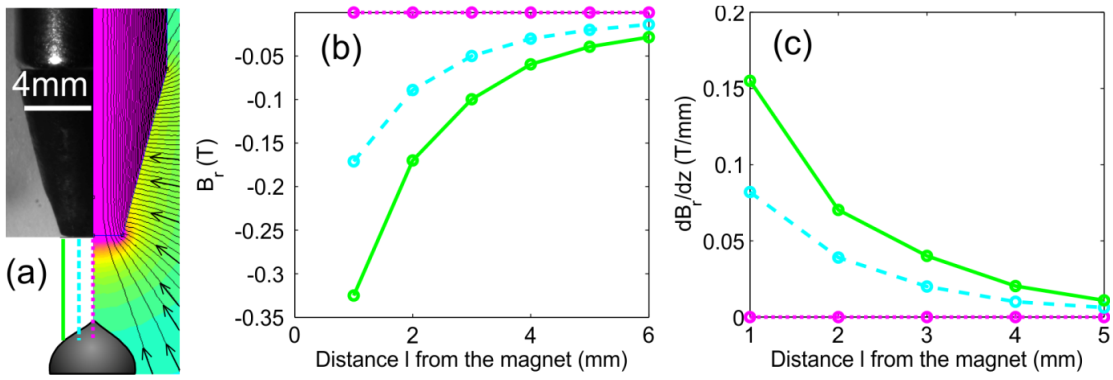

Figure 5.2 (a) A schematic of experimental setup, (b) radial component of the magnetic field B_r along the lines shown in (a), (c) z-derivative of the radial component dB_r/dz along the lines shown in (a).

The radial field component is directed toward the central axis, i.e. it is negative. This component fades away as the z-coordinate increases, Figure 5.2 (b). Therefore, the radial component of magnetic force is negative, pushing the nanorods to cluster at the central axis. The graph of the z-derivative of the radial field component is shown in Figure 5.2 (c) As follows from the figure, the z-derivative of the vertical component of magnetic field is negative. So is the z-component of magnetic force (Figure 5.1 (b)): it tends to bring all nanorods to the top.

As the cluster size increases, it deforms the droplet by creating a sharp peak at the top (Figure 5.1 (e)). The rest of the droplet profile remains non-perturbed. Until moment (e) in Figure 5.1, the process of the droplet deformation is reversible: the droplet takes on the original shape when the magnet is shifted back to its initial position. Figure 5.1 (f) shows the first irreversible shape of the droplet at critical distance l_{cr} . At this moment, the whole cluster filled with magnetic nanorods detaches from the mother droplet and jumps toward the magnet. This is a manifestation of an interfacial instability when the surface tension is unable to support the surface deformations and

any infinitesimal perturbation of the surface results in an eruption of the droplet interior [26].

Since the Bond number is less than one, Bo = $\sigma/\rho g R^2$ <<1, gravity is insignificant in these experiments. Therefore, the drop shape is controlled mostly by the capillary force. Only magnetic cluster having a tendency to jump to the magnet perturbs the droplet shape by pulling the droplet surface toward the magnet. Thus, the droplet profile is expected to be similar to an equilibrium unduloid describing the shape of a droplet sitting on a wire, Figure 5.3 (f) [27]. In the drop-on-a-wire model, the unduloid is pulled in the opposite directions by the interfacial tension of the dry wire surface acting at the contact lines.

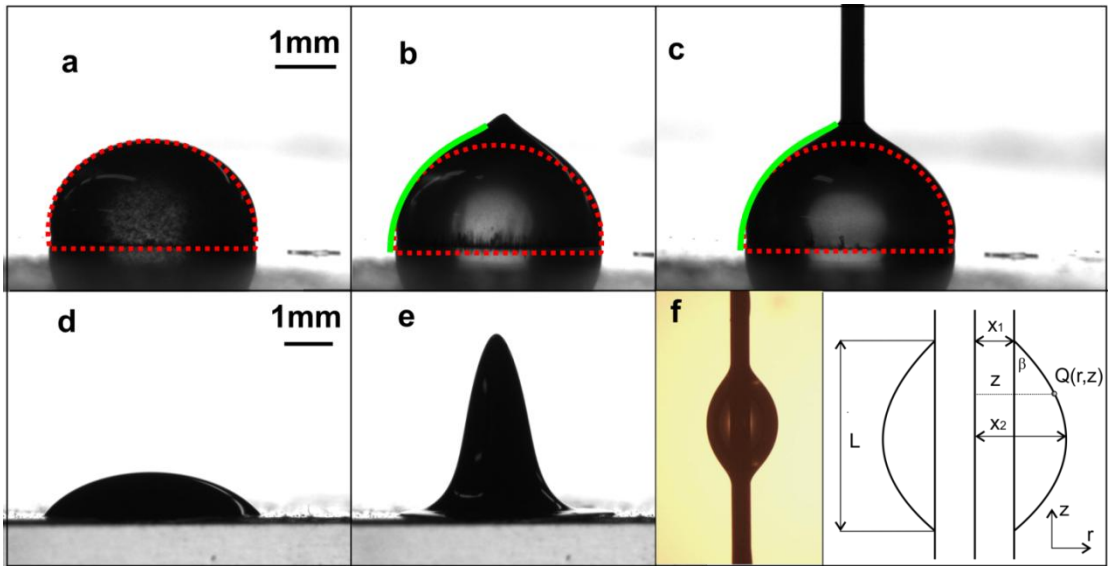

Figure 5.3 (a) The droplet with nanorods dispersion sitting on a glass slide, (b) shape of the nanorod droplet at the critical distance *l*cr from the magnet, (c) stainless steel wire with diameter d=0.46mm is inserted in the same droplet, (d) ferrodluid droplet sitting on a glass slide, (e) shape of the ferrofluid droplet at the distance *l*cr from the magnet, (f) configuration of ethylene glycol droplet sitting on stainless steel wire (wire was treated with plasma to make surface hydrophilic).

In order to confirm this analogy, the magnet was brought towards the droplet until the distance between them reached *l*cr (Figure 5.3 (b). Then the magnet was removed and different wires with diameters in the range of 0.07<d<1.5 mm were brought in contact with the droplet (copper wires with diameters d=0.4, 0.8, 0,85, 1 and 1,5 mm; tungsten wires with d=0.127 and 0.07 mm, stainless steel wires with d=1, 0.8 and 0,46 mm). The image analysis was conducted using MatLab. The unduloid corresponding to the given droplet is a solution of the Laplace equation of capillarity [27]:

$$-\frac{dz}{dr}=\frac{r^2(x_2-x_1\cos\beta)+x_1x_2(x_2\cos\beta-x_1)}{\left[r^2(x_2-x_1\cos\beta)^2(x_2{}^2-r^2)-x_1{}^2(x_2\cos\beta-x_1)^2(x_2{}^2-r^2)\right]^{\frac{1}{2}}} \qquad (5.1)$$

The shape of the droplet is defined by function $r = f$ (z, *x1/L,x2/L,* β), where *x1* is the wire radius, *x2* is the droplet radius, *L* is the droplet length, and β is the contact angle (Figure 5.3 (f)). Adjusting the contact angle β and the droplet height *L* one can fit the droplet shape. The droplet radius, x2 was taken from the images and the wire radius x1 was considered equal to the wire radius in our experiment, x1. Two other parameters, L, and β were adjusted to fit the image with function z(r), a solution of Eq. (5.1).

Upon immersion of a stainless steel wire with x1 = 0.23 mm (d=0.46 mm), we observed an unduloid, the solid line in Figure 5.3 (c), which was identical to that shown in Figure 5.3 (b) and corresponding to the onset of instability. An apparent contact angle was obtained as β =49±0.7° (an averaging is based on n = 7 droplets).

Using the droplet-on-a-wire analogy, one can introduce a radius of equivalent wire, x1. The ratio r1/x1 was found to be 2.7 for the droplet in Figure 5.3 (b) and (c). In order to check if the ratio r1/x1 is universal for all poppy heads, we conducted the X-ray experiments with different concentrations of nanorods in the initial droplet resulting in different radii of the magnetic cluster – r1,r2 and r3 (Figure 5.4 (a)-(c)). The cluster radius r was taken from the X-ray images as defined in Figure 5.4: we drew a horizontal line emanating from the outmost dark edge of the magnetic cluster. This edge is considered as the bottom boundary of the poppy head.

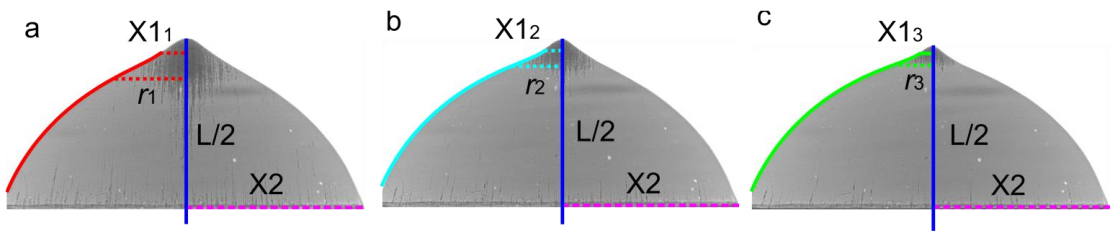

Figure 5.4 X-ray images of droplets with 3 different initial concentrations of nanorods showing the same ratio r_1/ $x1_1$= r_2/ $x1_2$= r_3/ $x1_3$=2.7

Taking advantage of this universal ratio, we first measured radius r_1 from Figure 5.4 (a). Then we calculated the radius of the equivalent fiber for the first droplet, $x1_1 = r_1/2.7$. Then we adjusted two other parameters, L, and β to fit the image with function z(r), a solution to Eq. (5.1). In two other droplets with the smaller nanorod concentrations, we kept the L-parameter same as that obtained for the first droplet. Then we measured two other radii r_2 and r_3 and obtained the radii of equivalent fibers as $x1_2 = r_2/2.7$ and $x1_3 = r_3/2.7$. The β - parameter was adjusted to fit the images with functions z(r). The corresponding contact angles were found to be almost the same, β_1 =49.4°, β_2 =49.1°, β_3 =49.3°. It can be seen from Figure 5.4 that the numerical

solutions of Eq. (5.1) overlap with the experimental droplet profiles. Therefore, we can conclude that the droplets with the same radius (X2) and different radii of the magnetic clusters can be described by function z(r), a solution to Eq. (5.1) by using the same L - parameter for all droplets, and adjusting parameter β. An effective wire radius is defined X1= r/2.7.

This analysis reveals an interesting universality of the poppy heads. It appears that the poppy heads can be considered as "frozen magnetic clusters" acting on the drop as solid objects. One can introduce an effective contact angle modeling the poppy head as a cone. The unduloid solution serves as an asymptotic solution of the Laplace equation of capillarity for a mother droplet. The contact angle where the unduloid meets the magnetic cluster is well defined and it is universal for all droplets of different generations. It is equal to $\beta = 49^0$. Using the discovered universality of the magnetic clusters, we can analyze the forces acting on them and explain the instability of poppy heads.

5.3 Stability of magnetic poppy heads. Analysis of forces

Figure 5.5 (a) shows the forces acting on the cluster of magnetic nanorods at critical distance l_{cr}:

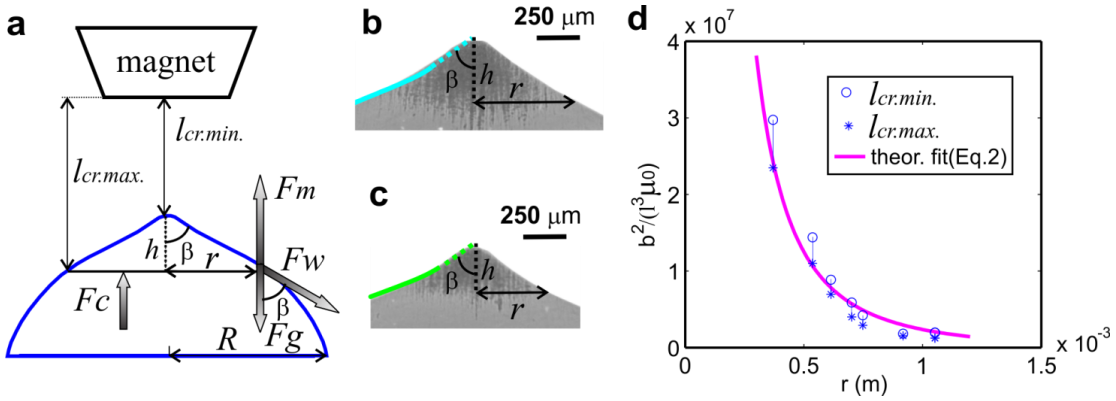

Figure 5.5 (a) Forces acting on the cluster of magnetic nanorods at critical distance lcr, (b), (c) the cluster formed by magnetic nanorods at the top of the droplet for 2 different concentrations of nanorods in the initial droplet c%wt(b)>c%wt(c), resulting in different cluster radii, r. The solid line shows an unduloid with angle $\beta = 49^0$, (e) for the given cluster radius r, the circles correspond to the left hand side of Eq. (5.3) taken at lcr.min. The stars correspond to the left hand side of Eq. (5.3) taken at lcr.max. The solid line is a theoretical fit with the right hand side of Eq. (5.3) where α was used as an adjustable parameter.

The first force is a magnetic force, $F_m = (\mathbf{m}\cdot\nabla)\mathbf{B}$, that the magnet acts on the magnetic cluster. In this equation, **m** is a magnetic moment of the cluster and **B** is a magnetic field vector. If we consider the magnetic force acting in the vertical direction, we can write $F_m = mB/l^2$. As was shown previously, the magnetic field can be approximated as B=*b*/*l*=0.735/*l* (the dashed line in Figure 1 (b)). Therefore, the magnetic force acting on the top part of the droplet can be written as $F_m = \alpha b^2 V / l^3 \mu_0$ where μ_0 is the magnetic permeability of vacuum, *V* is a volume of magnetic cluster, and α is a coefficient characterizing the cluster magnetic properties.

The second force acting on the magnetic cluster is a wetting force, $F_w = 2\pi r\sigma\cos(\beta)$, which is proportional to the radius of the magnetic cluster, *r*, to the surface tension of the liquid σ and to the contact angle β.

The third force is produced by the capillary pressure in the droplet $F_c = 2\sigma\pi r^2 / R$ where *R* is a radius of the mother droplet. The wetting force is in the order of magnitude greater than the gravitational force, $F_g / F_w \cos(\theta) \to 0$. Therefore, the gravitational force can be neglected in the balance of forces acting on the magnetic cluster. When the gravitational force is neglected we can write down the following force balance at the distance l_{cr}:

$$\frac{\alpha b^2 V}{l^3 \mu_0} + \frac{2\sigma\pi r^2}{R} = 2\pi r\sigma\cos(\theta) \qquad (5.2)$$

The volume of the magnetic cluster can be found as a volume of a cone with radius *r* and height $h = r\tan\beta : V = \pi r^3 \tan\beta / 3$. Therefore, Eq. (5.2) can be re-written as:

$$\frac{b^2}{l^3 \mu_0} = \frac{6\sigma}{\alpha \tan\beta}\left(\frac{\cos\beta}{r^2} - \frac{1}{rR}\right) \qquad (5.3)$$

In order to find constant α and check the theoretical model, we conducted experiments with 7 droplets of the same size (R=4.46±0.2mm) and with different initial concentrations of nanorods in the droplet in the range from 0.043%wt to

0.4%wt. The critical angle β was measured for all 7 droplets at distance *lcr.* and mean value from 7 measurements is β=49°.

In our experiments, all instabilities were formed in the region 1.7mm<*l*<7.1mm where the magnetic field can be approximated as B=*b*/*l*=0.735/*l*. The stage was moved towards the magnet with a 100nm step to reach a critical distance for the instability formation. The process was recorded with a Photron FastCam and Dalsa cameras at 100 fps. Videos were analyzed with VirtualDub and ImageJ software.

First, we estimated the concentration of nanorods in the magnetic cluster at different initial concentrations of nanorods in the droplet. It appears that the concentration of nanorods in the cluster does not depend on the initial concentration of nanorods in the droplet. Lower concentration of nanorods in the initial droplets resulted in a smaller radius *r* of magnetic cluster and smaller distance l_{cr}. Three parameters were measured from the recorded videos at the distance *lcr.* : radius of the cluster *r*, distance from the poppy head to the magnet *lcr.min.,* and the distance from the base of the cluster to the magnet, *lmax.*. The results of these experiments are shown in Figure 5.5 (d). For each given cluster radius r, the circles correspond to the left hand side of Eq. (5.2) taken at lcr.min. The stars correspond to the left hand side of Eq. (5.2) taken at lcr.max. The solid line is a theoretical fit with function $f(r)=\frac{6\sigma}{\alpha\tan\beta}(\frac{\cos\beta}{r^2}-\frac{1}{rR})$, where α was used as an adjustable parameter and the best fit was reached at for $\alpha=0.026$

This analysis confirms that the magnetic cluster formed from nanorods can be described as a cone-shaped solid body moving in the gradient field and deforming the top part of the drop. Extrapolating Figure 5.5 (d) to the smaller cluster radii, one expects that nanometer droplets can be formed by this method. Therefore, this principle can be used for generation of magnetic droplets on demand with desired size and volume.

5.4 Conclusions

In this Chapter we described a physical principle of self-assembly of magnetic nanorods into droplets of different sizes. These droplets can be formed on demand using magneto-static interactions between magnetic nanorods and a magnetic field gradient. We conducted experiments with different concentrations of nanorods in the initial drop and in different magnetic field gradients resulting in the different sizes of magnetic clusters. We theoretically and experimentally confirmed that the cluster of nanorods at the top of the droplet is acting as a cone-shaped solid body deforming the top part of the droplet when moving towards the magnet. By applying a higher magnetic field, one can possibly extract picoleter volumes of the liquid. All these important features of the nanorod colloid should allow one to selectively concentrate a finite amount of magnetic nanorods at the free surface and print multiple microdroplets on demand.

5.5 References

1. Erb, R.M., et al., Magnetic assembly of colloidal superstructures with multipole symmetry. Nature, 2009. 457(7232): p. 999-1002.

2. Li, F., D.P. Josephson, and A. Stein, Colloidal Assembly: The Road from Particles to Colloidal Molecules and Crystals. Angewandte Chemie-International Edition, 2011. 50(2): p. 360-388.

3. Whitesides, G.M. and B. Grzybowski, Self-assembly at all scales. Science, 2002. 295(5564): p. 2418-2421.

4. Graham, D.L., H.A. Ferreira, and P.P. Freitas, Magnetoresistive-based biosensors and biochips. Trends in Biotechnology, 2004. 22(9): p. 455-462.

5. Namiki, Y., et al., A novel magnetic crystal-lipid nanostructure for magnetically guided in vivo gene delivery. Nature Nanotechnology, 2009. 4(9): p. 598-606.

6. Wu, A.G., P. Ou, and L.Y. Zeng, Biomedical applications of magnetic nanoparticles. Nano, 2010. 5(5): p. 245-270.

7. Lalatonne, Y., J. Richardi, and M.P. Pileni, Van der Waals versus dipolar forces controlling mesoscopic organizations of magnetic nanocrystals. Nature Materials, 2004. 3(2): p. 121-125.

8. Carlson, J.D. and M.R. Jolly, MR fluid, foam and elastomer devices. Mechatronics, 2000. 10(4-5): p. 555-569.

9. Dames, P., et al., Targeted delivery of magnetic aerosol droplets to the lung. Nat Nano, 2007. 2(8): p. 495-499.

10. Ganguly, R. and I.K. Puri, Microfluidic transport in magnetic MEMS and bioMEMS. Wiley Interdisciplinary Reviews: Nanomedicine and Nanobiotechnology, 2010. 2(4): p. 382-399.

11. Zhang, K., et al., On-chip manipulation of continuous picoliter-volume superparamagnetic droplets using a magnetic force. Lab on a Chip, 2009. 9(20).

12. Wang, M.C.P. and B.D. Gates, Directed assembly of nanowires. Materials Today, 2009. 12(5): p. 34-43.

13. Wright, A.C. and M. Faulkner, Magnetophoretic assembly and printing of nanowires. Journal of Vacuum Science & Technology B: Microelectronics and Nanometer Structures, 2012. 30(2): p. 021603.

14. Tan, S.H., et al., Formation and manipulation of ferrofluid droplets at a microfluidic T-junction. Journal of Micromechanics and Microengineering, 2010. 20(4).

15. Koo, H.Y., et al., Emulsion-based synthesis of reversibly swellable, magnetic nanoparticle-embedded polymer microcapsules. Chemistry of Materials, 2006. 18(14): p. 3308-3313.

16. Frenz, L., et al., Droplet-based microreactors for the synthesis of magnetic iron oxide nanoparticles. Angewandte Chemie-International Edition, 2008. 47(36): p. 6817-6820.

17. Oh, J.K. and J.M. Park, Iron oxide-based superparamagnetic polymeric nanomaterials: Design, preparation, and biomedical application. Progress in Polymer Science, 2011. 36(1): p. 168-189.

18. Tsuchiya, H., et al., On-chip polymerase chain reaction microdevice employing a magnetic droplet-manipulation system. Sensors and Actuators B: Chemical, 2008. 130(2): p. 583-588.

19. Okochi, M., et al., Magnetic Force-based Lab-on-a-chip for Single Cell Analysis in a Droplet. ECS Transactions, 2009. 16(17): p. 15-20.

20. Lehmann, U., et al., Two-dimensional magnetic manipulation of microdroplets on a chip as a platform for bioanalytical applications. Sensors and Actuators B-Chemical, 2006. 117(2): p. 457-463.

21. Aggarwal, R., et al., Fabrication of Ag-tetracyanoquinodimethane nanostructures using ink-jet printing/vapor-solid chemical reaction process. Journal of Vacuum Science & Technology B, 2008. 26(6): p. L48-L52.

22. Tokarev, A., et al., Magnetic Nanorods for Optofluidic Applications. AIP Conference Proceedings, 2010. 1311: p. 204-209.

23. Kornev, K.G., et al., Magnetostatic interactions between carbon nanotubes filled with magnetic nanoparticles. Applied Physics Letters, 2008. 92(23): p. Article Number: 233117

24. Rosensweig, R.E., Ferrohydrodynamics1985, Cambrige: Cambrige University Press.

25. Halsey, T.C., Elecrorheological fluids. Science, 1992. 258(5083): p. 761-766.

26. Drazin, P.G. and W.H. Reid, Hydrodynamic stability. 2nd ed. Cambridge monographs on mechanics and applied mathematics2004, Cambridge, UK ; New York: Cambridge University Press. xx, 605 p.

27. Carroll, B.J., The accurate measurement of contact angle, phase contact areas, drop volume, and Laplace excess pressure in drop-on-fiber systems. Journal of Colloid and Interface Science, 1976. 57(3): p. 488-495.

6 CONCLUSIONS

In the first Chapter of this Dissertation we reviewed current microrheological methods and developed a Magnetic Rotational Spectroscopy (MRS) method describing nanorod response to a rotating magnetic field. First, we developed analytical and numerical models to study Newtonian liquids of different viscosities at the microscale. The model is designed for a specific experimental protocol. We introduced and examined physical parameters which can be measured experimentally. The same method can be used to estimate magnetization of nanorods provided that viscosity of surrounding liquid is known. We then modified the model to include non-Newtonian liquids with exponentially increasing viscosity. We conducted full numerical analysis and summarized the results in a form of a phase diagram which can be used to study the system behavior at different initial conditions. Using the numerical analysis, we developed an experimental protocol enabling extraction of the physical parameters of the model.

In the second chapter, we reviewed the techniques for magnetic nanorods synthesis. We described a setup and experimental protocol to synthesize nickel nanorods with the desired geometrical properties. In particular, the main attention was paid to the method to control the nanorod length to diameter ratio. We developed a multifunctional magnetic rotator that allows one to generate rotating magnetic fields in a broad frequency band, from hertz to tens kilohertz. This magnetic rotator was used for the rheological studies of simple and polymeric fluids at the nano and microscale. We believe that this multifunctional magnetic system will be useful not

only for micro and nanorheological studies, but will find much broader applications requiring remotely controlled manipulation of micro and nanoobjects.

In the third chapter we employed the designed magnetic system to study a temperature-dependent viscosity of synthetic oil used as a viscosity standard. Magnetic rotational spectroscopy described in the first chapter was used for these purposes. It was shown, that the MRS-based results perfectly reproduced a temperature dependence of the oil viscosity during the heating process.

A suspension of nickel nanorods, aligned in a magnetic field and illuminated by a visible laser beam, was used for the analysis of the diffraction pattern. It was found that increasing the concentration of nanorods in the suspension one can increase the area of diffraction wings. The control of this diffraction pattern is needed in the optofluidic applications where one requires to illuminate a larger area yet no direct mechanical contact with the light source is possible. We showed that the diffraction pattern can be rotated by spinning the magnetic field. The nanorods are stable in rotating magnetic field, i.e. the rotation of the field does not break them as it would with a chain of spherical magnetic nanoparticles. The produced nickel nanorods are able to rotate at the rate as high as 25 revolutions per seconds that is beyond the limit of naked eye resolution for moving objects. This effect opens an opportunity for use of these colloidal suspensions in medical optofluidic devices producing stationary illuminating spots, for example in endoscopes.

In the fourth chapter, we studied the time-dependent rheology of microdroplets of 2-hydroxyethyl-methacrylate (HEMA)/diethylene glycol dimethacylate (DEGDMA)-based hydrogel during photopolymerization synthesis. We demonstrated that magnetic rotational spectroscopy provides rich physico-chemical information about the gelation process. The method allows one to completely specify the time-dependent viscosity by directly measuring characteristic viscosity and characteristic time. Remarkably, one can analyze not only the polymer solution, but the suspension enriched with the gel domains being formed. Since the probing nanorods are measured in nanometers, this method can be used for the in vivo mapping of the rheological properties of biofluids and polymers on a microscopic level at short time intervals when other methods fall short.

In the fifth chapter, we described a physical principle of self-assembly of magnetic nanorods into droplets of different sizes. These droplets can be formed on demand using magneto-static interactions between magnetic nanorods and a magnetic field gradient. We theoretically and experimentally confirmed that the cluster of nanorods at the top of the droplet is acting as a cone-shaped solid body deforming the top part of the droplet when moving towards the magnet. The developed model allows one to selectively concentrate a finite amount of magnetic nanorods at the free surface and print multiple microdroplets on demand.